



저작자표시-비영리-변경금지 2.0 대한민국

이용자는 아래의 조건을 따르는 경우에 한하여 자유롭게

- 이 저작물을 복제, 배포, 전송, 전시, 공연 및 방송할 수 있습니다.

다음과 같은 조건을 따라야 합니다:



저작자표시. 귀하는 원저작자를 표시하여야 합니다.



비영리. 귀하는 이 저작물을 영리 목적으로 이용할 수 없습니다.



변경금지. 귀하는 이 저작물을 개작, 변형 또는 가공할 수 없습니다.

- 귀하는, 이 저작물의 재이용이나 배포의 경우, 이 저작물에 적용된 이용허락조건을 명확하게 나타내어야 합니다.
- 저작권자로부터 별도의 허가를 받으면 이러한 조건들은 적용되지 않습니다.

저작권법에 따른 이용자의 권리는 위의 내용에 의하여 영향을 받지 않습니다.

이것은 [이용허락규약\(Legal Code\)](#)을 이해하기 쉽게 요약한 것입니다.

[Disclaimer](#)

Doctoral Thesis

Capacitive Memory Effect of
Metal/Semiconductor Junction and Its
Application in Superconducting Circuit QED

Gahyun Choi

Department of Physics

Graduate School of UNIST

2019

Capacitive Memory Effect of
Metal/Semiconductor Junction and Its
Application in Superconducting Circuit QED

Gahyun Choi

Department of Physics

Graduate School of UNIST

Capacitive Memory Effect of Metal/Semiconductor Junction and Its Application in Superconducting Circuit QED

A thesis/dissertation
submitted to the Graduate School of UNIST
in partial fulfillment of the
requirements for the degree of
Doctor of Philosophy

Gahyun Choi

06. 11. 2019

Approved by

Advisor

Kibog Park

Capacitive Memory Effect of Metal/Semiconductor Junction and Its Application in Superconducting Circuit QED

Gahyun Choi

This certifies that the thesis/dissertation of Gahyun Choi is approved.

06. 11. 2019

signature

Advisor: Kibog Park

signature

Yonuk Chong: Thesis Committee Member #1

signature

Jingook Kim: Thesis Committee Member #2

signature

Min-Suk Kwon: Thesis Committee Member #3

signature

Kunook Chung: Thesis Committee Member #4;

Abstract

In the superconducting quantum circuits, a LC oscillator is a main component and Josephson junction gives nonlinearity. Tuning of resonant frequency can be achieved in general by modulating a Josephson inductance of superconducting quantum interference device (SQUID) with magnetic flux. Here, it is proposed to realize tunable capacitor by using metal/semiconductor junction, which can be applied in the superconducting circuit system.

Prior to realization of tunable capacitor, the electron transport at metal/semiconductor junctions is studied with two different interfacial layers, Al_2O_3 and graphene. The effects of interface states on electrical properties of the junction are studied by observing the change in Schottky barrier. First, the Schottky barrier height of Au/Ni/ Al_2O_3 /4H-SiC junction increases compared to that of Au/Ni/4H-SiC junction. It is because the electrostatic potential increases due to dipole effect on spontaneous polarization of 4H-SiC as a separation between metal and semiconductor increases. On the other hand, in case of Au/Graphene/4H-SiC junction, the Schottky barrier height decreases due to the presence of graphene. When the metal and graphene are in contact, there is charge transfer through Au/Graphene interface and then the graphene becomes doped. In addition, dipole is formed at the interface between Au and graphene. As a result, the effective work function becomes reduced, so does the Schottky barrier height.

Based on the understanding of Schottky junction, tunable capacitor is realized by fabricating Au/Cr/ Al_2O_3 /Al/Si junction. With thick Al_2O_3 film, the electron transfer is blocked for the path between Cr and Al and is allowed only through the Al/Si Schottky junction. Then, the electrons can be captured in the Al floating metal. The amount of charge is dependent on the magnitude of voltage pulses and then discrete capacitance values can be defined. This capacitive memory effect of the tunable capacitor using Schottky junction is expected to be used in the superconducting quantum circuit system in respect that it can change the resonant frequency with discrete capacitance.

Among the existing superconducting quantum circuit models, superconducting qubit is the most representative example of LC oscillators. Many superconducting circuit applications have been used to operate the qubits effectively. One promising application in the superconducting circuit QED is Josephson parametric amplifier (JPA). The JPA has been attracted as a device amplifying a signal in quantum-limited regime. It is observed in this dissertation that the JPA and Josephson parametric converter (JPC) which is another kind of JPA can improve the measurement efficiency in superconducting qubit detection. Also, the squeezed state which is another property of the JPA is studied by preparing it with the JPA and amplifying the squeezed signal with the JPC. The phase-dependence of the squeezed state is measured with homodyne setup and is reconstructed visually by using Wigner function.

Finally, it is explored to reconstruct quantum state as a form of density matrix by using quantum state tomography (QST) in the superconducting multi-qubit system. It is important to extract quantum state in quantum information processing and necessary to expand the analysis on multi-qubit system. In this dissertation, the QSTs on two and three qubits are studied. A joint qubit readout method is used to measure an ensemble of the system. Also, Z-axis phase gate by using hyperbolic secant pulse is discussed in two qubit system. By using sech pulse, the phase accumulated during microwave-activated phase (MAP) gate can be controlled and eventually compensated. It is expected that the state fidelity can be improved by controlling phase on the qubit.

Contents

Abstract	i
Contents	iv
List of Figures	vii
List of Tables	x
Nomenclature	xi
Chapter 1 . Introduction	1
1.1 Overview of Thesis	2
Chapter 2 . Superconducting Quantum Circuits	4
2.1 Superconducting Circuits	4
2.1.1 LC Oscillator	4
2.1.2 Josephson Junction	5
2.1.3 SQUID	7
2.2 Superconducting Qubits	8
2.2.1 Quantum Bit	8
2.2.2 Transmon Qubit	9
2.2.3 Circuit QED	11
Chapter 3 . Metal/Semiconductor Junction	12
3.1 Energy Band Theory	12
3.2 Ideal Metal/Semiconductor Junction	13
3.3 Schottky Junction	15
3.3.1 I-V Characteristic	15
3.3.2 C-V Characteristic	16
3.3.3 IPE Characteristic	17
3.4 Silicon Carbide	19
3.4.1. Structural Properties	19
3.4.2. Electrical Properties	20
3.4.3 Spontaneous Polarization	22
Chapter 4 . Sample Fabrication	23
4.1 Fabrication of Metal/Semiconductor Junction	23
4.1.1 Ohmic Contact	23
4.1.2 Graphene Transfer	25
4.2 Setup for Experiments with Schottky Junction	26

4.3 Design and Measurement of Superconducting Circuit	27
4.3.1 CPW Structure	27
4.3.2 Interdigitated Capacitor	28
4.3.3 Superconducting Resonator Measurement	30
4.4 Setup for Experiments with Superconducting Circuit	32
4.4.1 Cryogenic Setup	32
4.4.2 Homodyne Measurement	33
Chapter 5 . Metal/Semiconductor Junction with Various Interfacial Layers and Its Application in Tunable Capacitor	34
5.1 Modulation of Metal/4H-SiC Schottky Barrier by Inserting Thin Al ₂ O ₃ Layer	34
5.1.1 Sample Fabrication.....	35
5.1.2 I-V Measurement	36
5.1.3 C-V Measurement	38
5.1.4 Finite Element Electrostatic Modeling	39
5.1.5 Conclusion	42
5.2 Effect of Electric Dipole Formed at Au/Graphene Interface on Au/Graphene/4H-SiC Junction.....	42
5.2.1 Graphene	43
5.2.2 Sample Fabrication.....	44
5.2.3 I-V Measurement	44
5.2.4 C-V Measurement	45
5.2.5 IPE Measurement.....	46
5.2.6 Finite Element Electrostatic Modeling	47
5.2.7 Conclusion	49
5.3 Capacitive Memory Effect of Au/Cr/Al ₂ O ₃ /Al/Si Junction.....	51
5.3.1 Memcapacitor	51
5.3.2 Sample Fabrication.....	51
5.3.3 Working Mechanism.....	52
5.3.4 Experimental Results	54
5.3.5 Conclusion	56
Chapter 6 . Squeezed State Generated by Josephson Parametric Amplifier.....	58
6.1 Parametric Amplifier	58
6.1.1 Working Principle	58
6.1.2 Phase Preserving Amplification	60
6.1.3 Phase Sensitive Amplification	61
6.1.4 Gain Performance	62

6.2 Parametric Amplifier Measurements	63
6.2.1 Josephson Parametric Amplifier	63
6.2.2 Josephson Parametric Converter	65
6.3 Generation of Squeezed State	68
6.3.1 Experimental Results	68
6.3.2 Wigner Tomography	73
6.3.3 Conclusion	74
Chapter 7 . Quantum State Tomography with Circuit QED	75
7.1 Multi Qubit Measurement	75
7.1.1 Quantum State Tomography	75
7.1.2 Joint Readout	77
7.1.3 Experimental Realization with Three Qubits	77
7.1.4 Conclusion	80
7.2 Phase Compensation via Z-axis Phase Gate	81
7.2.1 Microwave Activated Phase Gate	81
7.2.2 Hyperbolic Secant Pulse for Z-axis Phase Gate	83
7.2.3 Experimental Result in Two Qubit System	85
7.2.4 Conclusion	87
Chapter 8 . Conclusion and Outlook	88
Appendix A. Recipes	90
Appendix B. JPA and JPC	93
Appendix C. Single Qubit Operation	94
References	97
Curriculum Vitae	107
Acknowledgement	111

List of Figures

Figure 2 .1 Representation of LC oscillators.	5
Figure 2 .2 Representation of Josephson junction.	6
Figure 2 .3 Schematic of SQUID.	7
Figure 2 .4 Bloch sphere representation.	9
Figure 2 .5 Representation of transmon qubit.	10
Figure 2 .6 Schematic of cavity QED.	11
Figure 3 .1 Energy band for electrons.	12
Figure 3 .2 Classification of solids.	13
Figure 3 .3 Energy band diagram of metal/semiconductor contact.	14
Figure 3 .4 I-V characteristics of Schottky junction.	15
Figure 3 .5 C-V characteristics of Schottky junction.	17
Figure 3 .6 IPE characteristics of Schottky junction.	18
Figure 3 .7 Tetrahedral structure of SiC and covalent bond between Si and C atoms	19
Figure 3 .8 Stacking sequence of SiC bilayers representing polytypes.	21
Figure 3 .9 Formation of SP due to the broken equivalence of tetrahedral bonds.	22
Figure 4 .1 I-V characteristics of Ohmic contact.	24
Figure 4 .2 Raman spectrum of graphene transferred on SiC substrate.	25
Figure 4 .3 Measurement setup for metal/semiconductor junctions.	26
Figure 4 .4 Schematic of transmission line.	28
Figure 4 .5 Design of interdigitated capacitor on COMSOL.	29
Figure 4 .6 Simulation results of interdigitated capacitor.	30
Figure 4 .7 Design of superconducting resonator.	31
Figure 4 .8 Measurement of Nb superconducting resonator.	31
Figure 4 .9 Resonant frequency tuning of the superconducting resonator.	31
Figure 4 .10 Experimental setup on mixing chamber plate for characterization of the samples.	32
Figure 5 .1 Cross-sectional HRTEM image of the Au/Ni/Al ₂ O ₃ /4H-SiC junction and the Au/Ni/4H-SiC junction.	35
Figure 5 .2 Current density as a function of forward bias for Au/Ni/4H-SiC and Au/Ni/Al ₂ O ₃ /4H-SiC junctions in semi-log scale. Also, the linear relation between ideality factor and SBH.	36
Figure 5 .3 The C-V characteristics in measured and calculated 1/C ² vs. V _R plots.	39

Figure 5.4 Device layer schematic and energy band diagram of Au/Ni/4H-SiC and Au/Ni/Al ₂ O ₃ /4H-SiC junctions.....	41
Figure 5.5 Honeycomb lattice structure and Dirac-cone energy band structure of graphene.....	43
Figure 5.6 I-V characteristics for Au/4H-SiC and Au/Gr/4H-SiC junctions in linear scale and in log-scale.....	45
Figure 5.7 C-V characteristic in measured 1/C ² vs. V _R plots for Au/4H-SiC and Au/Gr/4H-SiC junctions.....	46
Figure 5.8 IPE Characteristic for Au/4H-SiC and Au/Gr/4H-SiC junctions.....	47
Figure 5.9 Band diagrams of (a) Au/4H-SiC and (b) Au/Gr/4H-SiC junctions. The parameters used in the calculation are denoted. Graphene has Dirac-cone shaped energy band.....	50
Figure 5.10 Characteristics of memcapacitor.....	52
Figure 5.11 Energy band diagrams of the memcapacitor with a structure of metal/oxide/floating-Schottky junction.....	53
Figure 5.12 Memcapacitive characteristics of Au/Cr/Al ₂ O ₃ /Al/Si junction.....	55
Figure 5.13 The fluctuation in junction capacitance depending on the erasing voltage.....	56
Figure 5.14 Capacitance-voltage hysteretic behavior of the Au/Cr/Al ₂ O ₃ /Al/Si junction.....	57
Figure 6.1 Parametric amplification process.....	59
Figure 6.2 Type of parametric amplification in respect to the phase.....	60
Figure 6.3 Circuit schematic of the JPC.....	61
Figure 6.4 Circuit schematic of two types of JPA.....	62
Figure 6.5 Amplified signal having gain of G _{max} and bandwidth of B.....	62
Figure 6.6 Flux dependence of the resonant frequency of JPA.....	63
Figure 6.7 Amplified signal of the JPA with the maximum gain of 10.8 dB.....	64
Figure 6.8 Improvement of noisy measurement by using JPA.....	65
Figure 6.9 Flux dependence of the resonant frequency of signal and idler resonators of the JPC. ...	66
Figure 6.10 JPC gain curves for different pump power and frequency for signal resonator and idler resonator.....	67
Figure 6.11 Application to qubit measurement with JPC.....	68
Figure 6.12 Experimental setups for measuring squeezed state.....	69
Figure 6.13 Flux dependence of the parametric amplifiers.....	70
Figure 6.14 Amplification properties of the parametric amplifiers.....	70
Figure 6.15 Measurement of marginal distributions.....	71

Figure 6 .16	Experimental results of distributions at each phase.....	72
Figure 6 .17	Representation of JPA-off and JPA-on states with photon numbers and Wigner tomography.	74
Figure 7 .1	Step of quantum state tomography.	76
Figure 7 .2	Characterization of three superconducting transmon qubits in a 3D cavity.	78
Figure 7 .3	Joint readout results through simultaneous Rabi oscillations for single, two, and three qubits.....	79
Figure 7 .4	Experimental results of three-qubit QST in case of $X_{\pi/2}$ rotations for each qubit.	80
Figure 7 .5 (a)	Energy diagram of two qubit system during the MAP gate.	82
Figure 7 .6	Operation of Z-axis phase gate.....	83
Figure 7 .7	Pulse shapes for three different pulses.....	83
Figure 7 .8	Experimental and theoretical Rabi oscillation map as a function of detuning frequency of $\Delta = \omega_D - \omega_{10}$ for different pulse shapes.....	84
Figure 7 .9	Characterization of two superconducting transmon qubits in a 3D cavity.	85
Figure 7 .10	Phase estimation for z-axis phase gate by using hyperbolic secant shaped pulse.	86
Figure 7 .11	Phase compensation via Z-axis phase gate.	87
Figure A.1	Photomask design for superconducting resonator	92
Figure B.1	Photograph of JPC SN019 to test either signal or idler mode resonator.....	93
Figure B.2	Photograph of JPC mounted on the mixing chamber stage in dilution fridge.	93
Figure C.1	Experimental results of RB for the pulse length of 55 ns and 200 ns.....	94
Figure C.2	Confirmation for calibrating the offset in the pulse.....	95
Figure C.3	Single qubit QST for tracking qubit rotation in X- and Y-directions.....	95
Figure C.4	Single qubit QST depending on the different rotation axis (0, 45, 60, and 90 °).....	96
Figure C.5	Single qubit QST by varying I factor from 1 to 0 by an interval of 0.1.....	96

List of Tables

Table 5.1 Summary of electronic properties for Au/Ni/4H-SiC and Au/Ni/Al ₂ O ₃ /4H-SiC junctions.	37
Table 5.2 The material parameters used for finite element electrostatic modeling.	41
Table 5.3 Summary of data for Au/4H-SiC and Au/Gr/4H-SiC.	47
Table 5.4 The parameters used for material electrical properties in finite element method.	49
Table 6.1 Operation range for JPC with 20 dB gain.	65
Table 7.1 Qubit parameters used for three qubit state tomography.	78
Table 7.2 β parameters estimated from three tone Rabi oscillation.	79
Table 7.3 Qubit parameters used for phase compensation in two qubit system.	85

Nomenclature

AC	Alternating Current
ALD	Atomic Layer Deposition
AWG	Arbitrary Waveform Generator
BOE	Buffered Oxide Etch
C	Capacitor
CPW	Coplanar Waveguide
CVD	Chemical Vapor Deposition
C-V	Capacitance-Voltage
D	Dissipation
DC	Direct Current
DI water	Deionized water
Gr	Graphene
HF	Hydrogen Fluoride
HRTEM	High Resolution Transmission Electron Microscopy
IDC	Interdigitated Capacitor
IFL	Image Force Lowering
IPA	Isopropyl Alcohol
IPE	Internal Photoemission
I-V	Current-Voltage
JPA	Josephson Parametric Amplifier
JPC	Josephson Parametric Converter
JRM	Josephson Ring Modulator
L	Inductor
LO	Local Oscillator
MAP gate	Microwave Activated Phase gate
MLE	Maximum Likelihood Estimation

NV	Nitrogen Vacancy
PCB	Printed Circuit Board
PECVD	Plasma Enhanced Chemical Vapor Deposition
PMMA	Poly(methyl methacrylate)
QED	Quantum Electrodynamics
QST	Quantum State Tomography
RB	Randomized Benchmarking
RF	Radio Frequency
RIE	Reactive-Ion Etching
RTA	Rapid Thermal Annealing
SBH	Schottky Barrier Height
SBMOSFET	Schottky Barrier Metal Oxide Semiconductor Field Effect Transistors
Sech	Hyperbolic Secant
Si	Silicon
SiC	Silicon Carbide
SNR	Signal-to-Noise Ratio
SP	Spontaneous Polarization
SQUID	Superconducting Quantum Interference Device
TMA	Trimethylaluminum
VNA	Vector Network Analyzer

Chapter 1 . Introduction

Quantum computing has fascinated as the amount of information to be stored and manipulated has increased [1], [2]. While classical computer uses bit, either 0 or 1, to store the information, the quantum computer operates based on ‘qubit’. The qubit is a quantum bit consisting of two levels, labeled as $|0\rangle$ and $|1\rangle$. The information can be stored in each level or a superposition of both levels. Furthermore, quantum entanglement of qubits is another important feature in the quantum computer in that it allows the correlation between qubits even separated by a distance. Based on these quantum phenomena, the quantum computer can overcome the limitation of the classical computer such as complicated and time-consuming problems.

Superconducting circuit is one of promising candidates to realize the quantum computing [3]–[5]. The superconducting circuit system has an advantage of energy efficiency due to zero resistance under transition temperature. Also, the circuit system can be structured as designed, so it is useful to develop a quantum processor. The superconducting circuit consists of capacitor, inductor and Josephson junction. The Josephson junction consists of two superconductors separated by a thin insulator, and its inductance gives nonlinearity [6], [7]. The basic combination of the circuit elements is a LC oscillator which is a harmonic oscillator having an equal energy spacing. In the superconducting circuit, the energy level can become anharmonic with the nonlinear Josephson inductance.

Since the first quantum phenomenon was observed experimentally on the superconducting circuit in 1987 [8], the research on the superconducting circuit has expanded to an artificial atom, called as a qubit [9]. After the first observation of the superconducting charge qubit [10], several different types of qubit such as phase [11], flux [12], [13], or transmon [14], [15] qubits have been realized. The behaviors of superconducting qubit have been studied based on circuit quantum electrodynamic (QED). The circuit QED can be understood by replacing components in cavity QED where the interaction of original light and matter is explored [16]. A reflective cavity is substituted by coplanar waveguide (CPW) resonator, natural atom by artificial atom, and optical photon by microwave photon, respectively.

The superconducting resonator has a specific resonant frequency which is determined by the LC circuit parameters. On the other hand, when superconducting quantum interference device (SQUID) is used instead of the Josephson junction, the resonant frequency can be tuned because Josephson inductance of the device is dependent on magnetic flux. In operation of the superconducting qubit, the magnetic flux noise is a source of decoherence or dephasing [17]. This noise is usually originated from surrounding magnetic components, such as coils, screws, cryogenic components, and even adsorbed O_2 molecular [18]. However, many unknown noise sources have still remained [19]. Therefore, a device having tunable capacitance might be useful because it is not required to use magnetic flux generated

from the current flowing through the coil to control the Josephson inductance. Still, only a few superconducting microwave resonators with tunable capacitor has been realized experimentally [20]. Meanwhile, a Si-based device operating at cryogenic temperature has been developed, including the recent research on Schottky Barrier Metal Oxide Semiconductor Field Effect Transistors (SBMOSFETs) working at 10 mK [21]. Its fabrication process is also compatible with the superconducting technology. Therefore, the semiconductor devices can be applied to the superconducting circuit system. It is expected that decoherence source is reduced by replacing the tunable inductor with tunable capacitor.

In addition to decoherence by magnetic flux, a low power probing signal has been required because the superconducting qubits are unstable and easy to be disturbed from an environment. However, the weak input signal makes it difficult to detect signal coming from the resonator due to added noise, reducing measurement efficiency. Accordingly, Josephson parametric amplifier (JPA), one of the superconducting circuit devices, has been attracted in that it amplifies the signal without additional noise [22]–[25]. The JPA consists of LC circuit terminated with the SQUID, allowing the resonant frequency tuning, and pump line. When an injected signal is reflected from the nonlinear inductors, or SQUID, located at the end of the resonator, the signal is amplified by a parametric nonlinearity and strong pump tone. Several precedent studies have shown that when the JPA is used for the experiments, signal-to-noise ratio (SNR) could be improved and the qubit measurement with high fidelity was allowed [26]–[28]. Another attracting property of the JPA is a generation of squeezed state [29]–[31] which is a quantum state having reduced fluctuation in one quadrature and enlarged fluctuation in the other quadrature. Squeezing signal allows the JPA to operate below quantum limit and observe resonance fluorescence [32]–[34].

In the quantum information processing, it is fundamental step to define the quantum states composed by superconducting qubit in circuit QED. It can be achieved by a series of measurement of quantum state tomography (QST). Then, the quantum state can be expressed with density matrix and the state fidelity. As the size of quantum system grows, it is required to perform the QST on multiple qubit states. However, because there is a challenge in increasing the number of parameters to be solved and measurements, more effective method is needed. Also, the improvement in single qubit gate fidelity is one of possible implements.

1.1 Overview of Thesis

The aim of this thesis is to suggest an application of tunable capacitive device to superconducting circuit QED and investigate its system in respect to JPA and superconducting qubit. Chapter 2 provides an overview of superconducting circuits. First, the superconducting circuit elements are introduced, including LC oscillator, Josephson junction and SQUID. The second part of the chapter covers quantum bit, transmon qubit, and circuit QED to be necessary to understand superconducting qubits. Chapter 3

introduces the basic concepts of metal/semiconductor junction and Schottky junction that are used to realize memcapacitive device. Further, methods to characterize the Schottky barrier height (SBH) are discussed, including current-voltage (I-V), capacitance voltage (C-V), and internal photoemission (IPE). Then, material and electrical properties of silicon carbide (SiC) which is used to form Schottky junction are examined. Chapter 4 presents the formation of Ohmic contact for ground electrode and graphene transfer method. The metal/semiconductor junctions are measured at room temperature and its measurement setup is followed. In later part, the design of superconducting resonator by using CPW structure and interdigitated capacitor is discussed. The measurement of superconducting resonator and its cryogenic measurement system are also described. Chapter 5 covers the electrical properties of Schottky junction with different interfacial layers. Aluminum oxide and graphene are used for the interfacial layers, and experimental results for both cases are followed. Also, the device having capacitive memory effect for the application to the superconducting circuits is discussed. Chapter 6 covers the operation of Josephson parametric amplifier (JPA) and Josephson parametric converter (JPC). In advance of generating the squeezed state, the parametric amplifiers are characterized in respect to tunability and gain. Then, the squeezed state prepared by the JPA is demonstrated by reconstructing it with the Wigner tomography. Chapter 7 discusses quantum state tomography of multi-qubit system by using joint qubit readout and maximum likelihood estimation. In the following, the phase compensation by using hyperbolic secant pulse after microwave-activated phase gate is studied. Finally, chapter 8 concludes this thesis and gives an outlook for the experiments.

Chapter 2 . Superconducting Quantum Circuits

Many candidates to form two-level system can be used as a qubit which is a basic component of quantum computer. Trapped ions, NV centers in diamond, nuclear spins, and superconducting circuits are such examples for implementing qubit. Among them, it is focused on superconducting qubits and resonators which are basically composed of LC oscillator designed on a semiconductor substrate. This chapter starts with an introduction of basic and new circuit elements such as LC circuit and Josephson junction. After a brief review of quantum bit (or qubit), transmon qubit is followed as a typical type of superconducting qubit. Also, this chapter provides a short introduction of circuit quantum electrodynamics (QED).

2.1 Superconducting Circuits

A building block for the superconducting electrical circuit is LC oscillator as a standard circuit element and Josephson junction as a new one. In general, the inductor and capacitor are used to form a linear device. On the other hand, the Josephson junction provides a nonlinearity. Superconducting quantum interference device (SQUID) where two Josephson junctions are parallel-connected gives a nonlinear inductance by an external magnetic flux unlike the conventional inductor and capacitor. These properties are used basically for all superconducting circuit system.

2.1.1 LC Oscillator

To understand application of quantum behaviors to the electrical circuits, LC oscillator is introduced first. The LC oscillator is composed of a capacitor and an inductor connected in parallel as shown in Fig. 2.1(a). Between current I and voltage V , there are relations of $I = CdV/dt$ and $V = LdI/dt$. The resonant frequency of mode is determined by the given circuit parameters $\omega_0 = 1/\sqrt{LC}$. The stored energies in an electric field of capacitor and a magnetic field of inductor are presented as $E_C = CV^2/2$ and $E_L = LI^2/2$, respectively. The energy of system oscillates periodically between two energies with the resonant frequency ω_0 and the energy level with definite photon number is described in Fig. 2.1(b). In analogy to the pendulum, the magnetic flux in the inductor can be treated as a position and the charge in the capacitor as a conjugate momentum in this harmonic oscillating system. Then, two observables, or quadratures, can be written as a function of ladder operators

$$\Phi = i\sqrt{\frac{\hbar L\omega_0}{2}}(a - a^\dagger) \quad \text{and} \quad Q = i\sqrt{\frac{\hbar C\omega_0}{2}}(a + a^\dagger) \quad (2.1)$$

where a is the annihilation operator and a^\dagger the creation operator, satisfying $[a, a^\dagger] = 1$. This system is written by the harmonic oscillator Hamiltonian with resonant frequency of ω_0

$$H_{LC} = \frac{\Phi^2}{2L} + \frac{Q^2}{2C} = \hbar\omega_0 \left(a^\dagger a + \frac{1}{2} \right) \quad (2.2)$$

Here, the eigenstates of the Hamiltonian H_{LC} are represented as the Fock states $|n\rangle$ and the photon number as $\langle n | = a^\dagger a$.

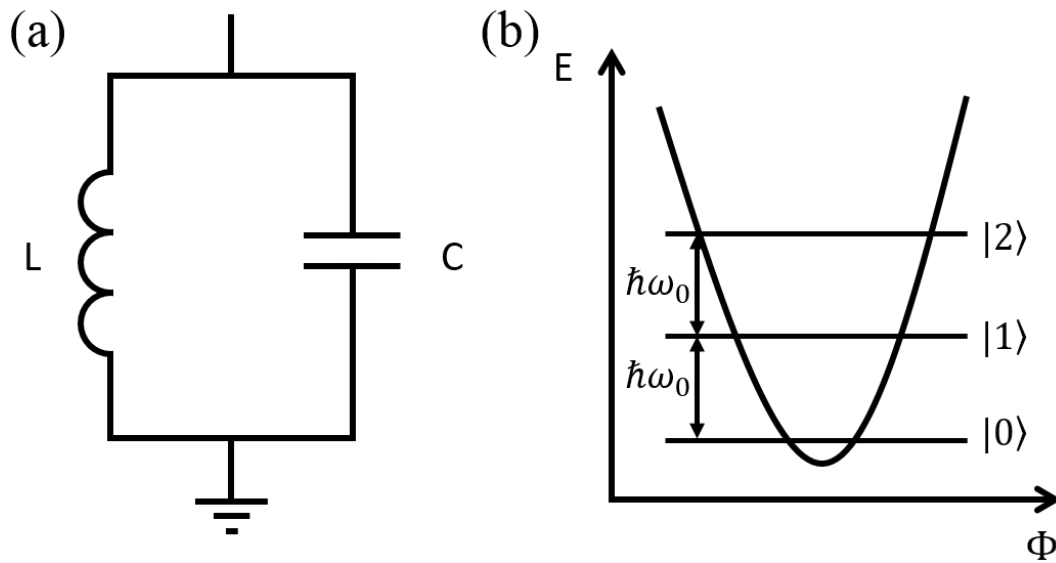


Figure 2.1 Representation of LC oscillators. (a) LC oscillator is composed of an inductor L and a capacitor C connected on both ends. (b) Energy difference of LC oscillator between two adjacent levels is same with the amount of $\hbar\omega_0$.

2.1.2 Josephson Junction

Josephson junction [6] consists of two superconductors separated by a thin insulator as shown in Fig. 2.2. The unique property of superconductor can be explained by Cooper pair according to BCS Theory [35]–[37]. Two electrons behave as a pair by attraction due to the distorted lattice ions. They can be expressed as

$$\Psi(r) = \Psi_0(r) \exp(i\varphi(r)) \quad (2.3)$$

where $\varphi(r)$ is a gauge-invariant phase. Due to very thin thickness of the insulator, the wave functions of both superconductors are overlapped and Cooper pair tunneling can happen across the insulating barrier.

The current through the junction is given by

$$I(t) = I_0 \sin(\delta(t)) \quad (2.4)$$

where I_0 is the critical current of junction and $\delta(t)$ the phase difference between two superconductors ($\delta(t) = \varphi_1(t) - \varphi_2(t)$). Also, the phase difference can be expressed by the integral form of

$$\delta(t) = \frac{1}{\varphi_0} \int_{-\infty}^t dt' V(t') \quad (2.5)$$

where φ_0 is the reduced flux quantum of $h/2e$.

In the superconducting circuit, the Josephson junction is widely used due to its nonlinearity on inductance. To describe the Josephson effect, another classical equation is needed

$$V(t) = \varphi_0 \frac{d\delta(t)}{dt} \quad (2.6)$$

where V is the voltage difference across the junction. By differentiating Eq. (2.4), it becomes

$$\frac{dI}{dt} = I_0 \cos(\delta(t)) \frac{d\delta(t)}{dt}. \quad (2.7)$$

Then, when $d\delta(t)/dt$ and dI/dt are replaced by using Eq. (2.6) and $V = L_J dI/dt$ respectively, the Josephson inductance L_J can be expressed as

$$L_J = \frac{\varphi_0}{I_0 \cos(\delta(t))}. \quad (2.8)$$

The cosine term in denominator makes the inductance nonlinear. This nonlinearity can give anharmonicity in energy level of qubit and make frequency mixing for parametric amplification. Also, the resonator having a tunable resonant frequency can be made. A method to change in the phase difference will be described in the following section.

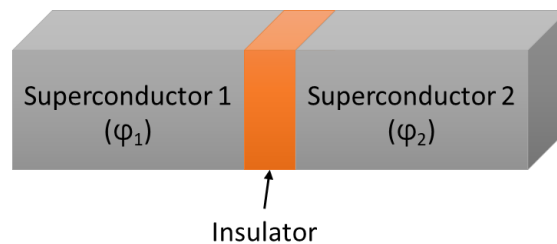


Figure 2.2 Representation of Josephson junction. Superconductors are separated by a thin insulator. Phase difference between two superconductors governs its electrical behaviors.

2.1.3 SQUID

Superconducting Quantum Interference Device (SQUID) [38] as shown in Fig. 2.3 consists of a loop of two Josephson junctions connected in parallel. The current flowing through the loop has a dependence on the applied magnetic field. It tunes the phase in the superconductor, and accordingly the phase difference $\delta(t)$ and the critical current I_0 between two superconductors.

If it is assumed that two junctions have identical critical current, the total current through SQUID can be expressed as

$$\begin{aligned} I &= I_0(\sin \varphi_1 + \sin \varphi_2) \\ &= 2I_0 \cos((\varphi_1 - \varphi_2)/2) \sin((\varphi_1 + \varphi_2)/2) \end{aligned} \quad (2.9)$$

The phase difference is given by line integral along a closed loop contour,

$$\varphi_1 - \varphi_2 = 2\pi\Phi / \Phi_0 \quad (2.10)$$

where Φ is the flux threading the SQUID loop. Then, the current is rewritten as

$$I = 2I_c \cos(\pi\Phi / \Phi_0) \sin(\varphi_1 + \pi\Phi / \Phi_0). \quad (2.11)$$

The maximum current I_0^S is just given by

$$I_0^S = 2I_c |\cos(\pi\Phi / \Phi_0)|. \quad (2.12)$$

When the critical current I_0 in the Josephson junction of Eq. (2.8) is replaced with the maximum current, I_0^S , it is found that that the SQUID inductance varies with the magnetic field, and so does the resonant frequency by the relation of $\omega = 1/\sqrt{LC}$.

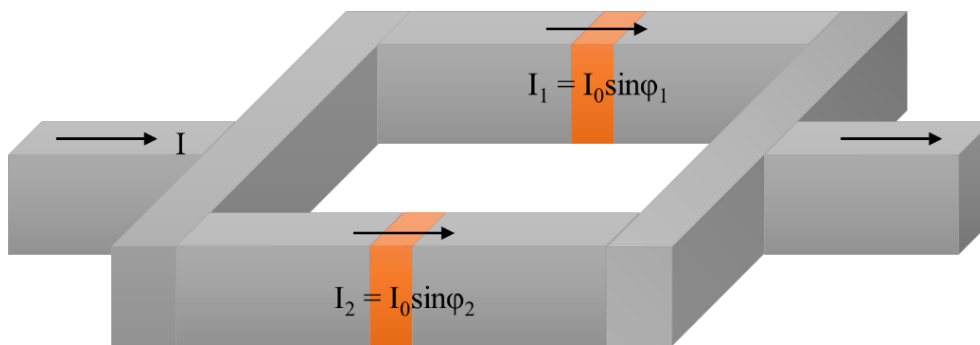


Figure 2.3 Schematic of SQUID. Two Josephson junctions in parallel form a loop, and its inductance is modulated by external magnetic flux.

2.2 Superconducting Qubits

Superconducting qubit is a good candidate of two-level system in respect to no dissipation for superconductor and nonlinearity for Josephson junction. By replacing the inductor with the Josephson junction in the LC oscillator, energy level spacing becomes uneven. Then, the circuit can be used as a qubit with the lowest two levels, such as ground and first excited states. In this section, quantum bit which is the most fundamental component in quantum computer is introduced. Among several types of superconducting qubits, transmon qubit is discussed. Then, circuit QED allows us to understand an interaction between atom and light.

2.2.1 Quantum Bit

Classical computers use either 0 or 1, which is called as ‘bit’. On the other hand, qubit, short for quantum bit, is used in quantum computer as a basic unit [39]. In addition to ground state $|0\rangle$ and excited state $|1\rangle$, superposition of two states are allowed. Generally, the quantum state composed of two level is represented by a wave vector

$$|\Psi\rangle = a|0\rangle + b|1\rangle \quad (2.13)$$

where a and b are complex number, satisfying normality condition of $|a|^2 + |b|^2 = 1$. Also, $|a|^2$ (or $|b|^2$) is probability where qubit is in ground (or excited) state. As a consequence, a system of n qubit can be written in the same manner

$$|\Psi_n\rangle = |\varphi_n\rangle \otimes |\varphi_{n-1}\rangle \otimes \dots \otimes |\varphi_1\rangle \quad (2.14)$$

with $|\varphi_i\rangle \in \{0,1\}$.

The two-level system is simply represented with a point on a unit sphere, called as Bloch sphere representation. Although there is global phase factor $e^{i\gamma}$, it is usually omitted due to no observable effect. Again, the quantum state can be expressed in a polar coordinate

$$|\Psi\rangle = \cos(\theta/2)|0\rangle + e^{i\phi} \sin(\theta/2)|1\rangle \quad (2.15)$$

where θ is in a range from 0 to π and ϕ from 0 to 2π . An arbitrary quantum state can be represented as a point on Bloch sphere as shown in Fig. 2.4.

Density matrix is another representation for quantum states, which is given by $\rho = |\Psi\rangle\langle\Psi|$ for pure states and $\rho = \sum_i p_i |\Psi_i\rangle\langle\Psi_i|$ for mixed states. This representation is useful to describe the mixed state because the wave vector representation only gives information of the pure state. The density matrix follows three general properties; (1) ρ is Hermitian, (2) $\text{tr}(\rho) = 1$, and (3) ρ has non-negative eigenvalues. This density matrix formalism is especially used for showing ensemble of quantum states and multi-qubit quantum states. For example, the single qubit system is described as 2×2 matrix with

$|0\rangle$ and $|1\rangle$ bases and n -qubit system as $2^n \times 2^n$ matrix. Also, it is allowed to express the expectation value of operator A as

$$\langle A \rangle = \sum_i p_i \langle \Psi_i | A | \Psi_i \rangle = \text{tr}(\rho A). \quad (2.16)$$

These properties are used to estimate the quantum state as density matrix from a set of ensemble measurements in quantum state tomography (QST).

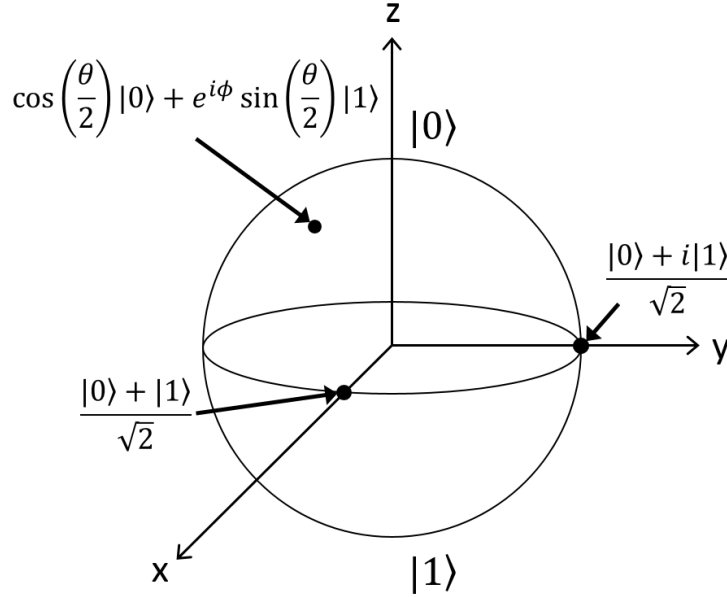


Figure 2.4 Bloch sphere representation. The quantum state is visually shown as a point on a unit sphere. Ground state $|0\rangle$ is in $+z$ direction and excited state $|1\rangle$ in $-z$ direction. The superposition of two possible states can be represented with polar coordinates.

2.2.2 Transmon Qubit

When an inductor of LC oscillator in section 2.1.1 is replaced by nonlinear inductor, or Josephson junction (Fig. 2.5(a)), the energy level between neighboring states is spaced unequally as shown in Fig. 2.5(b). The following Hamiltonian with the nonlinear Josephson inductance is written as

$$H = 4E_C n^2 - E_J \cos(\phi) \quad (2.17)$$

where n is the number of Cooper pairs ($n = Q / 2e$) and ϕ the phase related to the magnetic flux ($\phi = 2\pi\Phi / \Phi_0$). In this scheme, the Josephson ($E_J = \Phi_0 I_C / 2\pi$) and charging energies ($E_C = e^2 / 2C$) are stored in the inductor and capacitor, respectively [14]. For very small fluctuation in ϕ , the Hamiltonian to the first order except for the constant term can be written as

$$H \approx 4E_C n^2 + E_J \phi^2. \quad (2.18)$$

When the ratio between two energies E_J/E_C is greater than 50, it is called as transmon qubit where the energy level becomes flat and there are no sweet spots [14].

Here, the m th order energy can be given by

$$E_m = m\sqrt{8E_J E_C} - \frac{E_C}{12}(6m^2 + 6m + 3). \quad (2.19)$$

Then, the energy difference between two neighboring energy levels is

$$E_m - E_{m-1} = -mE_C, \quad (2.20)$$

and for the first two levels, the energy difference ($E_{21} - E_{10}$) is equal to $-E_C$, known as an anharmonicity α . Based on this relation, the anharmonicity can be controlled with different charging energy. The charging energy can be differed by varying a shunt capacitance (C_S) and a gate capacitance (C_G). For the transmon in 3D cavity, the shunt capacitance is related to the pad outside the Josephson junction.

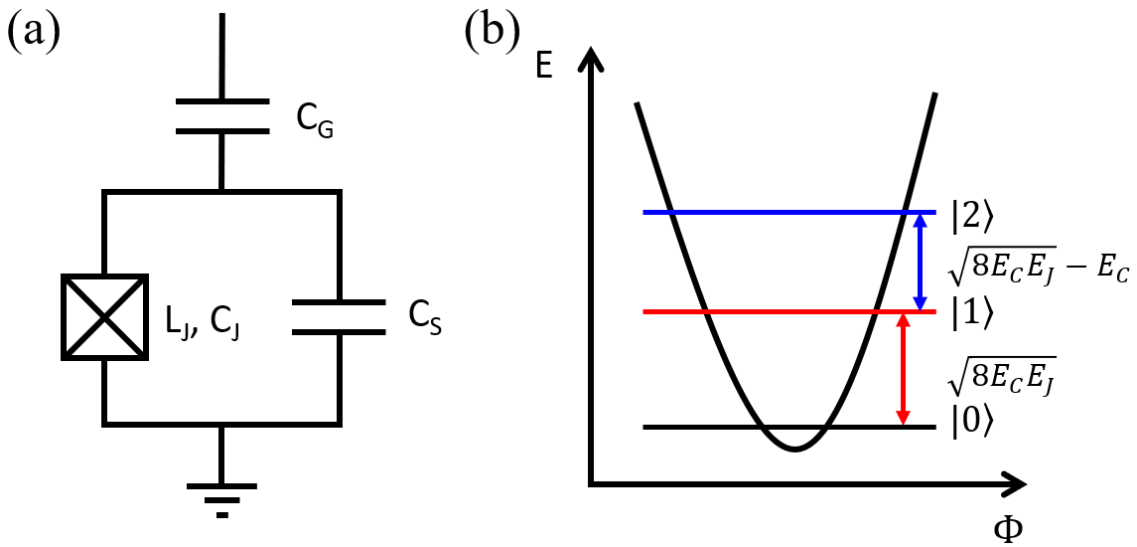


Figure 2.5 Representation of transmon qubit. (a) To realize the transmon qubit in circuit diagram, a linear inductor is replaced with nonlinear Josephson inductor. The charging energy E_C can be varied with gate capacitor and shunt capacitor. (b) Due to the nonlinearity of the Josephson junction, the energy spacing between two adjacent energy levels is uneven with amount of anharmonicity α .

2.2.3 Circuit QED

Basic concepts of circuit quantum electrodynamics (QED) is extended from cavity QED [40], [41]. The cavity QED is used to study an interaction between light and atom. The reflective mirrors of cavity make photons trapped in the cavity, increasing the interaction strength between light and atom. The schematic of the cavity QED is shown in Fig. 2.6. The photons inside the cavity escape with the rate κ , the atom decays with the rate γ , and they interact each other with coupling strength g . The circuit QED is an application of the cavity QED to the superconducting electrical circuits [16], [42], [43]. The atom and cavity in the cavity QED correspond to superconducting qubit and resonator, respectively. This concept has been used in all over the superconducting qubit system in readout [44], qubit coupling [45], quantum algorithms [46], and quantum error corrections [47]. Also, quantum-limited amplifier for readout of superconducting qubits, such as Josephson parametric amplifier (JPA), has been developed within circuit QED.

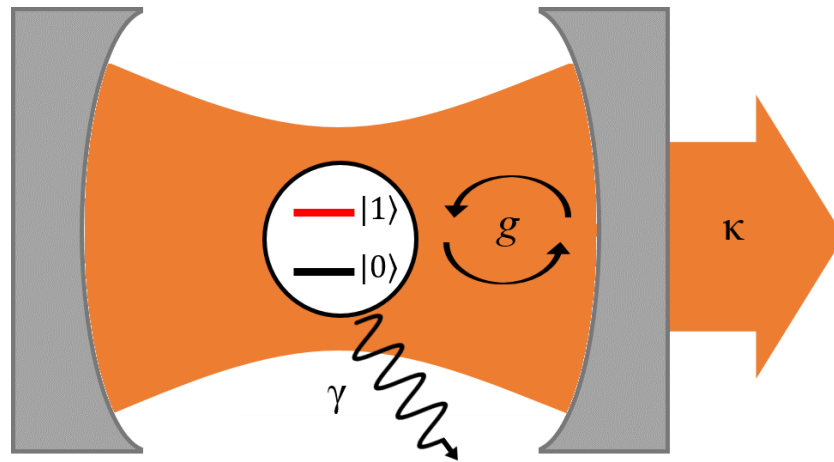


Figure 2.6 Schematic of cavity QED. The cavity QED is applied for an interaction between a real atom and optical cavity. On the other hand, the circuit QED is used for the system consisting of a superconducting artificial atom and resonator. In both cases, the quantum behavior can be explained by coupling strength g , atomic decay γ , and photon decay κ .

Chapter 3 . Metal/Semiconductor Junction

Metal/Semiconductor junction has been used widely for device applications. This chapter introduces the basics of ideal metal/semiconductor junction and classifies the junction in two ways: ohmic and Schottky. Various methods are presented to extract the Schottky barrier height (SBH) that is the most important parameter in the Schottky junction.

3.1 Energy Band Theory

The electron in solid has the energy band instead of discrete energy level due to the influence of neighbor atoms. The energy band consists of mainly three bands as shown in Fig. 3.1. The valence band consists of the energies of the outermost electrons, and the electrons are bound weakly to the nucleus of atom. On the other hand, the conduction band is empty generally and filled with electrons by external energy and the electrons move freely. Between them, there are the energy levels for electrons not to be allowed and it is called as ‘forbidden gap’ or ‘band gap’.

Depending on this energy band structure, the solid is classified into conductor, semiconductor, and insulator as in Fig. 3.2. In conductor, the conduction band and valence band are overlapped, and the electrons become easily free from the nucleus. In insulator, meanwhile, the flow of electrons is not allowed due to the large band gap. Semiconductor shows the electrical properties between these two materials. There is small band gap and electrons can move to the conduction band with a certain external energy.

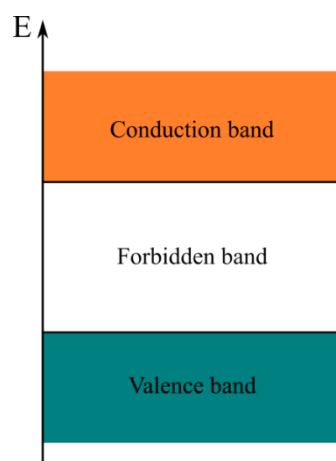


Figure 3.1 Energy band for electrons. In solid, electrons have energy band due to the influence of neighbor atoms.

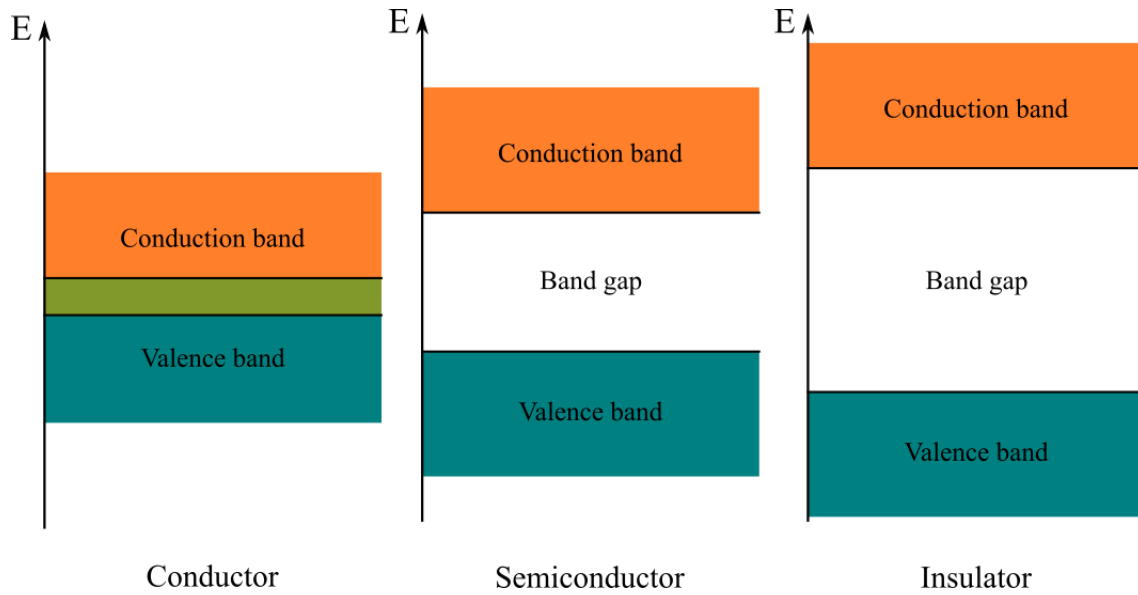


Figure 3.2 Classification of solids. Depending on the magnitude of band gap, the solid can be categorized into conductor, semiconductor, and insulator.

3.2 Ideal Metal/Semiconductor Junction

When two different materials are in contact, they form a junction and affect the total electrical properties. Each material has different Fermi level and the junction is formed in the way that the Fermi levels are aligned, or equilibrium. The situation when metal and n-type semiconductor are electrically isolated is depicted in Fig. 3.3(a). With the vacuum level as a reference, Φ_M and Φ_S are the work functions of metal and semiconductor, respectively and χ_S is the electron affinity of semiconductor. The junction can be classified as either Ohmic or Schottky [48]:

1. Ohmic when $\Phi_S > \Phi_M$
2. Schottky when $\Phi_S < \Phi_M$

In the Ohmic contact, the current can flow with no barrier and the junction follows the Ohm's law having a linear relation between the current and the voltage. On the other hand, the Schottky junction has an energy barrier, called 'Schottky barrier', which is defined as the difference between the electron affinity of semiconductor and the work function of metal. Due to this energy barrier, it shows a rectifying behavior, and it will be described in detail in the rest of this chapter.

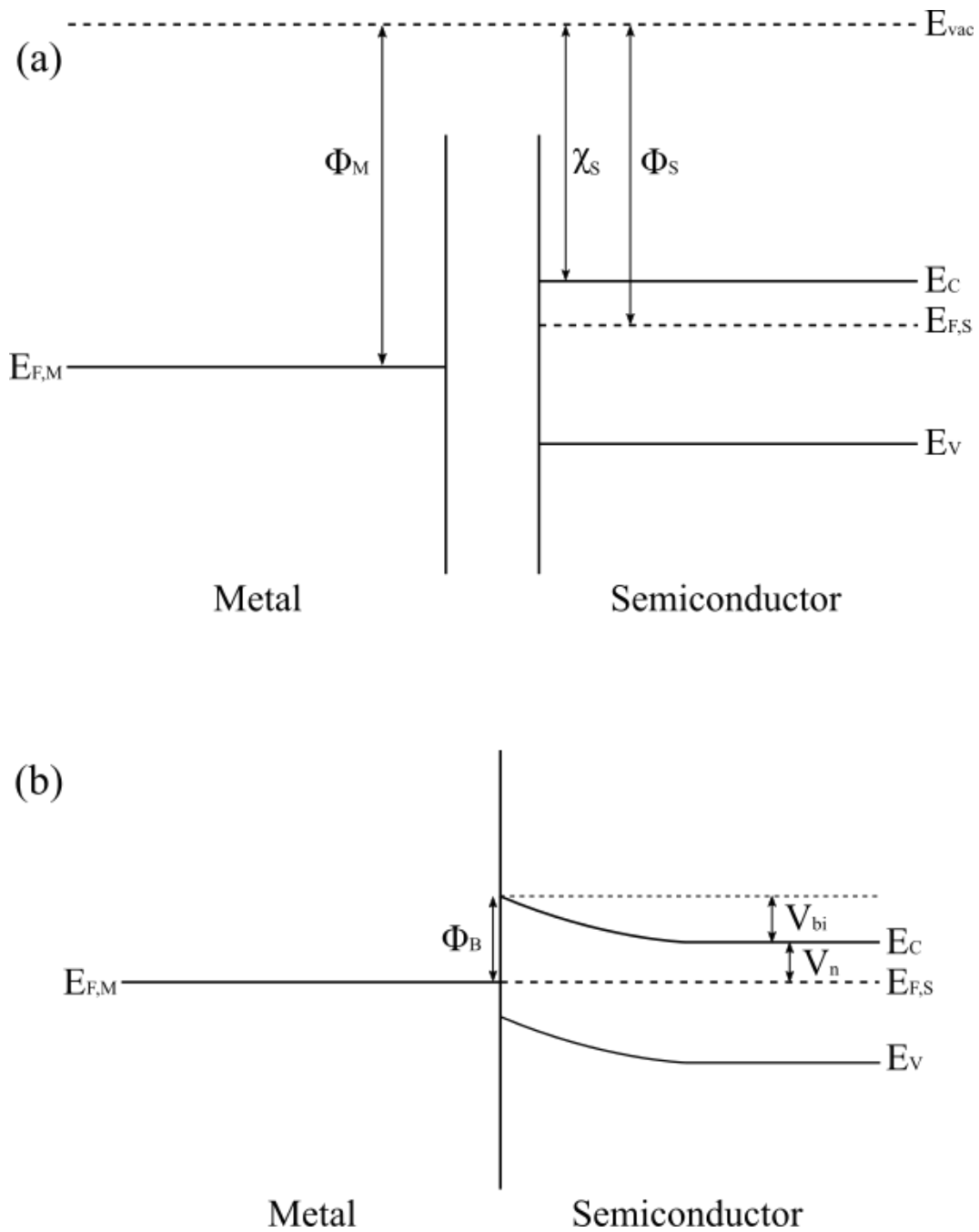


Figure 3.3 Energy band diagram of metal/semiconductor contact. The metal and the semiconductor are (a) electrically isolated with a large gap and (b) in contact with electrical connection. The Fermi levels of two materials are aligned and as a result, the band bending occurs.

3.3 Schottky Junction

In case the work function of the metal is larger than the electron affinity of the semiconductor, the junction becomes Schottky contact and the energy barrier, or Schottky barrier, formed in the process of the Fermi level alignment allows electron flow in a direction. The energy band diagram of a metal/n-type semiconductor junction is illustrated in Fig. 3.3(b). The electrical properties of the junction are mainly determined by the SBH because the electron flow is controlled by the Schottky barrier. Therefore, the Schottky barrier is a crucial parameter in the junction and its height can be measured with I-V measurement, C-V measurement, and IPE method.

3.3.1 I-V Characteristic

Current-voltage measurements is mainly used to estimate threshold voltage, leakage current, and critical breakdown field. The Schottky junction shows the rectifying behavior due to the energy barrier as shown in Fig. 3.4(a). The junction shows dissimilar I-V behavior depending on the direction of applied voltage. When forward bias is applied, electrons move from metal to semiconductor and current increases exponentially with the increase of the bias. On the other hand, the current hardly flows before the breakdown voltage because the Schottky barrier hinders the electron transfer. The I-V characteristics are explained by the thermionic emission theory [49], [50]. The current density over the Schottky barrier near threshold region at temperature T is given by

$$J = J_s \exp\left(\frac{qV}{nk_B T} - 1\right) = A^* T^2 \exp\left(-\frac{q\phi_B}{k_B T}\right) \exp\left(\frac{qV}{nk_B T} - 1\right) \quad (3.1)$$

where J_s is the reverse saturation current, A^* the effective Richardson constant, q the electric charge, k_B the Boltzmann constant, ϕ_B the SBH, V the applied bias, and n the ideality factor.

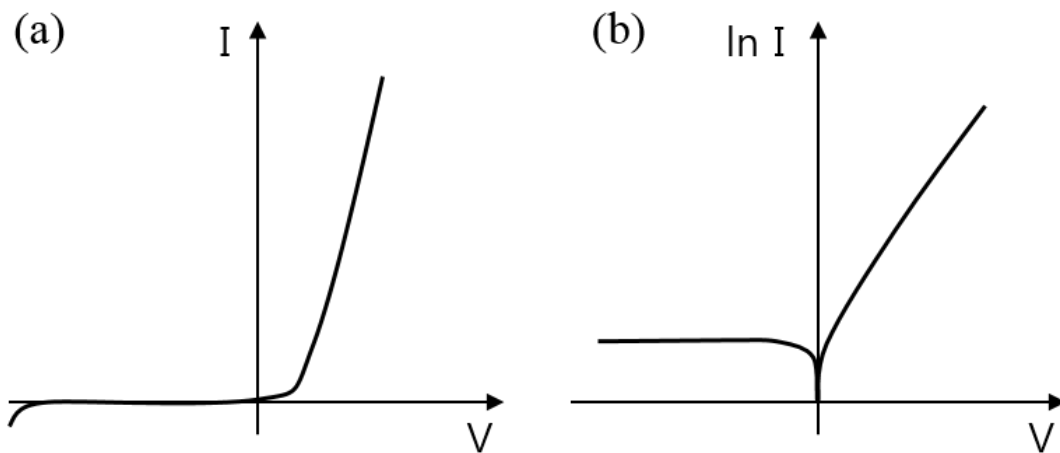


Figure 3.4 I-V characteristics of Schottky junction. (a) Rectifying property in the linear scale and (b) semi-log characteristic of the Schottky junction.

For $V \gg k_B T / q$, the equation can be approximated as

$$J \cong J_s \exp\left(\frac{qV}{nk_B T}\right). \quad (3.2)$$

Then, two important I-V measurement parameters can be obtained by taking the semi-log to both sides of Eq. (3.2) and the plot is shown in Fig. 3.4(b). The SBH can be estimated from the intercept of $\ln J$, or J_s , and expressed as

$$\phi_B = -\frac{k_B T}{q} \ln\left(\frac{A^* T^2}{J_s}\right). \quad (3.3)$$

Also, the ideality factor n can be determined using the slope of linear region of the plot and works as an indicator of ideal Schottky junction. This parameter is unity when the junction is ideal and becomes larger than 1 for non-ideal junction. The experimental results will be discussed later in chapter 5.

3.3.2 C-V Characteristic

Capacitance-Voltage measurement is a powerful tool to characterize an interface of semiconductor devices. The capacitance is measured by applying a small AC voltage superimposed on a DC bias. The AC signal makes charge variation and the DC bias induces the semiconductor in the state of inversion, depletion, or accumulation. To characterize the Schottky junction, a positive voltage is applied on the semiconductor, which is a reverse voltage condition, and the depletion region is formed on the semiconductor side by pushing electrons to the end of the region.

Schottky junction has a depletion capacitance and the depletion region works as an insulating layer in the capacitor because there is no free charge carrier. Here, it is assumed that the depletion approximation works on the system and the dithering AC voltage is small enough to show approximately linear differential capacitance. The depletion width varies with the applied voltage according to

$$W_D = \sqrt{\frac{2\varepsilon_s \varepsilon_0}{qN_D} \left(V_{bi} - V - \frac{k_B T}{q} \right)}, \quad (3.4)$$

where N_D is the donor density in the n-type semiconductor, ε_s the dielectric constant of semiconductor, ε_0 the vacuum permittivity (F/m), and V_{bi} the built-in potential [51]. Then, the depletion capacitance changes with the applied voltage. The relation between the capacitance and the voltage [51] can be written as

$$\frac{1}{C^2} = \frac{2}{qN_D \varepsilon_s \varepsilon_0 (\phi_B - \zeta + V - k_B T / q)}, \quad (3.5)$$

where ζ is the energy difference between the Fermi level (E_F) and the conduction band minimum (E_C) of the bulk semiconductor. From Eq. 3.5 and its plot, two electrical parameters can be extracted. First, the donor density can be obtained from the slope of the linear fitting line and it is given by

$$N_D = \frac{2}{q\epsilon_s\epsilon_0} \frac{1}{d(1/C^2)/dV} \quad (3.6)$$

Second, the Schottky barrier (ϕ_B) can be expressed by the relation of

$$\phi_B = -V_{bi} + \zeta + k_B T / q \quad (3.7)$$

and the built-in potential V_{bi} can be extracted from V_R -intercept of the linearly fitted line.

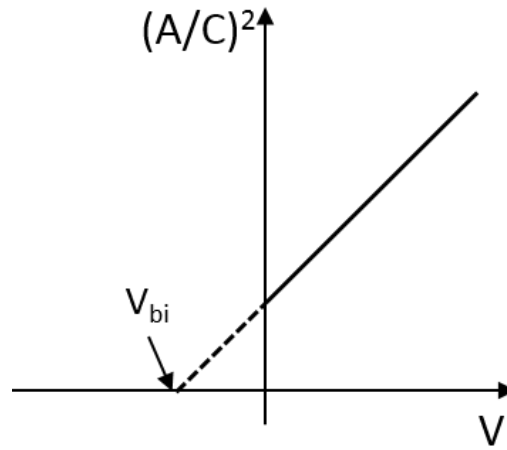


Figure 3.5 C-V characteristics of Schottky junction. The intercept to the reverse voltage axis implies built-in potential, V_{bi} .

3.3.3 IPE Characteristic

Lastly, the SBH can be determined by internal photoemission technique. This method is useful to characterize the electron transport properties because it detects directly the transfer of electrons over the Schottky barrier [52]. It is similar to (external) photoemission effect that an incident light makes the electrons in the metal to be excited and emitted into vacuum. In this case, since the energy barrier is formed at the surface of a solid for the external photoemission, the electrons need more energy to overcome the barrier. Meanwhile, the internal photoemission occurs at the interface of two different solids and electrons can be emitted with less photon energy.

The process of the IPE is summarized in Fig. 3.6(a). When the light with enough large energy ($h\nu > q\phi_B$) is injected to the metal, the electrons are excited and reach the interface of metal and semiconductor. Then, they surmount the energy barrier and are detected by the collector. Finally, the

SBH can be estimated.

The SBH can be estimated using so-called Fowler plot following an approximate Fowler's Formula [53]–[55]

$$Y \cong A(h\nu - q\phi_B)^2 \quad (3.8)$$

where Y is photo-yield, ν the frequency, A the material dependent constant. Constant A is differed by Fermi energy, scattering probability of hot electrons in the metal and crystalline defects at the interface [56]. Yield implies the ratio between the number of electrons to be escaped and the number of photons to be absorbed for a given energy. Based on Eq. 3.8, the SBH can be extracted from the extrapolation of the linear region in $Y^{1/2}$ vs. $h\nu$ plot as in Fig. 3.6(b).

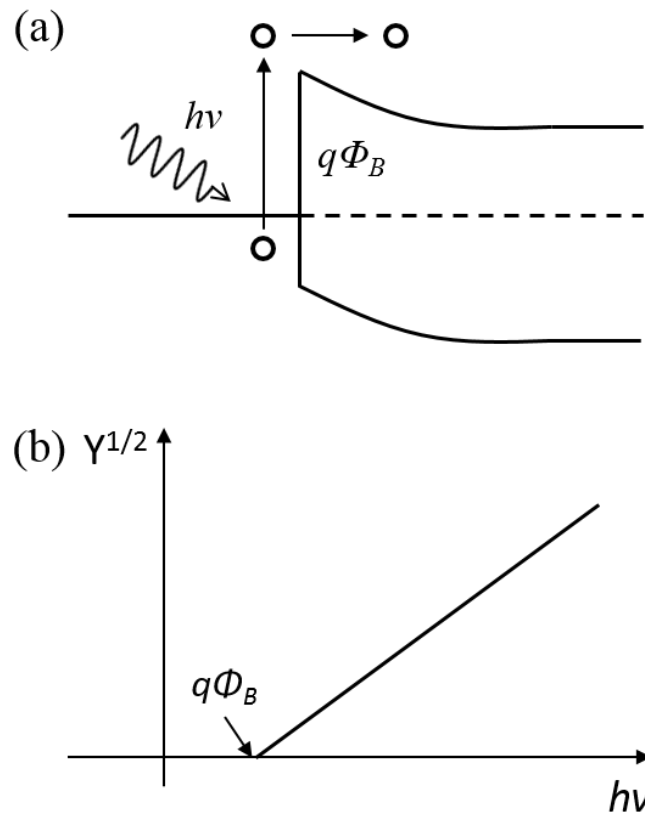


Figure 3.6 IPE characteristics of Schottky junction. (a) Mechanism of detecting photocurrent and (b) the extraction of Schottky barrier height in $Y^{1/2}$ vs. $h\nu$ plot.

3.4 Silicon Carbide

Silicon carbide (SiC) is one of the alternative materials over Silicon (Si) in semiconductor industry due to wide band gap energy and low intrinsic carrier concentration. Especially, it is useful in the area of high temperature, high power, and high frequency devices. With these superior properties, it can be applied to rectifiers, switches, amplifiers, and microwave power devices. In last few years, Nitrogen-Vacancy (NV) centers in SiC have been studied theoretically [57], [58] and proven experimentally [59]–[61]. An overall material and electrical properties of SiC are given in this subchapter. Also, the polytypes of SiC and spontaneous polarization (SP) in the hexagonal structure are introduced.

3.4.1. Structural Properties

SiC is IV-IV compound semiconductor where Si and C atoms are connected with strong sp^3 bonds in tetrahedron structure as shown in Fig. 3.7. The Si and C atoms are covalently bonded and separated by 1.89 Å, and the distance between neighboring C atoms is 3.08 Å. In such binary system, there can be many different crystal structures known as ‘polytypes’ and electrical properties varies depending on the polytypes [62]–[64]. SiC has more than 200 polytypes, but only few types, including 3C-, 2H-, 4H-, 6H-, and 15R-SiC, have been mainly used. Here, the name of polytypes follows the Ramsdell notation [65] where the first number implies the total number of layers in a unit cell and the followed letters represents the lattice types. For example, C is denoted for cubic, H for hexagonal, and R for rhombohedral structure. The structure of polytypes are determined by stacking sequence of SiC bilayers and a few examples are shown in Fig. 3.8. The stacking sequence of 3C-SiC is expressed as (ABC)(ABC)..., that of 4H-SiC is (ABCB)(ABCB)..., and that of 15R-SiC is (ABCBACABACBCACB) (ABCBACABACBCACB)... [62]–[64]. These structural factors are the reason for the SiC to show different material properties.

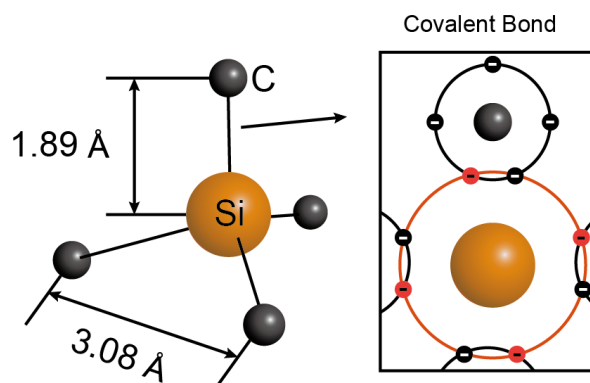


Figure 3.7 Tetrahedral structure of SiC and covalent bond between Si and C atoms

3.4.2. Electrical Properties

Even though SiC has several polytypes, they show three common electrical properties: high temperature, high power, high frequency [66]. First, the SiC device can operate at high temperature because of low intrinsic carrier concentration (n_i) and wide energy band gap ($E_g = 3.23$ eV). The intrinsic carrier concentration and temperature are related to

$$n_i = \sqrt{N_C N_V} \exp\left(-\frac{E_g}{2k_B T}\right). \quad (3.9)$$

According to the relation, the intrinsic carrier concentration increases with temperature increase and then it induces undesired leakage current. Since the SiC has inherently low intrinsic carrier concentration compared to Si at same temperature, it is useful to operate in high temperature [67], [68]. Also, when the band gap is wide, the carriers needs more energy to be excited to the upper band, and it prevents the carrier leakage. Next, the SiC devices can be operated with high power due to high electric breakdown field ($\sim 10^6$ V/cm) [67] and high thermal conductivity (2.3–4 W/cmK) [68]. High electric breakdown field imply that the depletion width is very short, and the device shows low resistance because dopants are concentrated in a thin region and then the resistance become low. Finally, the delay time in high speed device is affected by the depletion width. With the narrow depletion width, the carrier transport become high and fast. Therefore, the SiC can be used as high frequency device.

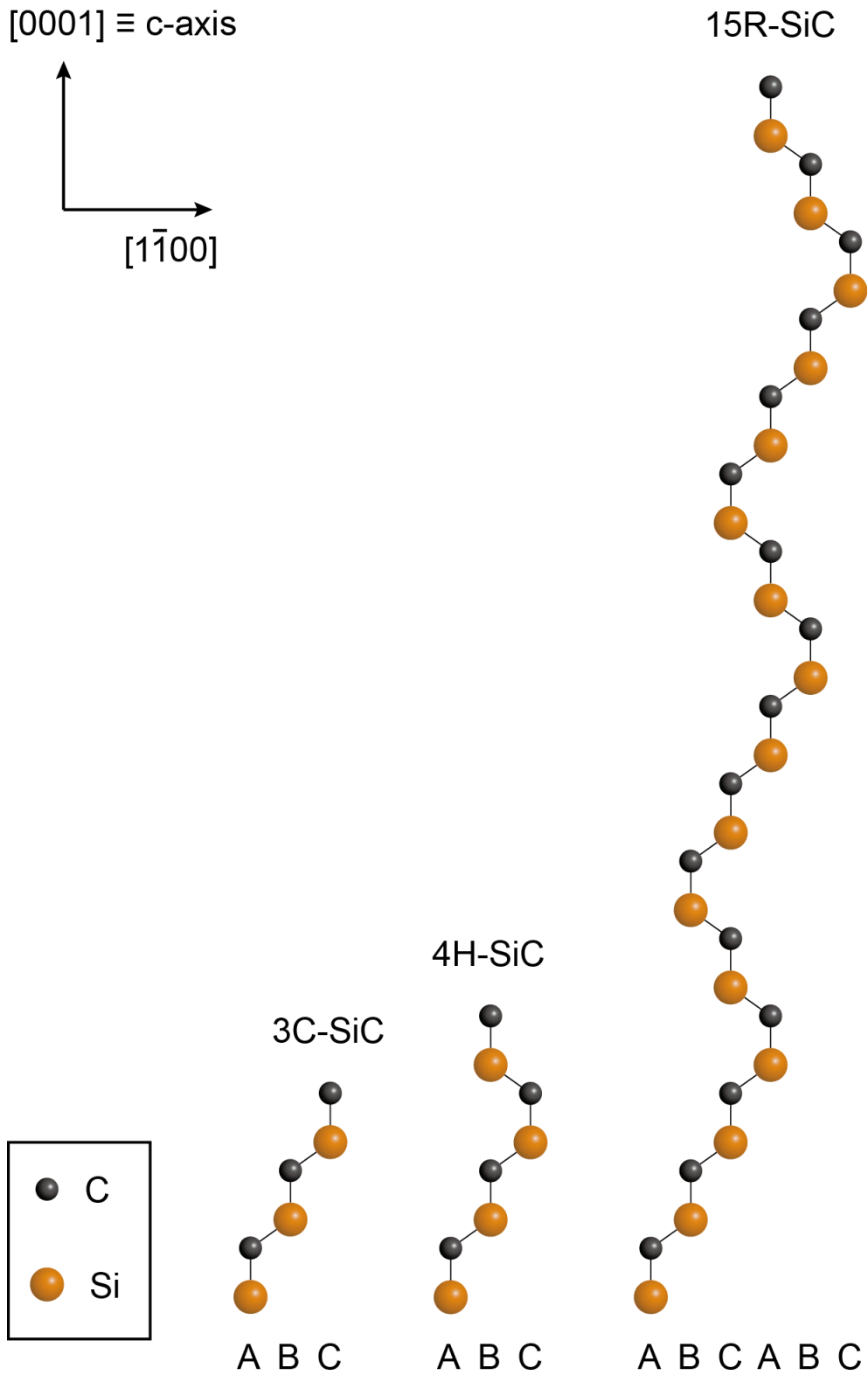


Figure 3.8 Stacking sequence of SiC bilayers representing polytypes: (a) 3C-SiC (b) 4H-SiC (c) 15R-SiC.

3.4.3 Spontaneous Polarization

As described above, the SiC shows various crystal structures depending on the stacking sequence of the SiC bilayers. Among many polytypes, the SiC composed of hexagonal structure has an exceptional property, called as spontaneous polarization (SP), compared to cubic-structure SiC [69]. The difference arises from the crystal symmetry. The cubic structure has symmetry and 4 sp^3 bonds have equivalent length. On the other hand, the symmetry is broken in the hexagonal structure and the bonds are divided in two types as one L-bond and three T-bonds as shown in Fig. 3.9. The L-bond is a longitudinal bond along the c-axis ([0001]) and a little bit large from the cubic-structure case. The remained three T-bonds are transverse bonds and a little bit shorter than the equivalent case. Therefore, the equivalence of the tetrahedral structure is not kept, and electron density is redistributed. The Si atom becomes positively charged and the C atom negatively charged. Then, the SP is formed in the opposite direction to the c-axis. According to S. Yu. Davydov *et al.* [69], the hexagonalities of 2H-, 4H-, 6H-, and 8H-SiC are estimated as 1, 0.50, 0.33, and 0.25, respectively and the calculated SP is proportional to these values.

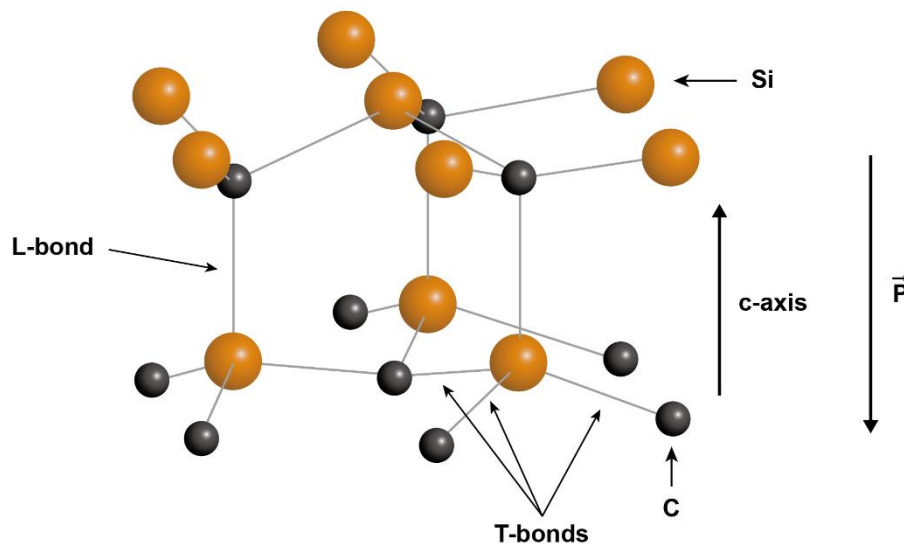


Figure 3.9 Formation of SP due to the broken equivalence of tetrahedral bonds.

Chapter 4 . Sample Fabrication

This chapter describes the fabrication techniques to be used for metal/semiconductor junctions and superconducting circuits. The measurement setups to characterize the electrical properties of the Schottky junction will be presented. Then, design and holder of the superconducting circuits are described. The cryogenic setup is discussed to measure the superconducting circuits, including input/output lines and dc line. At the end, the homodyne measurement to characterize quantum state such as vacuum state and squeezed state, is presented.

4.1 Fabrication of Metal/Semiconductor Junction

The metal/semiconductor junctions are fabricated with more than 10 circular patterns. The dot patterns are formed by using shadow mask or photolithography. The shadow mask is used for the samples with interlayer such as Al_2O_3 film and graphene. On the other hand, the photolithography is used twice to fabricate capacitive memory junction. One is for floating metal patterns and the other for top electrodes with smaller patterns. A common process of ohmic contact formation for both cases is described to be used for characterizing two-terminal devices. Then, the graphene transfer method and the measurement setups are followed.

4.1.1 Ohmic Contact

Ohmic contact is formed to measure the electrical properties of Schottky junction. It is essential to achieve ohmic contact with low resistance to show characteristics of Schottky junction definitely. In the experiments, silicon carbide is used, consisting of normally doped epilayer ($\sim 10^{15} \text{ cm}^{-3}$) grown on highly doped substrate ($\sim 10^{18} \text{ cm}^{-3}$). In the case, epilayer is terminated by Si atoms (Si-face) and substrate by C atoms (C-face). The Schottky junctions are formed on the Si-face of SiC and the other side of the SiC is used for ohmic contact formation. The substrate shows better ohmic resistance due to its high doping concentration.

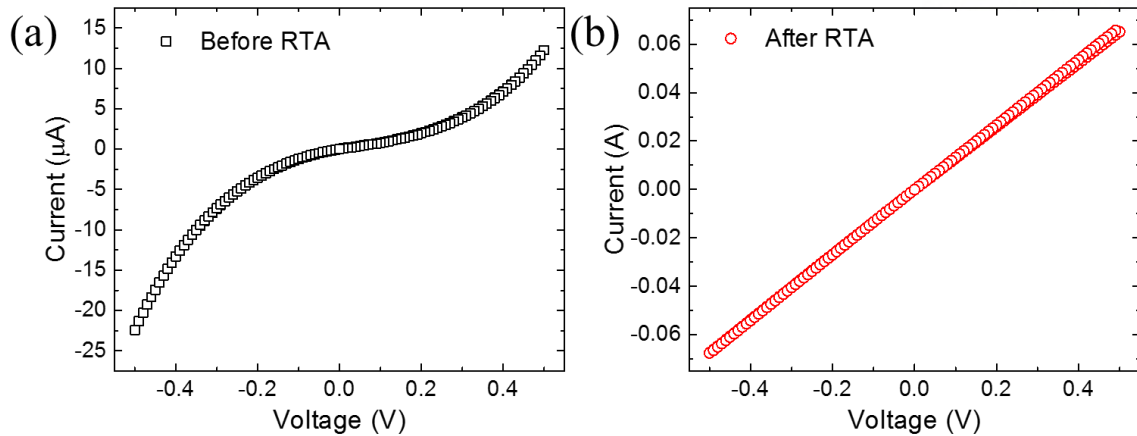


Figure 4.1 I-V characteristics of Ohmic contact (a) before and (b) after RTA. The junction becomes ohmic and has resistance of $\sim 10 \Omega$.

Ohmic contact with low resistance is achieved by depositing Ni electrodes and annealing it at high temperature [70]. Before the processes, the sample is cleaned using ultrasonication with two solvents such as acetone and methanol and then, the native oxide SiO_2 grown on SiC is etched by dipping it into 49 % of HF solution. The Si-face SiC is protected with 100 nm SiO_2 oxide layer by using plasma enhanced chemical vapor deposition (PECVD) because ohmic contact will be formed on the opposite side. In advance of Ni deposition, the SiO_2 grown in the previous process is removed with diluted HF solution (1:10 for 49 % HF : DI water) for 20 s. On the cleaned C-face, the Ni film of 100 nm thickness is deposited by using e-beam evaporator through shadow mask. The I-V characteristic of ohmic contact right after the electrode deposition is shown in Fig. 4.1(a). The current and voltage are not linearly related, which means that the contact is not yet ohmic. The sample is annealed by using rapid thermal annealing (RTA) method at 1000 °C for 90 s. After annealing the sample, the contacts show the linear I-V characteristics as shown in Fig. 4.1(b) and its resistance is in a range of 5 ~ 30 Ω . The ohmic contact is remained as same during an additional HF etching conducted before Schottky junction formation.

4.1.2 Graphene Transfer

In the experiment, graphene is transferred on the substrate by using dry transfer method [71] that has an advantage of less water molecules trapped on graphene. The CVD graphene on Cu foil is cut into smaller size than the sample and then spin-coated with PMMA 495 A2 at 5000 rpm for 1 min. In general, graphene is grown on both sides of Cu foil so, the opposite side is etched by using RIE in oxygen atmosphere with plasma power of 20 W and duration of 60 s. Then, the Kapton tape, which makes the difference from the wet transfer method, is attached on the top of PMMA/graphene/Cu foil. Since new supporter for graphene is used, Cu is etched by using ammonium persulfate. The Kapton tape/PMMA/graphene is rinsed with DI water repeatedly, dried with N₂ blowing, and then heated at 70 °C for 15 min. Before the graphene transfer, the substrate is cleaned with solvents and HF in advance to remove native oxide and residual organics on it. By handling the Kapton tape/PMMA/graphene with tweezers, it is transferred on the substrate. For uniform transfer, N₂ blow is conducted to the center of the sample and then heat it at 150 °C for 15 min. The sample is dipped into acetone to remove PMMA and accordingly Kapton tape is detached due to no connection to graphene/substrate. The sample is rinsed with IPA and heated again at 200 °C for 15 min to remove residuals. The transferred graphene is confirmed by using Raman spectroscopy and the spectrums are shown in Fig. 4.2. For general Raman spectrum of graphene, two peaks of G peak and 2D peak appear near 1580 cm⁻¹ and 2670 cm⁻¹, respectively. However, in this case, G peak is disturbed with SiC peak because graphene is transferred on the SiC substrate.

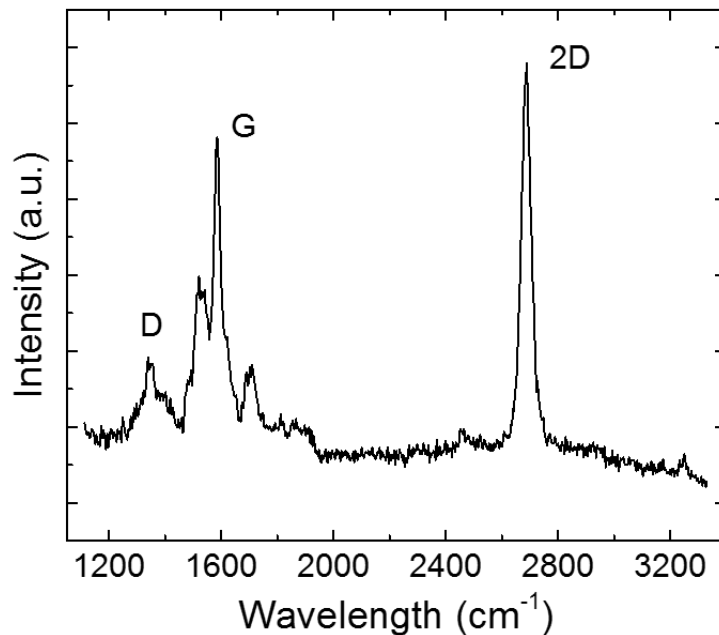


Figure 4.2 Raman spectrum of graphene transferred on SiC substrate. SiC peaks are observed in a range of 1300 ~ 1700 cm⁻¹.

4.2 Setup for Experiments with Schottky Junction

The probe station is designed to measure the samples by changing the measurement methods (I-V, C-V, and IPE) with a single contact as shown in Fig.4.3. Therefore, the sample can be characterized without variations in contact properties. When the sample is mounted, the I-V characteristics are measured first using KEITHLEY Current Amplifier (Model 428) that can amplify current signal and apply bias, simultaneously. It is checked whether the contact is stable and the turn-on voltages. Then, the C-V measurement is followed with an Agilent E4980 LCR meter. For the Schottky junction, voltage is applied on the substrate and ground on the metal electrode to observe the reverse voltage characteristics of sample. In this measurement, the junction quality is estimated with dissipation factor (D). It is an indicator of loss or inefficiency and the sample is lossless with low D. The last measurement is IPE which needs additional tools of laser to light the sample. Based on the SBH values obtained from the I-V and C-V measurement, the energy range is determined, and the corresponding fiber and filter is changed.

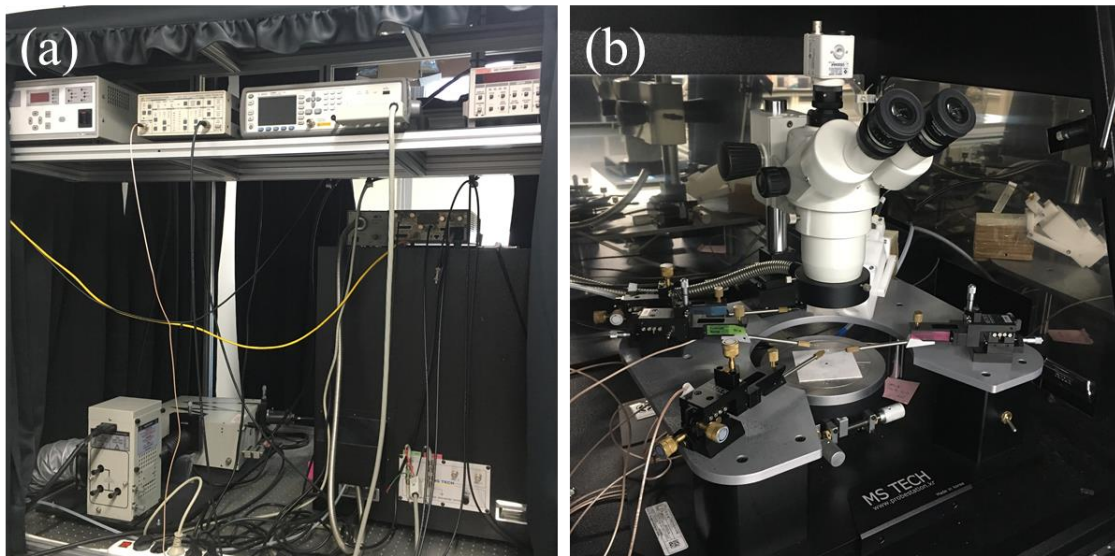


Figure 4.3 Measurement setup for metal/semiconductor junctions. (a) I-V, C-V, and IPE systems and (b) probe station.

4.3 Design and Measurement of Superconducting Circuit

In circuit QED, the operational parameters such as resonator frequency and qubit transition frequency are modulated depending on the design and fabrication of the circuits. The resonator can be presented by a transmission line or lumped elements. The most used form of the transmission line is a co-planar waveguide (CPW). The designed resonator can be coupled with outer ports through coupling capacitor. The capacitor can be formed by stacking metal and insulators or designing an interdigitated capacitor. Since the metal electrodes are on a same plane in the interdigitated capacitor, it has advantage of fabrication. Through these processes, the superconducting circuits are designed and fabricated. The samples are measured by dipping it into liquid He at ~ 4.2 K and also mounting it on the dilution fridge at ~ 10 mK.

4.3.1 CPW Structure

To propagate a signal from one point to another, a connection is necessary and is called transmission line in an electronic system [72]. The transmission line resonator has been used in various areas of circuit QEDs, such as quantum bus [73] and photon storage [74]. An infinitesimal part of transmission line consists of capacitance, inductance, resistance, and conductance as shown in Fig. 4.4(a). These values are determined by the transmission line design. According to Kirchoff's voltage and current law, the circuit can be expressed as

$$-\frac{\partial V(z,t)}{\partial z} = R_0 I(z,t) + L_0 \frac{\partial I(z,t)}{\partial t} \quad (4.1)$$

$$-\frac{\partial I(z,t)}{\partial z} = G_0 V(z,t) + C_0 \frac{\partial V(z,t)}{\partial t} \quad (4.2)$$

where R_0 , L_0 , G_0 , and C_0 are the resistance, inductance, conductance and capacitance per unit length, respectively.

By using $V(z,t) = \text{Re}[V_s(z)e^{j\omega t}]$ and $I(z,t) = \text{Re}[I_s(z)e^{j\omega t}]$ where V_s and I_s are the phasor form of $V(z,t)$ and $I(z,t)$, 1-D wave equations for voltage and current are given by

$$\frac{\partial^2 V(z,t)}{\partial z^2} = \frac{1}{\gamma^2} \frac{\partial^2 V(z,t)}{\partial t^2} \quad \text{and} \quad (4.3)$$

$$\frac{\partial^2 I(z,t)}{\partial z^2} = \frac{1}{\gamma^2} \frac{\partial^2 I(z,t)}{\partial t^2}. \quad (4.4)$$

γ is a propagation constant of $\sqrt{(R_0 + j\omega L_0)(G_0 + j\omega C_0)}$. The solutions for the wave equation are denoted with left- and right-travelling waves for both parameters. Finally, the intrinsic impedance of the transmission line is obtained by the relation of

$$Z_0 = \sqrt{\frac{R_0 + j\omega L_0}{G_0 + j\omega C_0}} \quad (4.5)$$

The intrinsic impedance is important parameter to design electrical circuit because of losses or reflections at the interface caused by impedance mismatching.

A CPW is the most widely used structure of the transmission line in the superconducting circuit. The CPW consists of a center conductor with width w and ground planes on both sides separated by a gap g as shown in Fig. 4.4(b). The electrical parameters are determined by the width of center electrode, separation between the center conductor and the ground plane, and the relative dielectric constant. As discussed above, the intrinsic impedance should be matched with another resonator and the most common value for the RF circuits is 50 Ω . Therefore, it is necessary to design the transmission line having the same impedance.

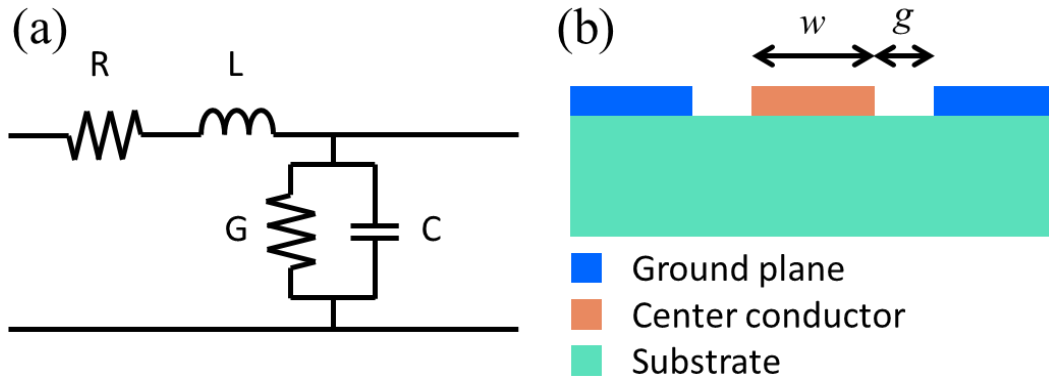


Figure 4.4 Schematic of transmission line. (a) Circuit diagram for infinitesimal length of transmission line and (b) the most common structure of transmission line, or CPW.

4.3.2 Interdigitated Capacitor

Interdigitated capacitor (IDC) has been used in sensing applications and evaluations of electrical properties [75]–[77]. The capacitance is measured between two comb- or finger-shaped electrodes. The capacitance depends on the dielectric properties (dielectric constant (ϵ_r) and thickness (h)), the electrode thickness (t), and the finger parameters such as number (N), length (l), and width (w). The interdigitated capacitance [78] is given by

$$C = (\epsilon_r + 1)l[(N - 3)A_1 + A_2] \quad (4.6)$$

where A_1 and A_2 are capacitance per unit length of fingers for interior and exterior cases. Both parameters are written by

$$A_1 = 4.409 \tanh[0.55(h/w)^{0.45}] \times 10^{-6} \text{ (pF/}\mu\text{m)} \text{ and} \quad (4.7)$$

$$A_2 = 9.920 \tanh[0.52(h/w)^{0.5}] \times 10^{-6} \text{ (pF/}\mu\text{m)}. \quad (4.8)$$

The IDC is also calculated by using a software package, COMSOL Multiphysics [79]. The structure of IDC used for the calculation is shown in Fig. 4.5. It is investigated that the capacitance is expressed as a function of finger number, length and width. The thickness of dielectric materials (Si and air) are set to be $100 \mu\text{m}$. As expressed in Eq. (4.6), there are linear relations in capacitance – number of fingers and capacitance – length of fingers. On the other hand, the capacitance has no finger width dependence because although it is related with A_1 and A_2 , their contributions are too low. The capacitances obtained from Eq. (4.6) is $\sim 10 \text{ fF}$ greater than the estimated values from the COMSOL. The calculated capacitances are used for designing coupling capacitor and lumped element in the resonator.

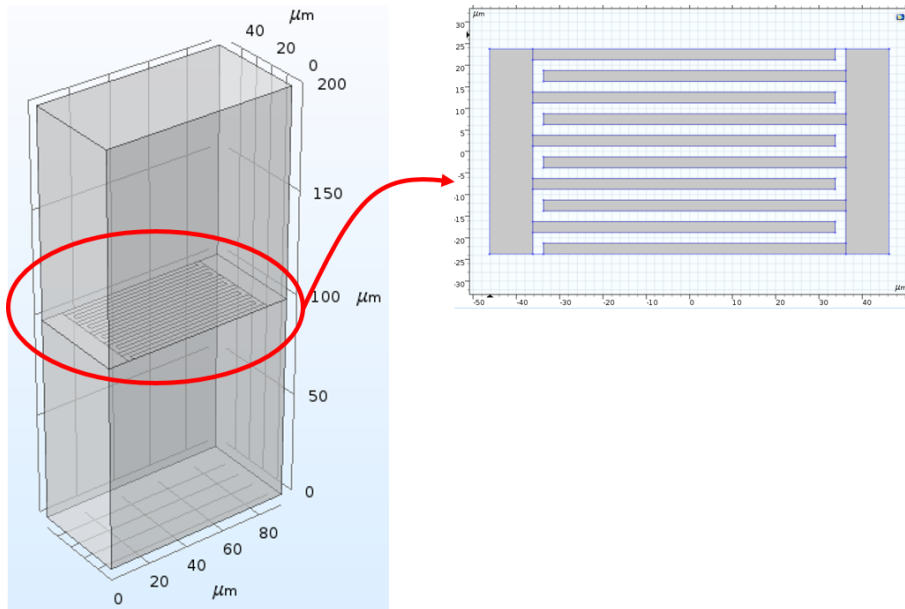


Figure 4.5 Design of interdigitated capacitor on COMSOL. The Si substrate and air are set to be $100 \mu\text{m}$.

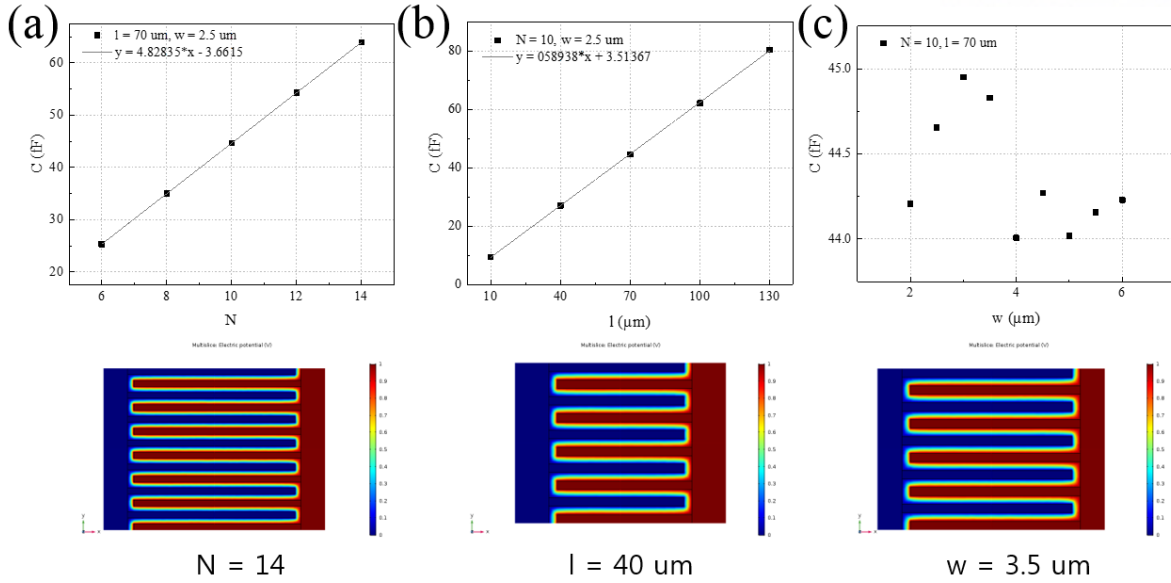


Figure 4.6 Simulation results of interdigitated capacitor. (a) Finger number (N) dependence with a constant length ($l = 70 \mu\text{m}$) and width ($w = 2.5 \mu\text{m}$). (b) Finger length (l) dependence with a constant number ($N = 10$) and with ($w = 2.5 \mu\text{m}$). (c) Finger width (w) dependence with a constant number ($N = 10$) and length ($l = 70 \mu\text{m}$).

4.3.3 Superconducting Resonator Measurement

Fig. 4.7 shows the superconducting resonator designed with a structure of quarter-wavelength resonator terminated with SQUID. The signal can be transmitted through the coupling capacitor. The resonant frequency is determined by the length of the quarter-wavelength resonator and affected by the inductance of SQUID. First, the Nb resonator was characterized by making the end grounded instead of using SQUID. The design of Fig. 4.7 was patterned by using photolithography and Nb deposited on the wafer was etched by using reactive ion etching (RIE). Then, the sample was put on the sample box and bonded with printed circuit board (PCB) by using Al wire as shown in Fig. 4.8(a). The packaged sample was placed at the dipping probe and cooled down at 4.2 K. The reflection in S parameters was measured and the resonant dip was observed as shown in Fig. 4.8(b). Phase and group delay are the other parameters to observe the resonant behavior. Finally, the sample terminated with the SQUID was prepared. The SQUIDs were patterned by using e-beam lithography and deposited as a structure of Al/AIO_x/Al by angle evaporation method. The packaged sample was mounted at the mixing chamber plate in the dilution refrigerator whose base temperature is ~ 7 mK because the critical temperature (T_C) of the aluminum is ~ 1.2 K. The magnetic flux was changed through the SQUID by applying DC bias and observed the resonant frequency tuning in the range of 5 \sim 6.7 GHz as shown in Fig. 4.9. The detailed experimental setup will be introduced in the following section.

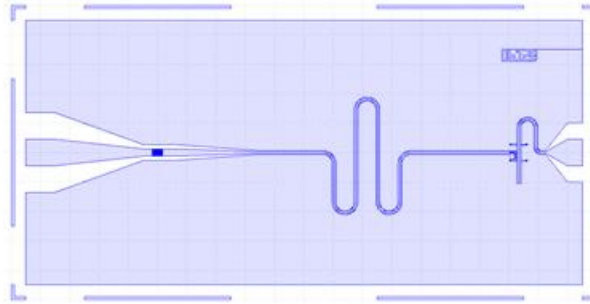


Figure 4.7 Design of superconducting resonator. One end of the resonator is open with the coupling capacitor and the other is grounded.

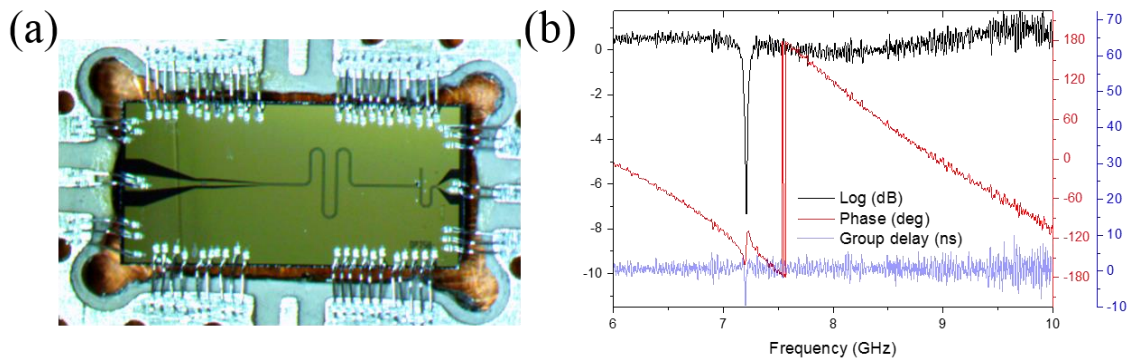


Figure 4.8 Measurement of Nb superconducting resonator. (a) The sample is mounted on the sample box and wire bonded with PCB. (b) Reflected signal is measured at 4.2 K by dipping in liquid He.

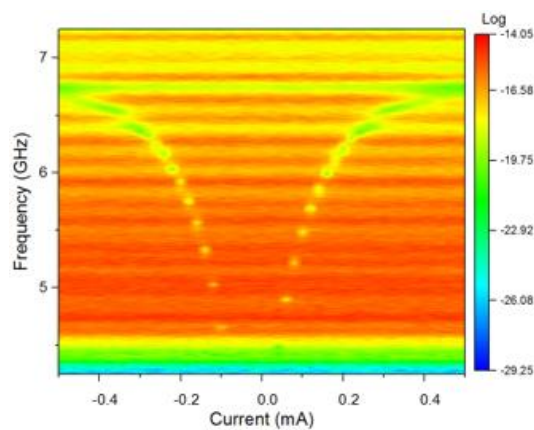


Figure 4.9 Resonant frequency tuning of the superconducting resonator. By varying the magnetic flux through the SQUID, the Josephson inductance and the corresponding resonant frequency can be tuned.

4.4 Setup for Experiments with Superconducting Circuit

Superconducting quantum circuits operate at <10 mK temperatures to reduce thermal excitations. Since the operational frequencies are in the GHz range, the corresponding temperature is $T = h\nu/k_B = 480$ mK for the frequency of 10 GHz. Compared to the fridge temperature of 7 mK, the temperature scale of 10 GHz is quite high. For example, the superconducting qubits can be in stable state. In addition to the temperature of sample, various microwave components including coaxial cables, circulators and isolators are possible sources to generate a loss. To thermalize the components, the components are anchored to each plate or stage. In this cryogenic setup, the quantum behaviors of electrical circuits such as parametric amplifiers and qubits are observed.

4.4.1 Cryogenic Setup

The superconducting circuit related experiments are conducted in Bluefors dilution refrigerators of which base temperature is ~ 7 mK. Fig. 4.10 depicts the experimental setup on the mixing chamber which is at the lowest temperature of the fridge. Basically, three ports of RF input, RF output, and DC line are used. To operate the JPA, another microwave path for pump tone is needed, which is combined with the DC bias through bias tee as shown in Fig. 4.10(a). The reflected signal from the JPA is sent through two successive isolators giving > 60 dB isolation. When the quantum limited amplification is observed with the superconducting qubit by using JPA, the qubit is located before the JPA. An additional isolator is added between the qubit and JPA to prevent the signal reflected back. Most of qubit measurements are conducted under the basic setup with three ports as shown in Fig. 4.10(b). A DC bias is used only when the qubit having tunable transition frequency is used.

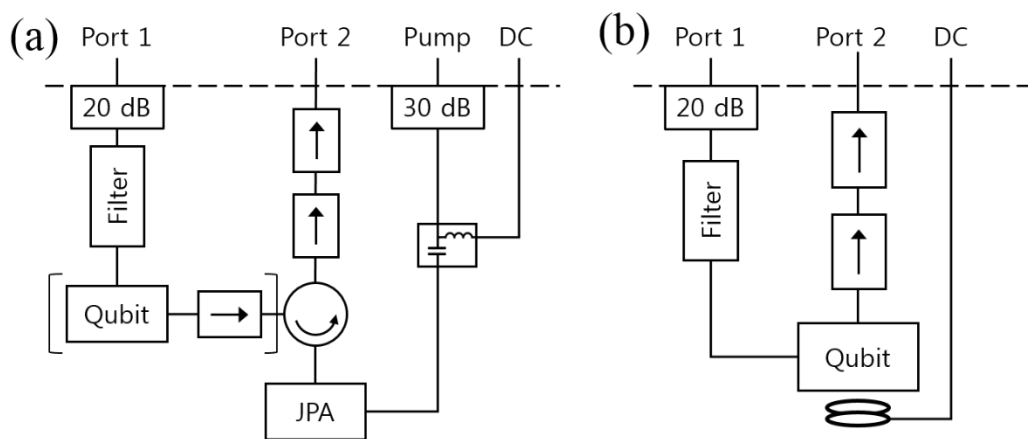


Figure 4.10 Experimental setup on mixing chamber plate for characterization of the samples. (a) When the JPA is used to amplify the qubit signal, the qubit and an isolator are added between filter and circulator. (b) The qubit is measured in transmission mode and when tunable qubit is used, a DC bias line is added.

4.4.2 Homodyne Measurement

Homodyne measurements provide the phase and magnitude of information by frequency down-conversion using mixer. A mixer is used to mix a RF signal with local oscillator (LO) by frequency conversion. When two microwave signals are mixed, two output signals are produced with the sum and difference of the input signal (ω_S) and LO (ω_{LO}) frequencies,

$$\begin{aligned} & A \cos(\omega_S t + \phi) \times \cos(\omega_{LO} t) \\ &= \frac{A}{2} [\cos((\omega_S - \omega_{LO})t + \phi) + \cos((\omega_S + \omega_{LO})t + \phi)]. \end{aligned} \quad (4.9)$$

When only considered with the down-conversion process, the second term can be neglected by using a low pass filter. Here, the process can be divided into two cases depending on the magnitude of difference in two frequencies. One is called as ‘homodyne’ method in case $\omega_S = \omega_{LO}$, or $\omega_S - \omega_{LO} = 0$ and the other as ‘heterodyne’ method in case $\omega_S \neq \omega_{LO}$. In this case, the homodyne method is used for the experiments. The output signal is detected by an oscilloscope. When the phase of LO is changed by using manual phase shifter, two output signals can be detected

$$I(t) = A(t) \cos(\phi) \quad \text{and} \quad Q(t) = A(t) \sin(\phi). \quad (4.10)$$

They are phase-shifted by 90° , giving the information of quadratures, X_1 for I and X_2 for Q. In homodyne detection with the phase sensitivity of the JPA, each quadrature operator or a linear combination of two quadratures can be observed. On the other hand, heterodyne method with phase insensitivity, both quadratures can be measured but, cannot be determined simultaneously with accuracy due to the commutation relation of $[X_1, X_2] = i/2$. The details of the homodyne setup to detect the squeezed state by using JPA are described in section 6.3.1.

Chapter 5 . Metal/Semiconductor Junction with Various Interfacial Layers and Its Application in Tunable Capacitor

As mentioned in chapter 3, it is important to understand electron transport mechanism in semiconductor industry. The Schottky junction has frequently been used and the SBH is a key parameter in the electron transport to affect device properties. Basically, the SBH is defined by the difference between the Fermi level of metal and the electron affinity of semiconductor. However, the Schottky junction sometimes shows different transport behaviors across the junction depending on used materials and interface states. In this chapter, the electrical properties of the Schottky junction is discussed depending on different interface states on the substrate, especially 4H-SiC. In the later part of the chapter, it is showed that metal/oxide/floating-Schottky junction has the capacitive memory effect working based on the variation of depletion of the Schottky junction.

5.1 Modulation of Metal/4H-SiC Schottky Barrier by Inserting Thin Al₂O₃ Layer

SiC has superior properties including high breakdown voltage and high thermal conductivity [67], [80]. Therefore, it has been researched as a wide band-gap semiconductor in the area of high-power device. Besides its electrical properties, it shows different material properties depending on the polytypes where the sequence of Si-C bilayer stacking [62], [81]–[83] makes a difference. A representative type of polytype-dependent material properties is spontaneous polarization (SP). The SP is shown only for the polytypes having hexagonal turn in the stacking sequence due to the broken balance in the tetrahedral sp³ bonds of Si and C atoms [69], [84], [85]. On the other hand, the polytype having a cubic symmetry (e.g. 3C-SiC) does not show the SP. Here, the SP of 4H-SiC effects on the Schottky barrier located at the metal/4H-SiC junction is studied by inserting a thin spacer layer and making a thin distance between the metal and 4H-SiC substrate [86]. It is expected that the negative charges of the SP induced on the 4H-SiC causes the increases in the SBH [87], [88]. Both Au/Ni/4H-SiC and Au/Ni/Al₂O₃/4H-SiC junctions are compared to evaluate this suggestion by measuring the electrical properties with I-V and C-V methods.

5.1.1 Sample Fabrication

A n-type 4H-SiC wafer (Cree Inc.) was prepared to fabricate the Au/Ni/4H-SiC and Au/Ni/Al₂O₃/4H-SiC junctions. The wafer consists of a 0.5 μm-thick buffer layer and a 17.8 μm-thick epilayer. The buffer layer with $1 \times 10^{18} \text{ cm}^{-3}$ doping and epilayer with doping concentration of $2 \times 10^{15} \text{ cm}^{-3}$ were grown on a n-type 4H-SiC having 8.06° miscut in order. Note that both layers are n-type doped. The two pieces were cut from the 4H-SiC wafer and cleaned by using trichloroethylene, acetone, and methanol. Then, a native oxide grown on the pieces was removed by dipping them into HF (49 %) solution and rinsing them with methanol. After cleaning, one of the prepared samples was used to deposit a 3 nm thick Al₂O₃ film by using atomic layer deposition (ALD). The growth of Al₂O₃ thin film was conducted with a 50 sccm N₂ gas flowing at 200 °C, and trimethylaluminum (TMA) and water (H₂O) were used as precursors. One cycle has four stages; a 0.2 s TMA pulse, a 10 s TMA purge, a 0.2 s H₂O pulse, and a 10 s H₂O purge. With this condition, the Al₂O₃ film is grown in a rate of 1.2 Å per one cycle. Then, the Au/Ni with thickness of 200 nm/500 nm were deposited as top electrodes and patterned through a circular shadow mask on both samples by using e-beam evaporator.

Fig. 5.1 shows the cross-sectional high-resolution transmission electron microscopy (HRTEM) image of both junctions. For the Au/Ni/Al₂O₃/4H-SiC junction, the oxide thickness was measured to be ~4.3 nm which is thicker than expected. It is revealed that the observed oxide layer in the image is composed of the deposited Al₂O₃ layer (~3.3 nm) and the natively grown SiO₂ layer (~1 nm) [89]. It is possible that the SiO₂ is remained during the fabrication process even though the samples were cleaned with HF solution beforehand. Also, the native oxide could be considered in the Au/Ni/4H-SiC junction.

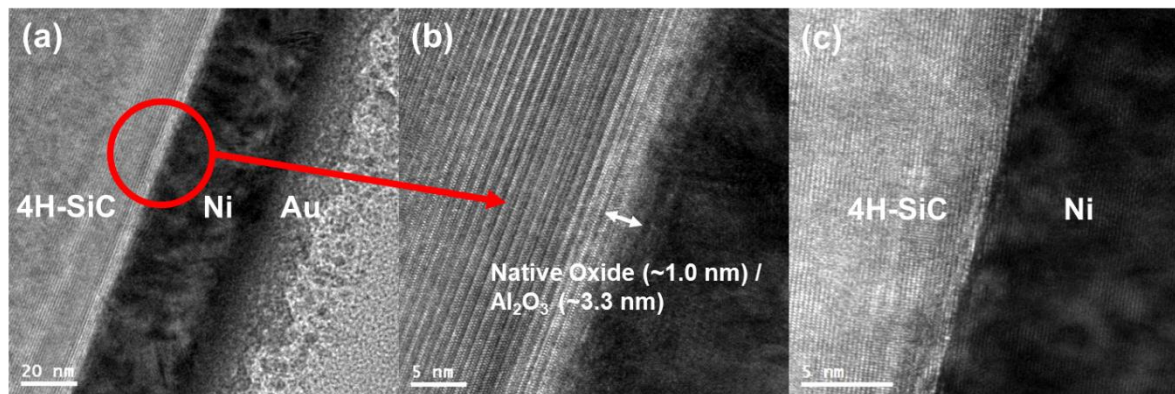


Figure 5.1 (a) Cross-sectional HRTEM image of the Au/Ni/Al₂O₃/4H-SiC junction and (b) its magnified image. (c) Cross-sectional HRTEM image of the Au/Ni/4H-SiC junction. The crystal plane of the substrate is (1-100).

5.1.2 I-V Measurement

The current-voltage curves of both junctions are shown in Fig. 5.2(a) and both junctions work as a usual rectifying Schottky junction. The Schottky behavior is observed in the Au/Ni/Al₂O₃/4H-SiC junction although it has the Al₂O₃ insulating spacer layer because the spacer layer is leaky itself, related with direct tunneling and trap-assisted current conduction in the layer. In the I-V curve of the Au/Ni/Al₂O₃/4H-SiC junction, the larger junction resistance is observed above the threshold region compared to the Au/Ni/4H-SiC junction. This means that the spacer layer can be resistive while it is transparent in the electron transport, and it gives the additional resistance. Especially, higher turn-on voltage is observed in the I-V curve of the Au/Ni/Al₂O₃/4H-SiC junction than that of Au/Ni/4H-SiC junction. By using Eq. 3.1 of the thermionic emission theory and fitting the measured I-V curves as shown in Fig. 5.2(a), the Schottky barrier height (SBH) is extracted as 1.51 ± 0.04 eV for Au/Ni/4H-SiC junction and 2.06 ± 0.13 eV for Au/Ni/Al₂O₃/4H-SiC junction, respectively.

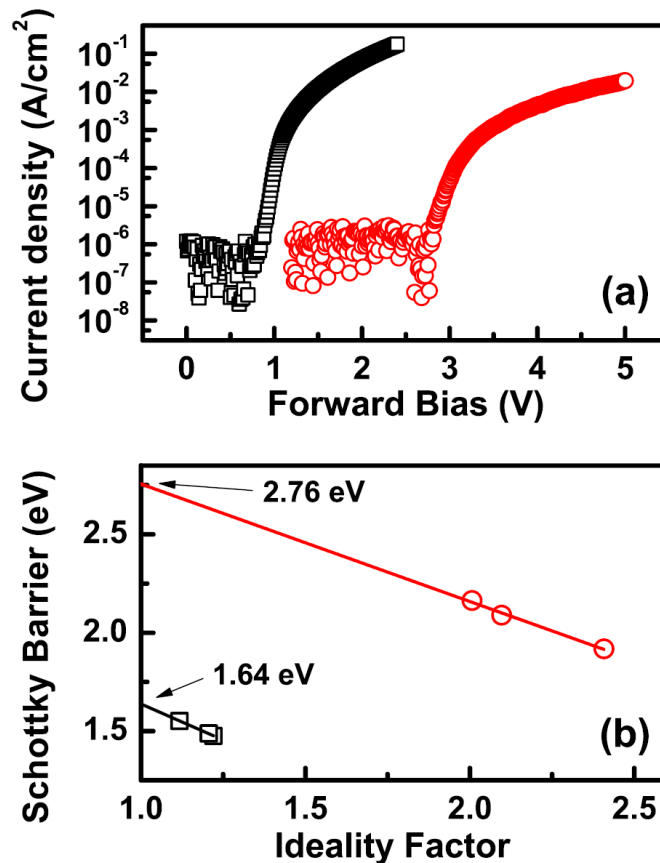


Figure 5.2 (a) Current density as a function of forward bias for Au/Ni/4H-SiC (black square) and Au/Ni/Al₂O₃/4H-SiC (red circle) junctions in semi-log scale. (b) The linear relation between ideality factor and SBH. The intercepted SBH with $n = 1$ means the barrier height except the portion of low-barrier patches.

The ideality factor (n), implying the deviation from the ideal Schottky junction, is another parameter to be noted in the I-V measurement. It is estimated to be 1.18 ± 0.06 for the Au/Ni/4H-SiC junction, which is close to the ideal Schottky junction and 2.17 ± 0.21 for Au/Ni/Al₂O₃/4H-SiC junction showing much larger than unity. The reason for non-ideality of the Au/Ni/Al₂O₃/4H-SiC junction is that Al₂O₃ film is not evenly deposited and then it has non-uniform thickness, making some local areas with lower SBs than the surroundings. Several researchers have demonstrated that these even very small low-barrier regions can affect the I-V curves [90]–[92]. In other words, the local low-barrier regions cause the increase in the ideality factor of the I-V curve and the SB to be measured even lower than average SB of the surrounding area [91]–[94]. As mentioned in R. T. Tung [95], the energy band profile of the low-barrier regions is pinched off because of the surroundings having high barrier. If there is small enough low-barrier region, the pinch-off can be enhanced to nearly close the low-barrier region. Then, the low-barrier regions can be neglected in terms of the carrier transport, and the Schottky junction behaves like an ideal junction. However, in this case, the ideality factor of Au/Ni/Al₂O₃/4H-SiC junction is large, and it indicates that some low-barrier regions are not negligible in the junction.

Table 5.1 summarizes the electrical parameters of the Au/Ni/4H-SiC and Au/Ni/Al₂O₃/4H-SiC junctions extracted from the I-V measurement curves. As shown in Fig. 5.2(b), the Schottky barriers and the ideality factors obtained from the I-V curves are linearly related to each other. The Schottky barrier without the effect of the low-barrier regions are estimated by finding the intercept of the linearly fitted line with $n = 1.0$. The extracted SBH of the Au/Ni/4H-SiC and Au/Ni/Al₂O₃/4H-SiC junctions are ~ 1.64 eV and ~ 2.76 eV, respectively.

Table 5.1 Summary of electronic properties for Au/Ni/4H-SiC and Au/Ni/Al₂O₃/4H-SiC junctions.

	J_{0a}	Ideality factor	ϕ_B (IV) ^b	ϕ_B (CV) ^c
Au/Ni/4H-SiC	$(1.06 \pm 0.91) \times 10^{-18}$	1.18 ± 0.06	1.51 ± 0.04	1.97 ± 0.027
Au/Ni/Al ₂ O ₃ /4H-SiC	$(2.26 \pm 3.91) \times 10^{-26}$	2.17 ± 0.21	2.06 ± 0.13	3.21 ± 0.082

^a J_0 (A/cm²) is the reverse saturation current density.

^{b,c} ϕ_B is the barrier obtained from the I-V and C-V curves (eV).

5.1.3 C-V Measurement

To get the Schottky barriers on the prevailing areas of the Au/Ni/4H-SiC and Au/Ni/Al₂O₃/4H-SiC junctions, capacitance-voltage (C-V) measurement technique is used. The bias-dependent differential capacitance of $C = dQ/dV$ is measured by applying a reverse bias (V_R) with an AC voltage of 50 mV amplitude and 1MHz frequency and the reverse bias is applied in the range from 0 V to 2.2 V. The C-V curves of the Au/Ni/4H-SiC and Au/Ni/Al₂O₃/4H-SiC junctions can be seen in Fig. 5.3(a). The measured capacitance data are replotted as $1/C^2$ vs. V_R with the linear fitting lines. By using the abrupt depletion approximation referred to the chapter 2, the doping concentration (N_D) and the SBH could be obtained. The doping concentrations for the Au/Ni/4H-SiC and the Au/Ni/Al₂O₃/4H-SiC junctions are extracted to be $(3.34 \pm 0.23) \times 10^{15} \text{ cm}^{-3}$ and $(2.90 \pm 0.10) \times 10^{15} \text{ cm}^{-3}$, respectively. These values of both junctions are close to the provided value ($2.00 \times 10^{15} \text{ cm}^{-3}$) by the vendor. The SBH calculated from the procedure are $1.97 \pm 0.027 \text{ eV}$ for the Au/Ni/4H-SiC and $3.21 \pm 0.082 \text{ eV}$ for the Au/Ni/Al₂O₃/4H-SiC junctions, as shown in Table 5.1.

Even when the influence of the low-barrier regions is neglected, the Schottky barrier obtained from the C-V measurement is larger than that from the I-V measurement. Although the image force lowering is considered, the estimated values to be $\sim 25 \text{ meV}$ for the Au/Ni/4H-SiC and $\sim 29 \text{ meV}$ for the Au/Ni/Al₂O₃/4H-SiC junctions are insufficient to explain the discrepancies between the Schottky barriers obtained from the I-V and C-V measurements. It can be mostly attributable to the capacitive component of ohmic contact in the substrate and the stray capacitances in the measurement system. Due to the additional capacitive components, the capacitance of the Schottky junction can be measured smaller than the actual value. The smaller capacitance induces over-estimated built-in potential which is the V_R -intercept of the linearly fitted line in the $1/C^2$ vs. V_R plot and also the higher Schottky barrier. Since it is expected that the added capacitive components are quite similar for both junctions, their influences are negligible for the increase of the Schottky barrier with the inserted Al₂O₃ spacer layer. The Schottky barrier of the Au/Ni/Al₂O₃/4H-SiC junction measured from the C-V method is estimated much higher with the amount of $\sim 1.24 \text{ eV}$ than that of the Au/Ni/4H-SiC junction, like the I-V measurement. Just as a note, when the influences of the low-barrier regions are excluded, the difference between two junctions obtained from the I-V measurement is $\sim 1.12 \text{ eV}$.

It is noticeable that the C-V measurements are insensitive to the low-barrier regions. Considering a native oxide layer ($< 1 \text{ nm}$) for both junctions and the spacer oxide layer ($\sim 3 \text{ nm}$) for Au/Ni/Al₂O₃/4H-SiC junction, the total oxide layer of 4.3 nm thickness is much thinner than the width of depletion region in the 4H-SiC ($\sim 900 \text{ nm}$ for $N_D = 2.00 \times 10^{15} \text{ cm}^{-3}$). Therefore, the oxide capacitance (C_{ox}) is > 200 times larger than depletion capacitance (C_D) by the reciprocal relation with the dielectric thickness. Then, the effective capacitance (C_{eff}) is mainly attributed from the depletion region capacitance because the capacitors of the oxide layer and the depletion region are series connected as

$$C_{eff} = \frac{C_D}{1 + C_D / C_{ox}} \sim C_D. \quad (5.1)$$

By this calculation, it can be considered that the Schottky barrier extracted from the C-V measurements is almost entirely corresponding result of the depletion region without the considerations of the small low-barrier regions and the capacitive components of the spacer layer in the surroundings with high barrier.

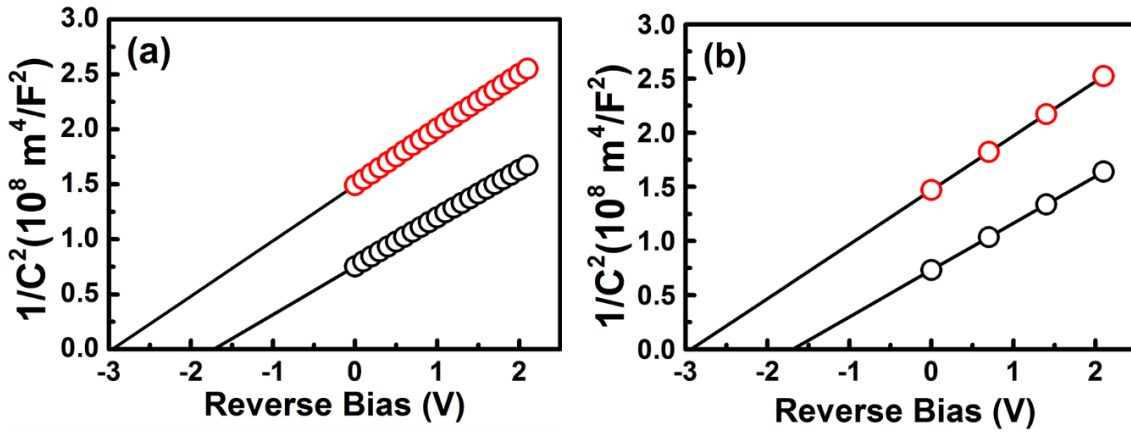


Figure 5.3 The C-V characteristics in (a) measured and (b) calculated $1/C^2$ vs. V_R plots. The modeling with finite element method is conducted by using commercial tool, FlexPDE.

5.1.4 Finite Element Electrostatic Modeling

It is demonstrated that the Schottky barrier is increased when the Al_2O_3 spacer layer is inserted in the Schottky junction through the I-V and C-V measurements. The increase in Schottky barrier is thought to be mainly due to negative charges located at the 4H-SiC surface generated by the SP of the 4H-SiC. Fig. 5.4 shows the formation of a dipole layer by forming negative SP charges and the same-amount induced positive charges on the 4H-SiC surface and the metal electrode, respectively. As a result, linear increase in the electrostatic potential energy from the metal surface to the 4H-SiC surface is induced. As the electrostatic potential energy on the 4H-SiC surface increases, its conduction band energy minimum is accordingly raised. The increase of the electrostatic potential energy occurs across a thin native oxide (SiO_2) for the Au/Ni/4H-SiC junction (Fig. 5.4(a)). On the other hand, there is an additional increase of electrostatic potential energy due to the existence of the Al_2O_3 spacer layer in the Au/Ni/ Al_2O_3 /4H-SiC junction, inducing the increase of Schottky barrier compared to the Au/Ni/4H-SiC junction, as shown in Fig. 5.4(b).

The SB increase is estimated due to the dipole layer formation by the SP charge by calculating the C-V curves and use FlexPDE [96] which is one of finite element electrostatic modeling tool. The

procedure is followed with one used by K. -B. Park *et al.* [97] and the electrostatic potential energy in the dielectric materials (e.g. oxide layer and substrate) is given by

$$\varphi_{tot} = \varphi(x, y, z) + (\varphi_m - \chi), \quad (5.2)$$

where $\varphi(x, y, z)$ is the electrostatic potential energy at (x, y, z) , φ_m is the work function of metal (Ni), and χ is the electron affinity of the dielectric materials (Al_2O_3 , SiO_2 , and 4H-SiC). The potential energy $\varphi(x, y, z)$ in Eq. (5.2) can be determined by solving the Poisson's equation

$$\nabla^2 \left[-\frac{\varphi}{q} \right] = -\frac{\rho(x, y, z)}{\epsilon_0 \epsilon_r}, \quad (5.3)$$

where $\rho(x, y, z)$ is the net charge density, ϵ_r the relative dielectric constant of Al_2O_3 , SiO_2 , or 4H-SiC. It is assumed that the net charge density in the oxide layers are set to be zero and in the 4H-SiC is given as

$$\rho(x, y, z) = q[N_D - n_c(x, y, z)]. \quad (5.4)$$

The density of free electron, n_c is

$$n_c = N_c \exp[(E_{F,S} - \varphi_{tot}) / k_B T], \quad (5.5)$$

where N_c is the effective electron density of states ($1.83 \times 10^{19} \text{ cm}^{-3}$ for 4H-SiC), and $E_{F,S} = -qV_R$ is the Fermi level energy of the semiconductor when a reverse bias is applied. Here the extracted donor concentration from the C-V measurement is used and the negative SP charge on the 4H-SiC surface is set to be the boundary condition at the interface of oxide and 4H-SiC. Table 5.2 summarizes the material parameters used in the calculation. As the reverse bias varies with a small amount ΔV_R , the charge Q_m on the metal electrode is induced. Then, the change of charge is quantified, and the differential capacitance is obtained, giving

$$C = \Delta Q_m / \Delta V_R, \quad (5.6)$$

where $Q_m = Q_m(V_R) - Q_m(V_R + \Delta V_R)$. The amount of SP of 4H-SiC surface is found to be $3.00 \times 10^{-2} \text{ C/m}^2$ by repeating the calculation with different SP of 4H-SiC and getting the best-fitted C-V curve to the measured one as shown in Fig. 5.4(b). The estimated SP of 4H-SiC is a bit larger but very close to the previous theoretically-predicted [69], [81], [84] or experimentally-found values [98], [99] in the range of $(1.10 - 2.16) \times 10^{-2} \text{ C/m}^2$.

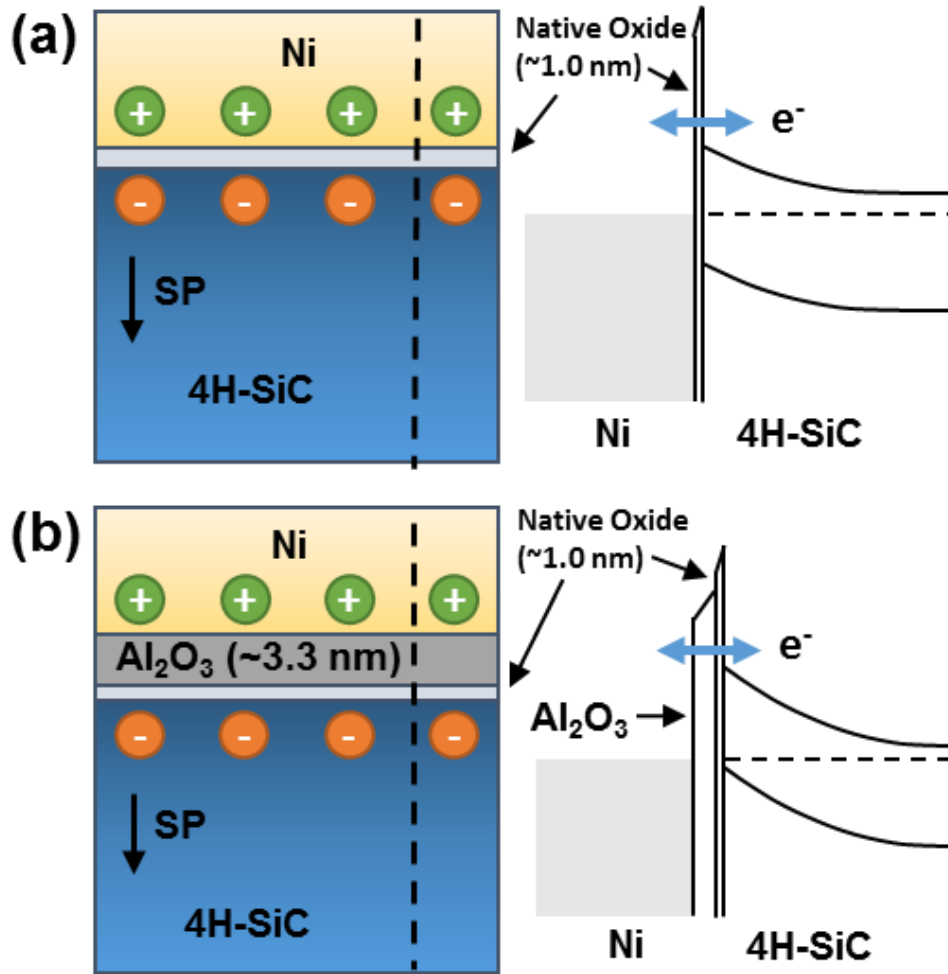


Figure 5.4 Device layer schematic and energy band diagram of (a) Au/Ni/4H-SiC and (b) Au/Ni/Al₂O₃/4H-SiC junctions. The energy band profiles at the right side are indicated along the dashed line of device schematic.

Table 5.2 The electrical characteristics used for finite element electrostatic modeling with work function, electron affinity, and dielectric constant.

$\phi_m(Ni)$	χ_{4H-SiC}	χ_{SiO_2}	$\chi_{Al_2O_3}$	ϵ_{4H-SiC}	ϵ_{SiO_2}	$\epsilon_{Al_2O_3}$
5.10 eV	4.05 eV	0.9 eV	1.35 eV	9.7	3.9	9.0

5.1.5 Conclusion

It has showed that when a thin Al_2O_3 spacer layer is inserted in the Au/Ni/4H-SiC junction, the Au/Ni/ Al_2O_3 /4H-SiC junction behaves as a normal rectifying Schottky diode, having quite high threshold voltage. Due to the direct tunneling or trap-assisted conduction across the thin Al_2O_3 layer, the junction is considered to have the rectifying behaviors. Also, the Au/Ni/ Al_2O_3 /4H-SiC junction have the significant higher threshold voltage compared to Au/Ni/4H-SiC junction because of electrostatic potential energy jump for electron. This jump occurs across the dipole layer consisting of the negative charges by SP bound on the 4H-SiC substrate and the positive charges induced on the metal electrode. The measured C-V curves are reproduced by using the finite element method and assuming the proper value of the SP of 4H-SiC. It is found that the assumed value of the SP is quite close to the previously reported values. As a result, the SP of 4H-SiC can modulate the Schottky barrier of the metal/4H-SiC efficiently by the insertion of thin interfacial layers.

5.2 Effect of Electric Dipole Formed at Au/Graphene Interface on Au/Graphene/4H-SiC Junction

Graphene (Gr) has been widely used in the device applications and it becomes essential to form a contact with metal electrodes [100]–[102]. The following researches of metal/graphene have been studied and the doping graphene [103] due to the contact with metals is interesting. An electric dipole formed at an interface of metal/graphene causes the doping on graphene showing the dependence on the work function of metal and adsorption to the graphene. Also, it is described with an extra charge caused by an electric dipole between graphene and metal. These phenomena on the metal/graphene interface are demonstrated by forming Au/Gr/4H-SiC Schottky junction. The 4H-SiC is a kind of substrate showing weak Fermi level pinning [104], whereas the most used Si and GaAs are the substrates having strong Fermi level pinning [105], [106]. The Fermi level pinning interrupts an observation of influence of the dipole charges on the junction properties and thus the 4H-SiC is appropriate candidate. The Au is used as top electrode because it is one of metals having weak adsorption with graphene and forming electric dipole and it also forms the Schottky junction of large barrier height due to the work function of 5.1 ~ 5.4 eV and inactive reaction with the substrate. The formation of electric dipole is confirmed by the change in the SBH with I-V, C-V, and IPE measurements. Then, the calculation by using finite element method is conducted to support the dipole formation.

5.2.1 Graphene

Graphene is composed of a single layer of carbon atoms in honeycomb structure where the carbon atoms are bound by orbital hybridization as shown in Fig. 5.5(a). A. Geim and K. Novoselov discovered graphene, new two-dimensional material experimentally in 2004 [107] and they were awarded the Nobel Prize in Physics in 2010 for their works on graphene. The appearance of novel material has attracted much attention because of superior properties of high thermal conductivity, high electron mobility, and so on. The linear energy dispersion relation is one of unique properties of graphene and can be understood by using tight-binding approximation. It was first proven by P. R. Wallace [108] and is given as

$$E_{\pm} = \hbar v_f |k| \tag{5.7}$$

where E_{\pm} is the conduction band or valence band, v_f the Fermi velocity ($\sim 10^6$ m/s), and k the wave vector. Based on this relation, there are crossing points of the conduction and valence bands as shown in Fig. 5.5(b). They are called as ‘Dirac points’ and these energy band structure as ‘Dirac cones’. Especially, for the intrinsic graphene can be either semi-metal or zero-gap semiconductor due to its gapless band structure, giving outstanding electrical properties ever.

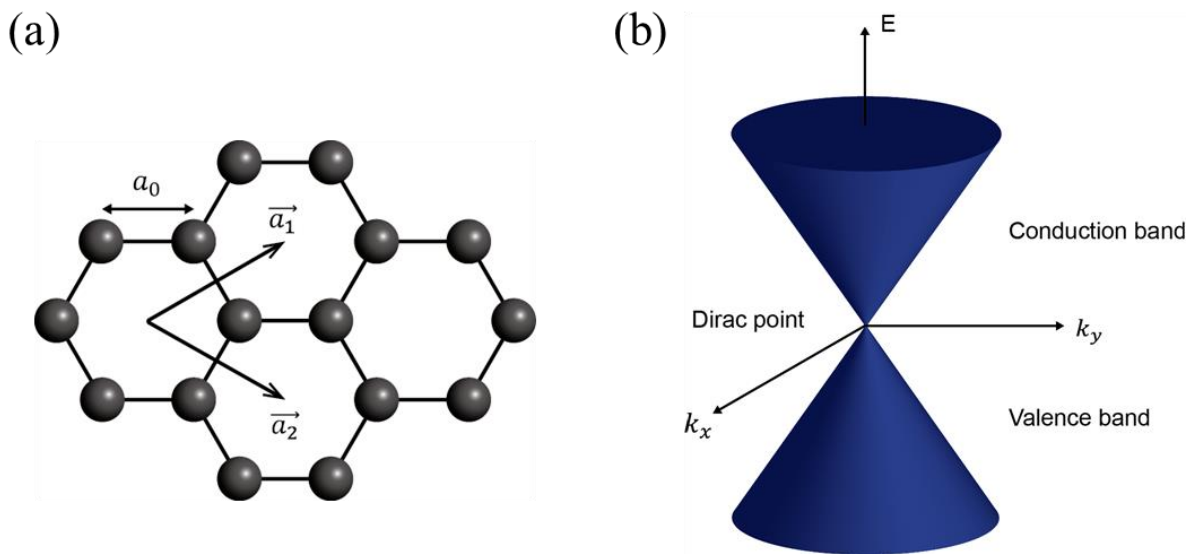


Figure 5.5 (a) Honeycomb lattice structure of graphene. a_1 and a_2 are the lattice vectors. (b) Dirac-cone shaped energy band structure. The upper conduction band and lower valence band intersect at a point, called Dirac point.

5.2.2 Sample Fabrication

The 4H-SiC wafer used in this work was double-side polished and comprised of 360 μm -thick substrate and its doping concentration of $N_D = 5 \times 10^{18} \text{ cm}^{-3}$ and 25 μm -thick epilayer and its doping concentration of $N_D = 1 \times 10^{15} \text{ cm}^{-3}$. Two 1 cm \times 1 cm samples were used for the comparison and cleaned with 49 % HF solution for 1 min to etch native oxide (SiO_2). The C-face of the SiC was used to make an Ohmic contact due to the high doping concentration and the Si-face to form a Schottky junction. Prior to the formation of Ohmic contact and Schottky junction, a protective layer is deposited with SiO_2 layer of 100 nm thickness on the Si-face by using plasma-enhanced chemical vapor deposition (PECVD). The samples were dipped into a diluted 49 % HF and DI water solution (1:10) to eliminate the native oxide grown slightly during the deposition of the protective layer. Then, Ni film with 100 nm thickness was deposited on the C-face SiC by using e-beam evaporator and the annealing process was followed at 1000 $^\circ\text{C}$ for 90 s without any gas flow. The sample was again dipped in 49 % HF solution for 1 min to remove the remained native oxide before the Schottky junction formation. To compare the effect of graphene/metal contact, graphene was transferred on one sample by using dry transfer method [S19]. The top electrode of 50 nm-thick-Au was deposited on both samples by using e-beam evaporator and was patterned with 500 μm diameter-circles through metal shadow mask. The neighboring junctions on Au/Gr/4H-SiC were isolated by removing graphene with O_2 plasma etching.

5.2.3 I-V Measurement

Both junctions exhibit the rectifying current-voltage (I-V) characteristics as in Fig. 5.6(a) and their breakdown reverse voltages are still high as usual SiC devices. However, the threshold voltage, which is related to the SBH, decreases in the junction with the graphene, as better seen in the semi-logarithmic plot in Fig. 5.6(b). From the curve fitting of the semi-logarithmic plot, the obtained SBHs for the Au/4H-SiC and Au/Gr/4H-SiC junctions were $1.89 \pm 0.02 \text{ eV}$ and $1.05 \pm 0.02 \text{ eV}$, respectively. In case of the Au/4H-SiC junction, the SBH is similar to the reported values [109], [110]. The ideality factor increases from 1.05 ± 0.01 to 2.11 ± 0.09 when the graphene is located between the metal and semiconductor. The non-ideal behavior of the Au/Gr/4H-SiC is contributed significantly by uneven graphene transfer. The defects such as ripples, and ridges causes spatial inhomogeneous and alter locally the electrical properties of the junction [111], [112]. It might be several nm-height and its effect on the charge transfer will be explained later. Also, it is noted that the current flows less in the Au/Gr/4H-SiC junction that it becomes leaky although the energy barrier is to be low.

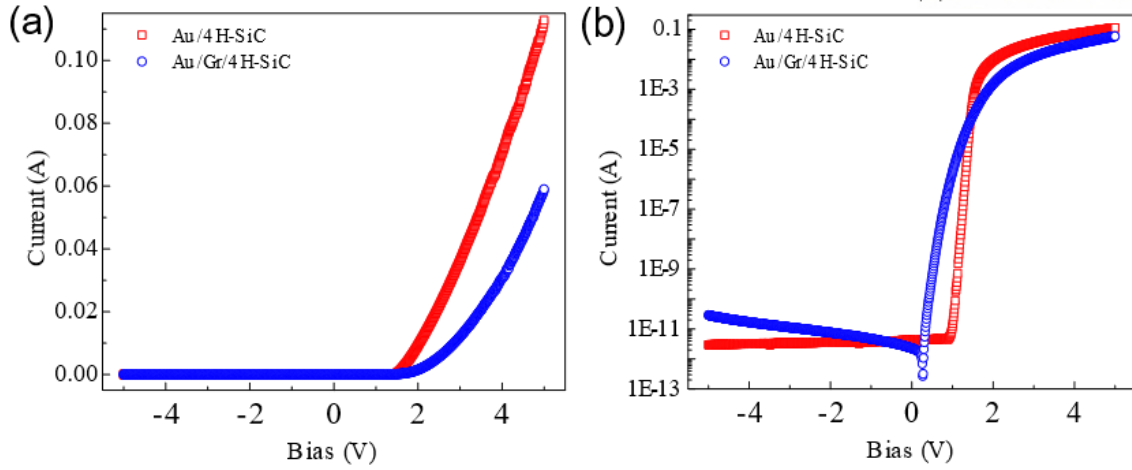


Figure 5.6 I-V characteristics. (a) Current as a function of forward bias for Au/4H-SiC (red square) and Au/Gr/4H-SiC (blue circle) junctions in linear scale and (b) in log-scale.

5.2.4 C-V Measurement

The SBH is also extracted from the capacitance-voltage (C-V) measurement. Agilent E4980A LCR meter is used to measure the capacitance and the reverse bias is applied from 0 V to 2V with an alternating AC voltage having the frequency of 100 kHz and the magnitude of 50 mV. The bias-dependent differential capacitance ($C = dQ/dV$) curves are shown in Fig. 5.7. The curves are analyzed according to the abrupt depletion approximation. Two electronic parameters in the $1/C^2$ vs. V curve can be obtained, the doping concentration from the slope and the built-in potential (V_{bi}) from the extrapolated voltage. The V_{bi} describes the amount of band bending in the bulk semiconductor and is defined as $V_{bi} = \phi / q - \zeta - k_B T / q$. Using this relation, the SBHs are extracted with 1.98 ± 0.01 eV for the Au/4H-SiC junction and 1.38 ± 0.02 eV for the Au/Gr/4H-SiC junction. As consistent with the I-V results, the SBH is reduced when the graphene is located in the Au/4H-SiC junction. The SBH obtained from the C-V measurement is higher than that from the I-V measurement because the low SBH regions in the junction are not considered and the electrical properties over whole area of the junction are treated in the C-V characteristics. The image force lowering (IFL) is the other reason to give lower energy barrier in the I-V characteristics.

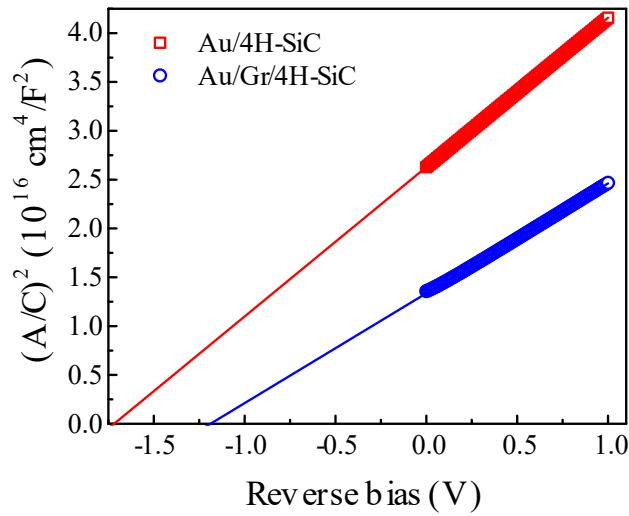


Figure 5.7 C-V characteristic in measured $1/C^2$ vs. V_R plots for Au/4H-SiC (red square) and Au/Gr/4H-SiC (blue circle) junctions.

5.2.5 IPE Measurement

The last method used to estimate the SBH is internal photoemission (IPE). The SBH obtained from the IPE method gives relatively exact value compared to other methods since the electrons surmounting the energy barrier are only detected and the measured photocurrent is dominated by prevailing region of the junction [113]. Referring the results of the I-V and C-V measurements, the IPE measurement range is set as 1.55 ~ 1.70 eV for the Au/4H-SiC junction and 1.1 ~ 1.8 eV for the Au/Gr/4H-SiC junction. It is because depending on the energy, different filter and fiber were used to measure the photocurrent. When the electrons start to move over the SBH, the current abruptly increase. Then, the SBH can be extracted from the extrapolated photon energy in the first linear region after the threshold. The IPE results of the junctions are shown in Fig. 5.8. The SBH of the Au/4H-SiC junction is extracted with 1.82 ± 0.01 eV and that of the Au/Gr/4H-SiC junction with 1.24 ± 0.00 eV. The result obtained from the IPE is in agreement with other measurement results that the SBH decreases when the graphene is located between the Au/4H-SiC junction. The SBHs and related parameters extracted from each measurement are listed in Table 5.3.

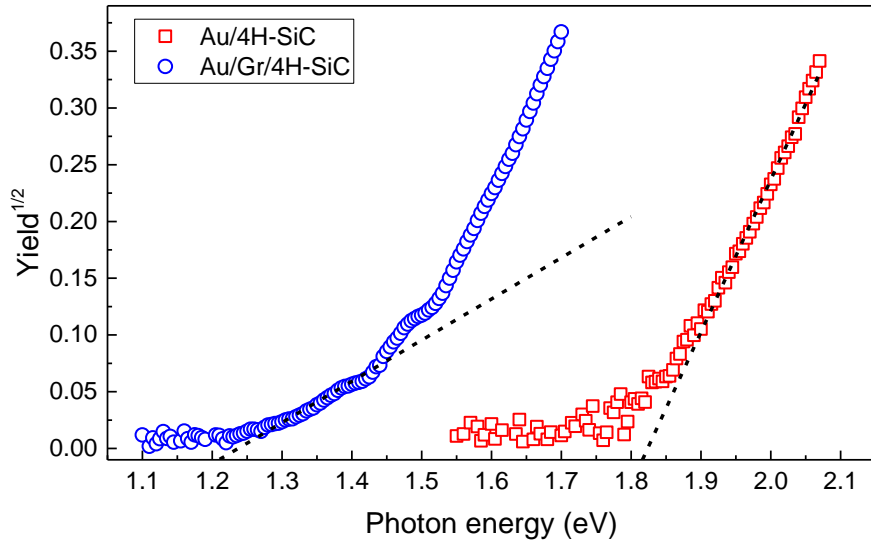


Figure 5.8 IPE Characteristic for Au/4H-SiC (red square) and Au/Gr/4H-SiC (blue circle) junctions.

Table 5.3 Summary of data for Au/4H-SiC and Au/Gr/4H-SiC.

	n	$\phi_{B,I-V}$ (eV)	N_D (cm ⁻³)	$\phi_{B,C-V}$ (eV)	$\phi_{B,IPE}$ (eV)
Au/4H-SiC	1.05±0.01	1.89±0.02	(0.73±0.01)×10 ¹⁵	1.98±0.01	1.82±0.01
Au/Gr/4H-SiC	2.11±0.09	1.05±0.02	(1.28±0.00)×10 ¹⁵	1.38±0.02	1.24±0.00

5.2.6 Finite Element Electrostatic Modeling

The electric dipole formation at the metal/graphene interface and its effect on the electron transport is analyzed by using the commercial software FlexPDE [96] which solves the modeling problem of the electrostatic potential with finite element method. The energy band diagram for both junctions modeled in the calculation are shown in Fig. 5.9. Table 5.4 shows a list of the electrical parameters used in the calculation. The potential $U(x)$ at the metal and substrate is defined by solving one dimensional Poisson equation

$$d^2U(x)/dx^2 = -\rho(x)/\epsilon_0\epsilon_r \quad (5.8)$$

where $\rho(x)$ is the net charge. Here, we set the electrostatic potential to be zero at the metal surface. Then, the conduction band minimum (E_C) and valance band maximum (E_V) could be obtained from the relation of

$$E_C(x) = \phi_M - \chi_{SiC} - U(x) \quad \text{and} \quad E_V(x) = E_C(x) - E_g \quad (5.9)$$

where ϕ_M is the metal work function, χ_{SiC} the semiconductor electron affinity, and E_g the energy band gap. The net charge density in the 4H-SiC is given by

$$\rho(x) = -q[N_d - n(x) - p(x)], \quad (5.10)$$

and the electron density ($n(x)$) and hole density ($p(x)$) were calculated by using approximated form of Fermi-Dirac integral of order 1/2 [114]. On the other hand, there are more charges to be considered at the interface of substrate and graphene, including interface trap charge (Q_{it}), graphene charge (Q_G), and dipole charge (Q_D). First, the interface trap charge at the 4H-SiC surface [51], [115] is calculated as

$$Q_{it} = -qD_{it}(E_g - E_{CNL} - \phi_B) \quad (5.11)$$

where D_{it} is the interface trap density, E_{CNL} the charge neutrality level. When the E_{CNL} is assumed to be 2.44 eV [116], the D_{it} is determined as $8 \times 10^{11} \text{ cm}^{-2} \text{ eV}^{-1}$ by satisfying with the measured SBH for the Au/4H-SiC junction. This order of D_{it} well corresponds to the weak Fermi-level pinning effect of the 4H-SiC surface. It is assumed that the 4H-SiC surface of the Au/Gr/4H-SiC junction has the identical E_{CNL} and D_{it} values with that of the Au/4H-SiC junction. Next, the doping charge of graphene is expressed as

$$Q_G = q\Delta E_F |\Delta E_F| / \pi \hbar^2 v_F^2 \quad (5.12)$$

where ΔE_F is the difference between Dirac point and Fermi level in graphene and v_F ($=10^8 \text{ cm/s}$) the Fermi velocity of graphene. The Fermi level shift of the graphene is calculated by electrostatic potential drop from the metal surface

$$\Delta E_F = \phi_M - \phi_G - U. \quad (5.13)$$

The last parameter to be considered is the interaction dipole charge originated from the wave function overlap between the Au and graphene. In calculation, the dipole charge is considered as a thin charge sheet at the Au and graphene interface. Among the charges considered in the calculation, the interface trap charge and the doping charge are determined in advance by using material parameters and measured SBH. Then, the dipole charge of $1.0 \times 10^{-6} \text{ C/cm}^2$ is extracted to satisfy the SBH obtained by IPE measurement with equilibrium distance of 3.3 Å [103]. Note that the distance between graphene and 4H-SiC does not much affect the estimated SBH, so we set it as a minimum value (2 Å) to be possible to be calculated. Moreover, it is confirmed that the SBH could be modulated in amount of $\sim 0.1 \text{ eV}$ with the dipole charge.

Since graphene could be transferred roughly, the distance between graphene and 4H-SiC could be different locally [111], [112] and, therefore it induces the inhomogeneity of the SBH in the junction. When the sign of the interface trap charge is positive, the electrostatic potential drop across the gap between graphene and 4H-SiC increases. Therefore, the large gap could cause the reduced SBH with

increased potential drop. In the C-V and IPE measurements, this effect was not observed because the SBHs were measured by the majority parts of the different SBHs. On the other hand, it could be observed with using the I-V measurement because of the fact that the current flows less resistive region although that region is small. By using the dipole charge of $1.0 \times 10^{-6} \text{ C/cm}^2$ and the equilibrium distance of 3.3 \AA , the distance between graphene and 4H-SiC was extracted with 33 \AA to have the same SBH obtained from the I-V measurement.

Table 5.4 The parameters used for material electrical properties in finite element method.

ϕ_M (Au)	ϕ_G	χ_{4H-SiC}	χ_{SiO_2}	ϵ_{4H-SiC}	ϵ_{SiO_2}
5.4 eV	4.5 eV	3.5 eV	0.9 eV	9.7	3.9

5.2.7 Conclusion

In summary, the formation of an electric dipole between metal and graphene was studied by making Schottky junction with the substrate having weak Fermi level pinning effect. It is demonstrated that the Fermi level tuning and interface dipole formation by contacting graphene with metal could influence the electron transport in the junction, resulting in the reduction of SBH. The experimental results are consistently obtained from I-V, C-V, and IPE methods and the calculation using FlexPDE supports the claim on dipole formation at the interface of metal/graphene. The experimental result could be useful to understand the metal/graphene interaction in real graphene-used devices, like the graphene-Schottky junctions.

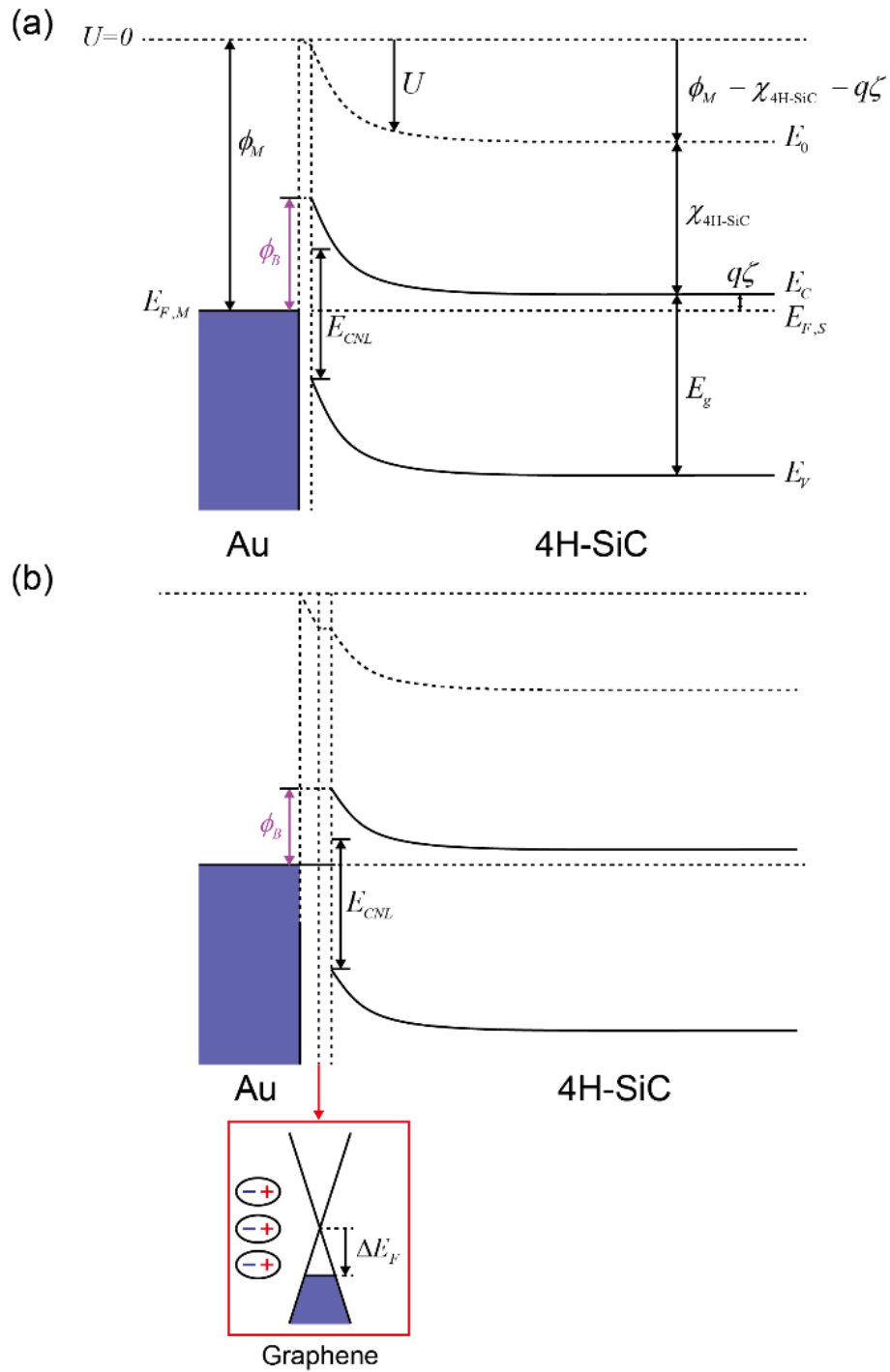


Figure 5.9 Band diagrams of (a) Au/4H-SiC and (b) Au/Gr/4H-SiC junctions. The parameters used in the calculation are denoted. Graphene has Dirac-cone shaped energy band.

5.3 Capacitive Memory Effect of Au/Cr/Al₂O₃/Al/Si Junction

Numerous alternatives to existing computers such as quantum computing and neuromorphic computing have been studied to efficiently process overflowing information [1], [117]–[119]. Memcomputing consisting of memory circuit elements (memelements) is also a potential candidate to simultaneously store and process information in the same location of the device [2]. Memelement characterized by M. Di Ventra *et al.* [120] is a key element of the memcomputing itself and can be used extensively including quantum and neuromorphic computing, leading to a new computing paradigm [121]–[125].

5.3.1 Memcapacitor

In the beginning of the 1970s, L. O. Chua suggested memristor (abbreviated for memory resistor) first, which is one of memory circuit element [126]. The concept of memory element expands to other circuit elements such as memcapacitor (abbreviated for memory capacitor) and meminductor (abbreviated for memory inductor) [120]. These memelements are considered to be a neuron for human brain system in that they are both information-storing and computing units. It allows their applications to parallel computing including quantum computing and neuromorphic computing [2].

Among three memelements, the interest in this part is memcapacitor whose symbol is shown in Fig. 5.10(a). An asymmetric property of terminals is described with black thick line in lower part. For voltage-controlled memcapacitors, $q(t)$ and $V_C(t)$ have the relation of

$$q(t) = C \left[\int_t^{t_0} V_C(\tau) d\tau \right] V_C(t) \quad (5.14)$$

and the system shows hysteresis loop like Fig. 5.10(b). The area of closed loop means added or removed energy from the system and it depends on the direction of the loop.

5.3.2 Sample Fabrication

An n-type Si (100) doped with donor concentration of $N_D = 10^{15} \text{ cm}^{-3}$ was used to fabricate Au/Cr/Al₂O₃/Al/Si junction [127]. The 1 cm × 1 cm Si substrate was cleaned by sonicating it in acetone and methanol for 5 min and then dipping it in BOE solution (BOE : DI = 1:6) for 30 sec to remove the native oxide grown on the Si surface. Schottky contact pattern was formed by photolithography using MA-6 mask aligner and the contact was made by depositing Al (3 nm) film with an e-beam evaporator and the following lift-off process. Then, 30 nm thick Al₂O₃ film is deposited by using atomic layer deposition (ALD) to cover the entire Schottky contact. It is considered that the Al₂O₃ film is thick enough not to allow electrons to flow through it. The photolithography process was performed again for the top electrode pattern. Then, Au/Cr (100 nm/10 nm) was deposited using e-beam evaporator and the lift-off process was followed to form the top metal electrode.

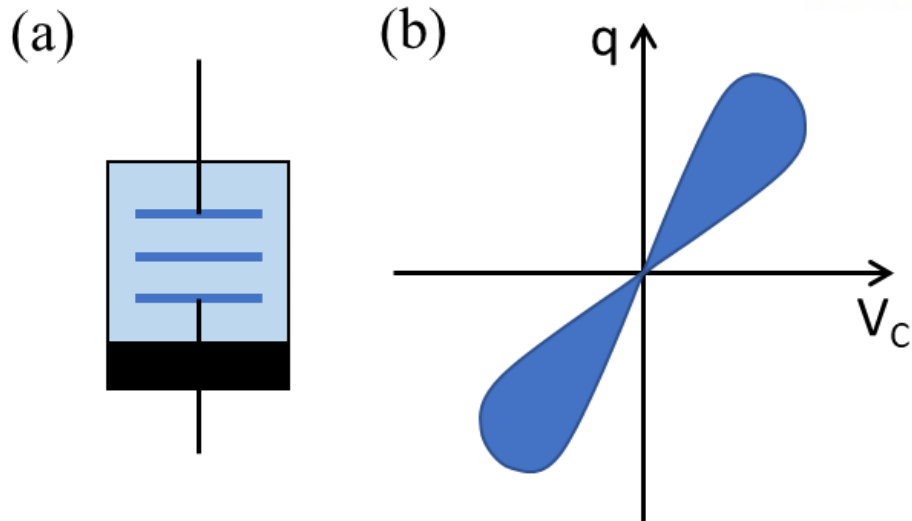


Figure 5.10 Characteristics of memcapacitor. (a) Electrical symbol of memcapacitor. In general, a positive voltage is applied to the upper terminal. (b) Hysteretic behavior of memcapacitor.

5.3.3 Working Mechanism

There are three kinds of internal state, such as geometric configuration, voltage, or time, to specify memcapacitance [120]. Two ways are suggested to determine the internal state of the memcapacitor [2]. One is to manipulate properties of dielectric materials. In this case, the different capacitance can be measured by a previous polarization state of the dielectric [128], [129]. It occurs because the motion of electrical carriers cannot follow the change in applied voltage. The other one is related to the geometric configurations of the memcapacitor, for example, area of the junction and thickness of dielectric layer [128]. The memcapacitor of metal/oxide/floating-Schottky junction operates based on changes in the geometric configuration of the capacitor, especially the separation of the capacitor electrodes. The electron transfer to and from the floating Schottky metal located between the substrate and thick insulating layer is controlled by varying the voltage pulses across the whole junction. Then, the depletion width varies spontaneously to compensate the differed negative charges in the floating metal. Here, the depletion region has positive space charges for the n-type substrate. In this manner, the depletion width can be controlled by applying voltage pulses with different signs and magnitudes, proving that it can lead to multi-level memcapacitive behaviors.

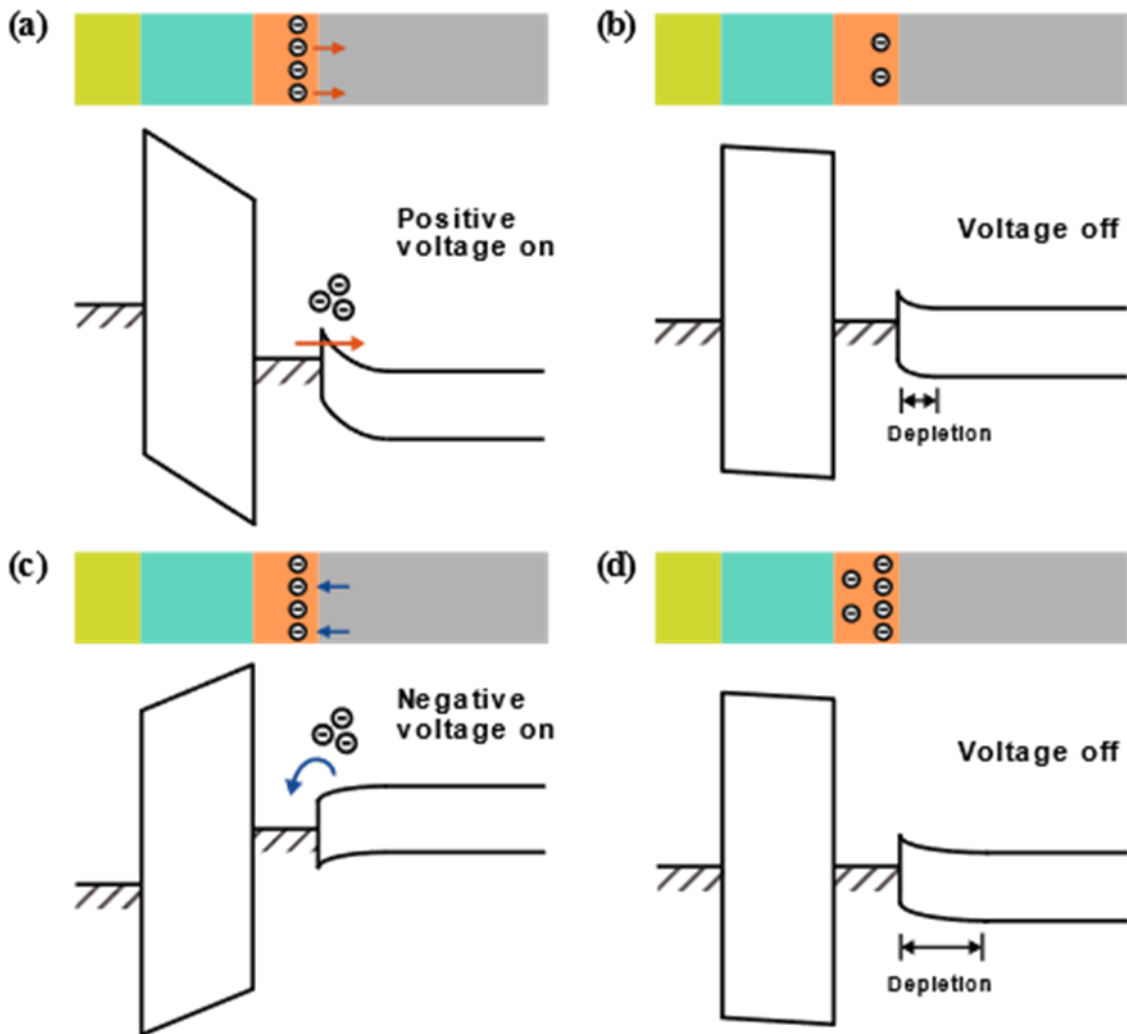


Figure 5.11 Energy band diagrams of the memcapacitor with a structure of metal/oxide/floating-Schottky junction. (a) Electrons in the floating metal flow into the substrate by applying a positive voltage on the substrate. (b) After the voltage is turned off, the depletion width decreases due to the reduction of electrons stored in the floating metal. (c) On the other hand, when a negative voltage is applied to the substrate, electrons in the substrate flows into the floating metal. (d) In this case, the depletion width increases with the increased number of electrons in the floating metal.

The following demonstrates how the depletion width is tuned by voltage pulses and the capacitance is changed accordingly. While a positive bias is applied to the semiconductor substrate, some electrons will migrate from the floating metal to the semiconductor (Fig. 5.11(a)). Then, the depletion width will decrease since the number of electrons in the floating metal needed to be screened out is reduced, which results in an increase in depletion capacitance (Fig. 5.11(b)). On the other hand, applying negative bias to the semiconductor substrate brings up electron flow into the floating metal. (Fig. 5.11(c)) Thus the depletion width increases, making the depletion capacitance decrease. (Fig. 5.11(d)) Here, it is assumed that there is no leakage of electrons through the insulating layer deposited on top of the Schottky contact and the electrons in the floating metal are to be trapped by the Schottky barrier during the bias-off state.

In the metal/oxide/floating-Schottky junction, two capacitors are connected in series; one is the top-metal/oxide/floating-metal structure and the other the underlying Schottky contact. The Schottky contact can be considered as a capacitor because its depletion region behaves as an insulating layer due to the lack of free electrons and the doped semiconductor and metal act as electrodes [51]. The capacitance of the top-metal/oxide/floating-metal capacitor (C_{ox}) is estimated to be ~ 33 times larger than that of Schottky contact (C_{dep}) because even though their relative permittivities are in similar range of 9 \sim 12, the depletion width of $\sim 1 \mu\text{m}$ is larger than the insulator thickness of $\sim 30 \text{ nm}$. Therefore, the effective capacitance of the total junction will be dominantly determined by the smaller depletion capacitance ($1/C_{tot} = 1/C_{dep} + 1/C_{ox}$), implying that the capacitive response by the voltage pulses is entirely due to a change in the depletion width.

5.3.4 Experimental Results

The memcapacitive behavior of metal/oxide/floating-Schottky junction was experimentally verified by fabricating Au/Cr/Al₂O₃/Al/Si junction as illustrated in Fig. 5.12(a). Lower pane of Fig. 5.12(b) shows how the memcapacitor responds by applied voltages of upper pane of Fig. 5.12(b). As shown in the top inset, all voltage pulses with a width of 1 sec and a frequency of 1 MHz were used to characterize the memcapacitive performances of junction; negative (-15 V) for erasing process and positive (2, 4, 6, and 8 V) for writing. The data retention of a memcapacitor was confirmed by measuring the capacitance for 600 sec with an interval of 10 sec without bias. The initial capacitance jump was observed immediately after the writing voltage pulse was applied. Then, it decreases somewhat rapidly and approaches any specific value corresponding to each writing voltage pulse as shown in Fig. 5.12(c). It is explained that the electrons moved to the semiconductor due to the applied voltage leak into the floating metal through the leakage path until the device reaches an equilibrium state. The capacitance difference between writing and erasing increases linearly with the voltage pulse and is specified on Fig. 5.12(d). This result shows that the proposed junction works as a memcapacitor having multi-level memory state.

It is necessary to have a stable initial state in order to function as a memory device. The capacitance was measured in the same way by changing the erasing voltage to -8, -12, and -15 V to find the

conditions with a stable initial state as shown in Fig. 5.13(a)-(c). When the voltage pulse of -8 V and -12 V that are not enough to fill the floating metal with electrons is applied, the capacitance value is significantly dispersed and increases as the erasing operations are repeated. When the magnitude of the erasing voltage is increased to -15 V, the reset state still increases but is almost saturated with a certain value as shown in Fig. 5.13(d). A condition having an initial state that has more constant value should be found in order to stably drive the memory device.

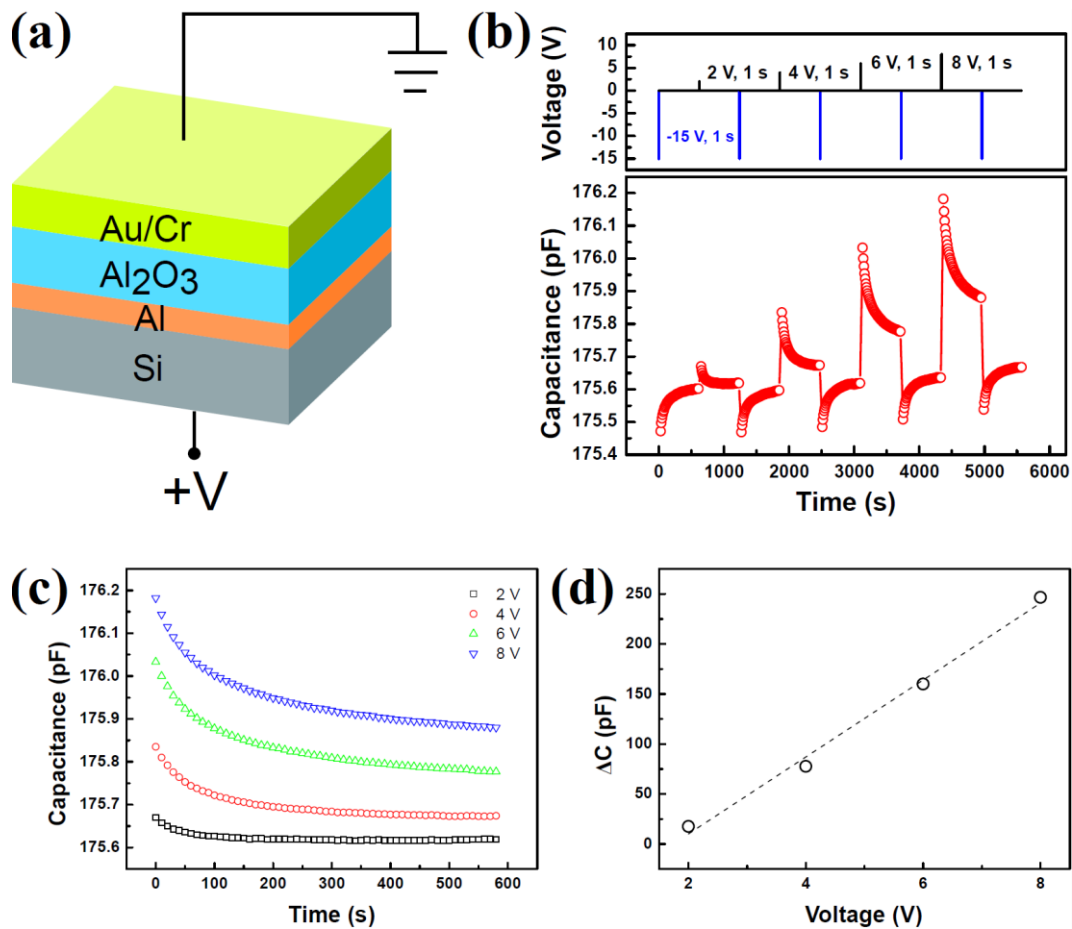


Figure 5.12 Memcapacitive characteristics of Au/Cr/Al₂O₃/Al/Si junction. (a) Schematic diagram of Au/Cr/Al₂O₃/Al/Si junction. Voltage pulse is applied to the semiconductor substrate. (b) The junction capacitance varies with the voltage pulse of 2, 4, 6 and 8 V. A negative voltage of -15 V is applied to reset the state. All pulses are applied for 1 sec and between pulses, there are time intervals of 600 sec to observe the data retention. (d) The capacitance-difference between writing and erasing states increases as the magnitude of voltage pulse increases.

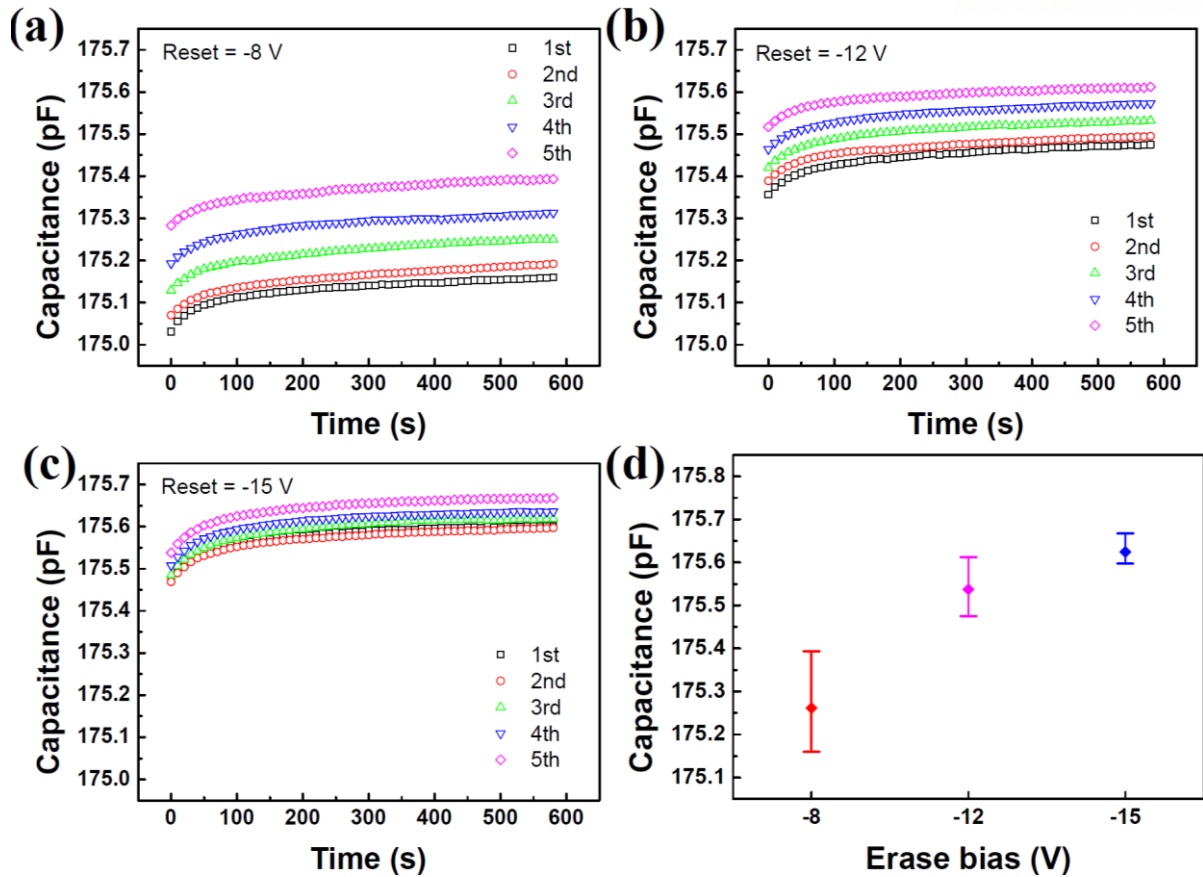


Figure 5.13 The fluctuation in junction capacitance depending on the erasing voltage (a) -8 V, (b) -12 V, and (c) -15V. The capacitance values were obtained from the pulse sequence of Fig. 5.12(b). (d) The distribution of saturated capacitance values after each writing voltage for different erasing voltage. With the higher erasing voltage, the states become stable with a reduced dispersion of capacitance.

Fig. 5.14 shows the capacitive memory behavior of Au/Cr/Al₂O₃/Al/Si junction as a form of hysteresis loop. The C-V loop is measured with following sequences: 0 V → |V_{max}| V → -|V_{max}| V → 0 V where |V_{max}| = 2, 4, 6, and 8 V. The voltages were applied for 1 sec and the capacitance was measured with the LCR meter after the applied voltage was turned off for 1 sec.

5.3.5 Conclusion

In conclusion, a memcapacitor structured with metal/oxide/floating-Schottky junction has been suggested. The proposed device actually functions as a stable memcapacitor showing the discrete capacitive memory states depending on different external voltage pulses. Each memcapacitive state is determined by the depletion width modulated with the number of electrons trapped in the floating metal. This work demonstrates that solid-state memcapacitors can be fabricated in simple manners by using

conventional semiconductor fabrication technology. Thus, it is expected that the metal/oxide/floating-Schottky junction will be used to realize neuromorphic and polymorphic computing as the precedent memristors do [130]–[132].

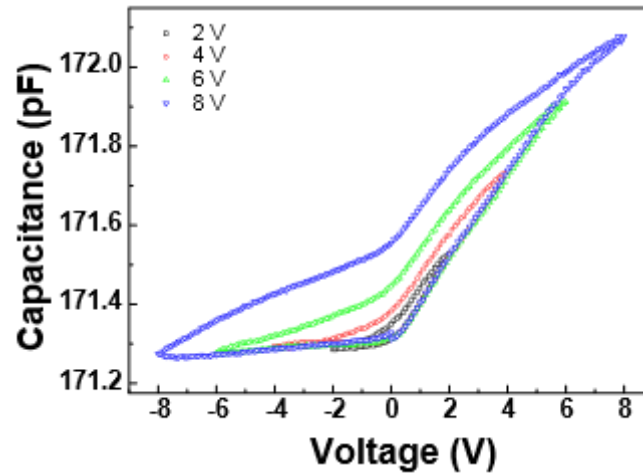


Figure 5.14 Hysteretic behavior of the Au/Cr/Al₂O₃/Al/Si junction in capacitance-voltage plot. The C-V hysteresis loops were obtained by sweeping voltage pulses with the duration of 1 sec onto substrate.

Chapter 6 . Squeezed State Generated by Josephson Parametric Amplifier

This chapter covers parametric amplifiers in the superconducting circuit QED, such as Josephson parametric amplifier (JPA) and Josephson parametric converter (JPC). First, the improvement of measurement efficiency with enough gain of both parametric amplifiers is demonstrated. The gains of each parametric amplifier are obtained with applied strong pump field. Then, using these parametric amplifiers, the squeezed state which is one of nonclassical quantum state is generated, and reconstructed with Wigner tomography.

6.1 Parametric Amplifier

In quantum optics, process becomes *parametric* when a nonlinear medium is used for frequency mixing and its refractive index is modulated by a strong pump tone [133]. By analogy with the optics, the refractive index corresponds to the impedance in the electrical circuits and the nonlinear medium to the Josephson junction in the superconducting circuits. Then, the parametric process in the microwave regime can be achieved by modulating either a capacitance or inductance. In the superconducting system, the impedance can be changed by varying the Josephson inductance with the magnetic flux applied through the SQUID. Since the parametric amplifier with the Josephson junction was demonstrated in 1970s [134], various forms of the parametric amplifiers have been developed. T. Yamamoto et al. has reported flux-driven JPA consisting quarter wavelength resonator and dc-SQUID [23]. L. Zhong et al. showed ~ 4.9 dB squeezing by using the flux-driven JPA with 10 dB gain [31]. M. A. Castellanos-Beltran and W. H. Lehnert [135] demonstrated widely tunable JPA with 400 SQUID arrays, which can be tuned in the range of 4-8 GHz and obtain ~ 28 dB gain. The JPC researched by N. Bergeal *et al.* [136] is also different form of JPA. Recently, the research on traveling wave parametric amplifier has increased [137] because it has wide bandwidth to operate and high gain.

In this section, the working principle of parametric amplification is described. Then, two types of amplification such as phase-preserving and phase-sensitive amplification are presented. At the end, the main performances of signal amplification with gain is followed.

6.1.1 Working Principle

The parametric amplification is a nonlinear process between a strong ‘pump’ tone at frequency ω_p , a ‘signal’ mode at frequency ω_s , and ‘idler’ mode at frequency ω_i as depicted in Fig. 6.1. The signal is amplified by transferring pump energy into each mode by frequency mixing. Depending on the pump frequency, the energy transfer method is divided into three-wave mixing or four-wave mixing. Literally,

it means the number of photons involved in the process. The signal, idler, and pump photons are used for the three-wave mixing with the relation of $\omega_P = \omega_S + \omega_I$. On the other hand, one signal, one idler and two pump photons are engaged for the four-wave mixing where $2\omega_P = \omega_S + \omega_I$ [29]. In the parametric process, the energy of pump photon is converted into signal and idler photons, revealing the amplification of both modes.

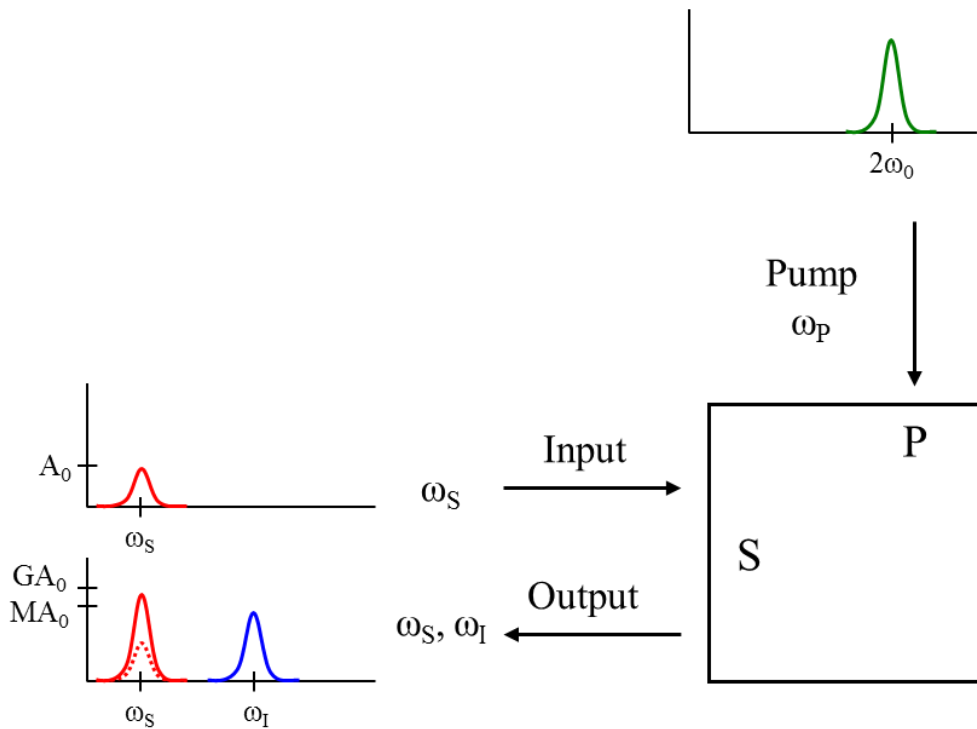


Figure 6.1 Parametric amplification process. The input signal is amplified by the nonlinear interaction between the pump tone and the signal mode.

Moreover, the amplification process can be classified by relation between the signal and idler frequencies. When they are located at different frequencies ($\omega_S \neq \omega_I$), it is called as non-degenerate or phase-preserving amplification. However, when they have same frequency ($\omega_S = \omega_I$), the process is called as degenerate or phase-sensitive amplification. In Fig 6.2, both amplifications are depicted in phase space where the equal fluctuations of the input signal in both quadratures are represented by a circle. In the non-degenerate mode, the amplified signal is also represented as a circle and surrounded by an additional noise as shown in Fig. 6.2(a). On the other hand, when the parametric amplifier operates in the degenerate mode, the signal is amplified in one quadrature and deamplified in the other quadrature without any added noise, generating squeezed state as shown in Fig. 6.2(b).

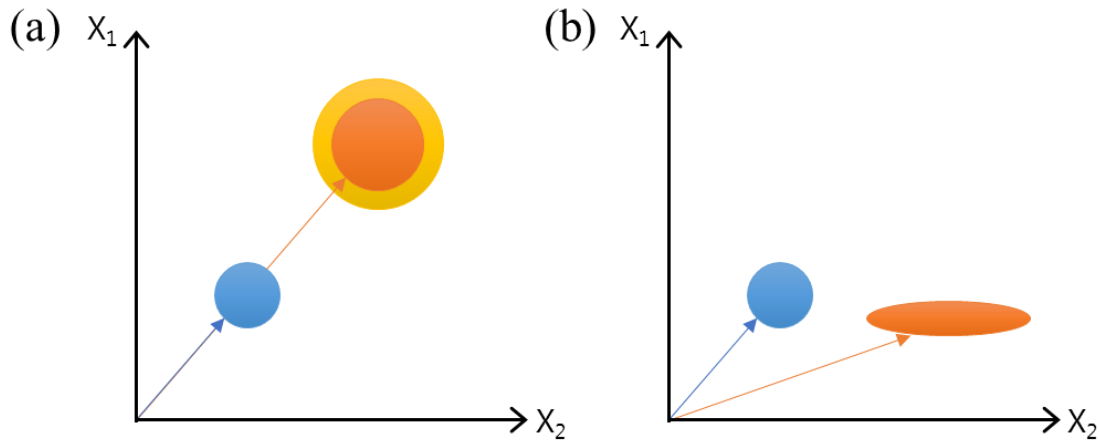


Figure 6.2 Type of parametric amplification in respect to the phase. (a) The amplitude and fluctuation of the signal are amplified equally without phase dependence under the phase-preserving amplification. (b) The amplitude and fluctuation are amplified in one quadrature but deamplified in the other for under the phase-sensitive amplification.

6.1.2 Phase Preserving Amplification

When output signal has no phase-dependence on input signal, it is called as a phase-preserving amplification or nondegenerate amplification. In this amplification, half a photon $hf/2$, which is a minimum amount of noise, is added to the signal [22], [138]. For the phase-preserving amplifier, the pump frequency is given by the sum of signal and idler frequencies ($2\omega_p = \omega_s + \omega_i$). The amplifier can operate in two different ways depending on frequency mixing, an amplifier with photon-number gain for frequency up-conversion ($\omega_s + \omega_i$) and a converter without photon-number gain for frequency down-conversion ($|\omega_s - \omega_i|$) [139], [140]. As shown in Fig. 6.2(a), the signal is amplified by a factor of \sqrt{G} without any phase dependence, where G is gain. In the amplification, the noise is also increased with same amount for both quadratures. This device is useful to carry a signal containing the information in both quadratures [136].

Josephson parametric converter (JPC) is a representative example of the phase-preserving amplifier. A circuit of the JPC with lumped elements is depicted in Fig. 6.3. The amplifier is structured with two resonant modes and Josephson ring modulator (JRM) which is composed of four Josephson junctions in Wheatstone bridge and located at the intersect where the signal and idler resonators are crossed orthogonally. The device has been studied from the basic working mechanism [141], [142] to application for qubit readout [26]. Although the device operates as the phase-preserving amplifier, two-mode squeezing can be produced because it is comprised of two separate modes [143], [144].

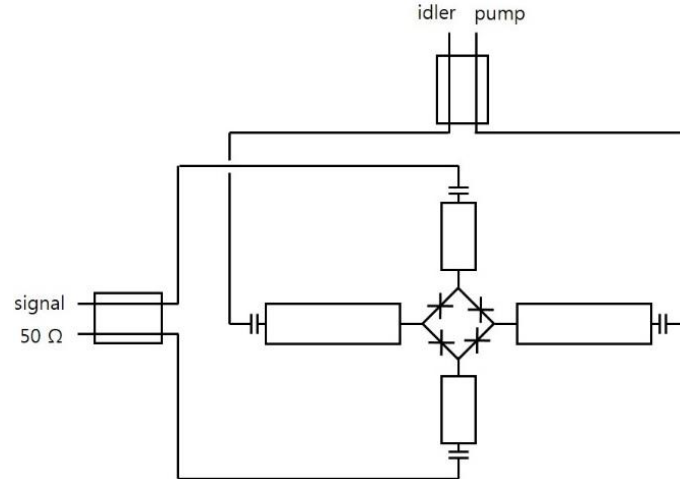


Figure 6.3 Circuit schematic of the JPC. Two different modes called as signal and idler intersect at the center through JRM. The pump is applied with the mode to be amplified and the remained port is terminated with 50Ω .

6.1.3 Phase Sensitive Amplification

On the other hand, a phase-sensitive amplifier has phase-dependence in that the signal is amplified in one quadrature and de-amplified in the other as shown in Fig. 6.2(b). In this amplification, the signal quadrature in the same direction with the pump is amplified by \sqrt{G} , while the one in orthogonal direction is de-amplified by $1/\sqrt{G}$. This property of the phase-sensitive amplifier allows the device to squeeze vacuum fluctuations. In contrast to the phase-preserving amplifier, the phase-sensitive amplifier operates with only one resonant mode [23], [135], [145] and is driven by the strong pump tone at twice the signal frequency ($\omega_P = 2\omega_S$).

The JPA has been widely studied as the phase-sensitive amplifier and designed in various forms as shown in Fig. 6.4. At first, the researches on the JPA was conducted to obtain high gain and wide bandwidth. The gain performance was enhanced up to 37 dB in 2014 [25] and the wide dynamic range was achieved by using Josephson junction arrays [133]. In addition to the quantum-limited noise performance with gain and bandwidth, the squeezing has been demonstrated for many applications [146]–[148]. More recently, this low-noise amplifier has been used in the qubit measurements including single-shot qubit readout with high fidelity [27], [28], quantum trajectories [149], [150], and nonclassical photon number distribution [151].

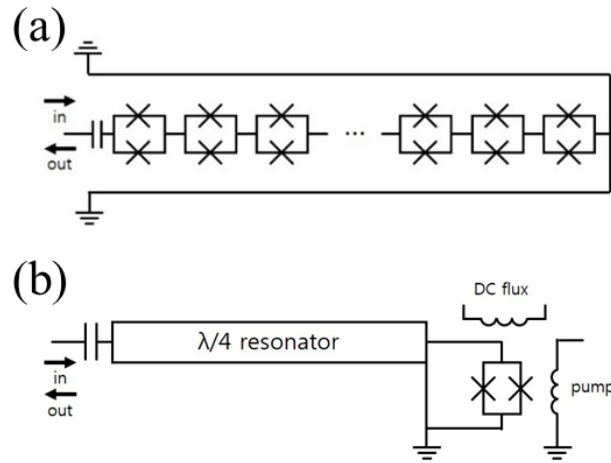


Figure 6.4 Circuit schematic of two types of JPA. (a) Widely tunable JPA with SQUID array [135] and (b) flux-driven JPA [23].

6.1.4 Gain Performance

The amplified signal is illustrated in Fig. 6.5. A performance of amplifier is determined with gain (G) which is a ratio between input and output power. Therefore, the gain is a quantitative parameter to measure the amplification and usually expressed in dB. The gain increases with higher pump power. However, at a certain point, the gain is reduced and when the gain is decreased by 1 dB, it is called as 1 dB compression point. It is related to dynamic range of amplifier. Bandwidth (B) is another parameter to define the amplifier's performance. It implies the working frequency range of the amplifier, in which the signal intensities are over a half of maximum amplitudes.

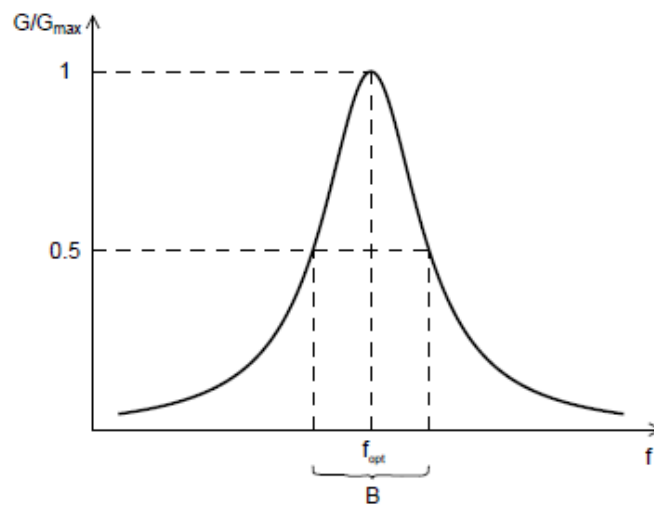


Figure 6.5 Amplified signal having gain of G_{\max} and bandwidth of B .

6.2 Parametric Amplifier Measurements

Parametric amplifiers are divided into two groups depending on the phase-dependence, which is phase sensitive amplifier and phase insensitive amplifier. JPA and JPC are the representative parametric amplifiers. In the experiments, both amplifiers are used as a squeezer for the JPA and an amplifier for the JPC to generate the squeezed state. The initial state is squeezed by the JPA and then, the output signal is amplified by the JPC to enhance the quality of detection. Before the squeezed state is generated, the amplification properties of both parametric amplifiers are characterized in respect to the qubit measurement.

6.2.1 Josephson Parametric Amplifier

The JPA has two ports, one for signal and the other for pump. Actually, the JPA works in reflection mode with one port, but the input and output signals are separated with the circulator in the experiment. The microwave input is generated by vector network analyzer (VNA) and injected by port 1 as a source. The other port 2 is used as a receiver and the transmitted signal is detected in the form of scattering parameter, S_{21} . The flux dependence of the JPA is observed by sweeping the probe microwave tone from 6 GHz to 9 GHz with 1001 points under NA power of -50 dBm. The magnetic flux is applied by sweeping the current from -1 mA to 1 mA with the spacing of 0.02 mA. The measured flux dependence is plotted in Fig. 6.6. The resonant frequency is repeated periodically with a current interval of 0.7 mA.

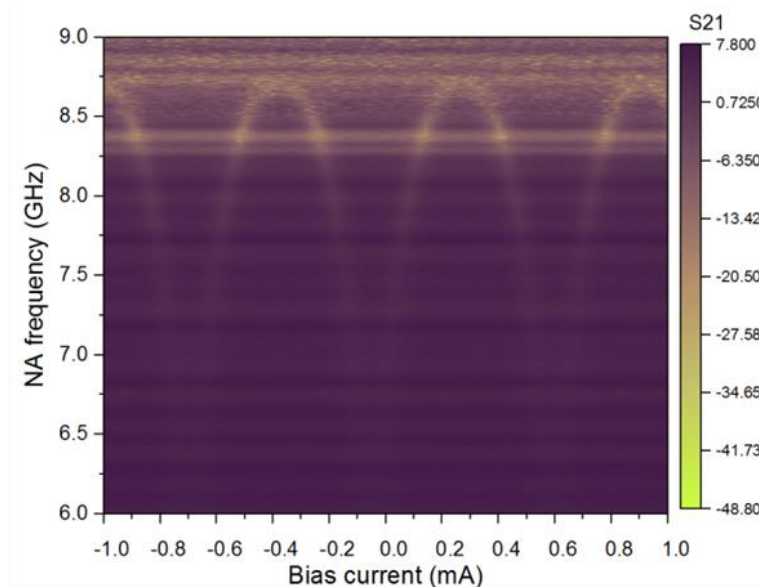


Figure 6.6 Flux dependence of the resonant frequency of JPA. The magnetic flux is applied by sweeping the current.

Before the experiments with the qubits, the amplification properties of the JPA are characterized at the specific frequency. For the experiment, the qubit with transition frequency (f_{01}) of 5.5480 GHz was prepared and the shifted cavity frequency (or ground state frequency) due to coupling between qubit and cavity was $f_g = 7.56461$ GHz. The JPA resonant frequency was set to be coincided with the ground state frequency. The bias current was chosen to be 0.14 mA which was found by changing the current through programmable DC source. Then, by applying the pump tone with twice signal frequency ($f_p = 15.12582$ GHz) for the operation in nondegenerate mode, it is possible to find the amplification of JPA with the maximum gain of 10.8 dB as shown in Fig. 6.7.

Next, the improvement of measurement efficiency with the JPA was investigated. The transmon qubit in 3D resonator was mounted in front of the JPA. By adding two isolators between the resonator and JPA, the signal was prevented from the back reflection. The parts of Rabi oscillations of the qubit are shown in Fig. 6.8 for the effect of using JPA in the measurement. It is observed that the oscillations become apparent with even less average.

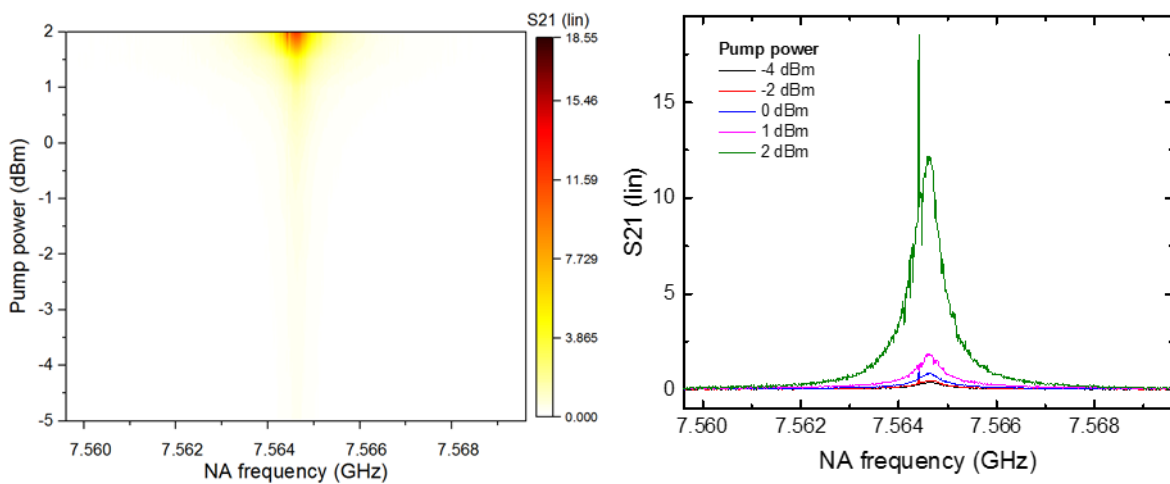


Figure 6.7 Amplified signal of the JPA with the maximum gain of 10.8 dB.

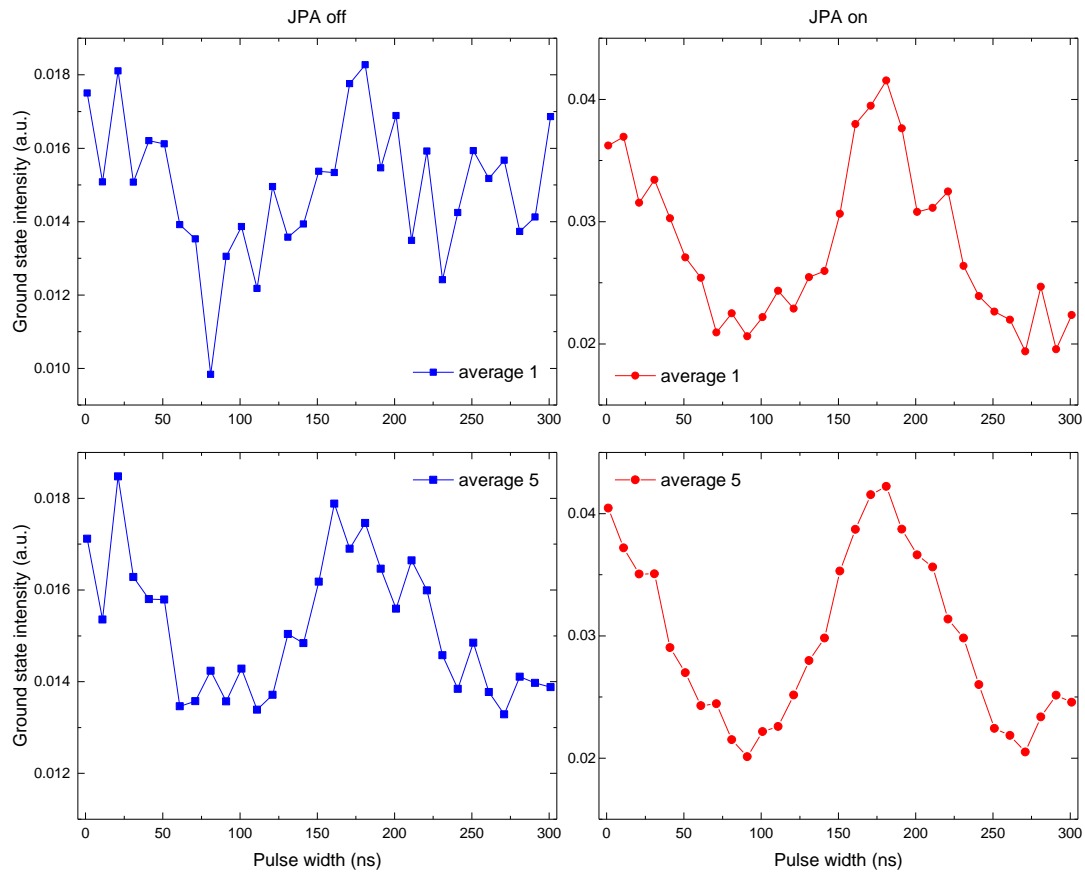


Figure 6.8 Improvement of noisy measurement by using JPA.

6.2.2 Josephson Parametric Converter

JPC was purchased from Quantum Circuit, Inc. and full specification of the JPC SN019 is listed in Table 6.1. For the signal and idler modes of JPC, 1dB compression points are specified in the range from -140 dBm to -120 dBm. Bandwidths of both resonators are estimated to be ~ 6 MHz with the maximum value of 12 MHz.

Table 6.1 Operation range for JPC with 20 dB gain.

SN019	f_{\max} (GHz)	f_{\min} (GHz)
Signal mode for 20 dB gain	7.549	7.208
Idler mode for 20 dB gain	5.179	5.014

The JPC consists of two transmission lines (signal and idler) intersecting at the center of each resonator. A coil placed right below the device introduces an external magnetic flux and the flux dependences of the resonant frequency of the signal and idler resonators are shown in Fig. 6.9(a) and (b), respectively. To determine the resonant frequency, the phase response was measured with VNA by sweeping the microwave tone from 6 GHz to 8 GHz for the signal resonator and from 4 GHz to 6 GHz for the idler resonator. The current through the coil is swept from -2 mA and 2 mA with the spacing of 0.01 mA. In this bias measurement, only one resonator is of interest and the ports of the other resonator are terminated.

After the flux dependences on the bias current are obtained for the signal and idler modes, the amplification properties can be determined. Unlike the JPA operated in degenerate mode, the JPC works in non-degenerate mode where the signal and idler frequencies are different. Now, both resonators are connected with SMA connectors and the pump tone is applied to the resonator to measure the gain properties. A collection of the JPC response to the pump is shown in Fig. 6.10. For the signal mode, the resonant frequency is set to be 7.3667 GHz at $I_b = -0.42$ mA. Based on the bias maps obtained from the previous stage, the pump frequency is determined by the sum of the signal frequency and the expected idler frequency. Then, the gain of JPC is measured by increasing pump power gradually. With the power having the maximum gain, the pump frequency is swept with the spacing of about 20 MHz. Finally, the optimal pump power and pump frequencies are determined by repeating these processes and Fig. 6.10(a) and (b) show the response in the signal mode to the pump power and frequency. The signal mode shows the maximum gain of 20.0 dB with pump frequency of 12.494 GHz and pump power of 0 dBm. Here, the power of microwave tone is the value set in the microwave source. In the same way, the performance of idler mode ($f_i = 5.0384$ GHz at $I_b = -0.465$ mA) was measured with the maximum gain of 18.8 dB with pump frequency of 12.185 GHz and pump power of -22.6 dBm. The response in the idler mode to the pump is shown in Fig. 6.10(c) and (d).

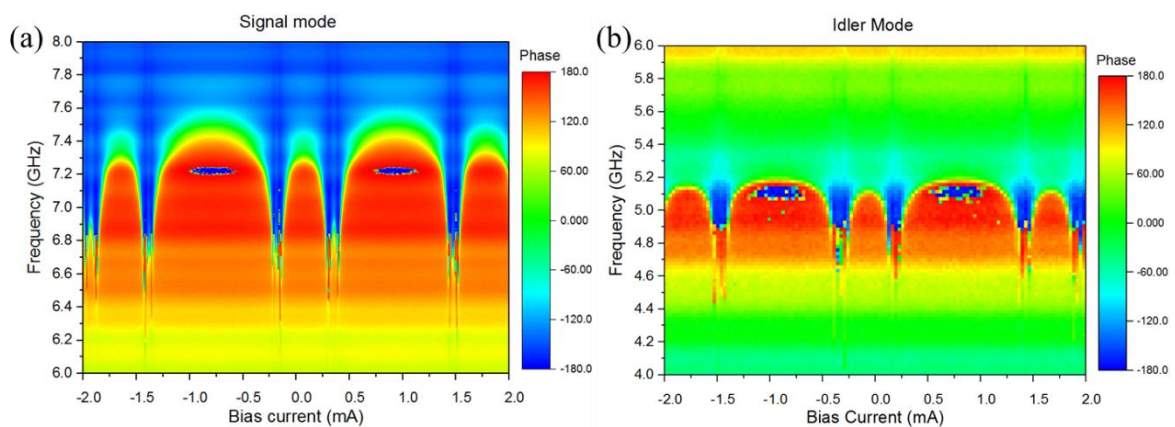


Figure 6.9 Flux dependence of the resonant frequency of (a) signal and (b) idler resonators of the JPC.

Since the measurement is conducted in the range of 7-8 GHz, the signal mode of JPC for the qubit measurement is used. Based on the pump condition obtained the previous experiment, the transmitted signal at the ground state frequency is amplified as shown in Fig. 6.11(a). To operate the JPC, the current is applied at $I_b = -0.42$ mA and the pump tone is injected with the frequency of 12.505 GHz and power of 0.1 dBm. Also, the Rabi oscillations when the JPC is on and off are compared as shown in Fig. 6.11(b). Without the support of JPC, it is hard to observe to detect the oscillation due to noisy signal. However, the JPC makes clear Rabi oscillations by improving the measurement efficiency.

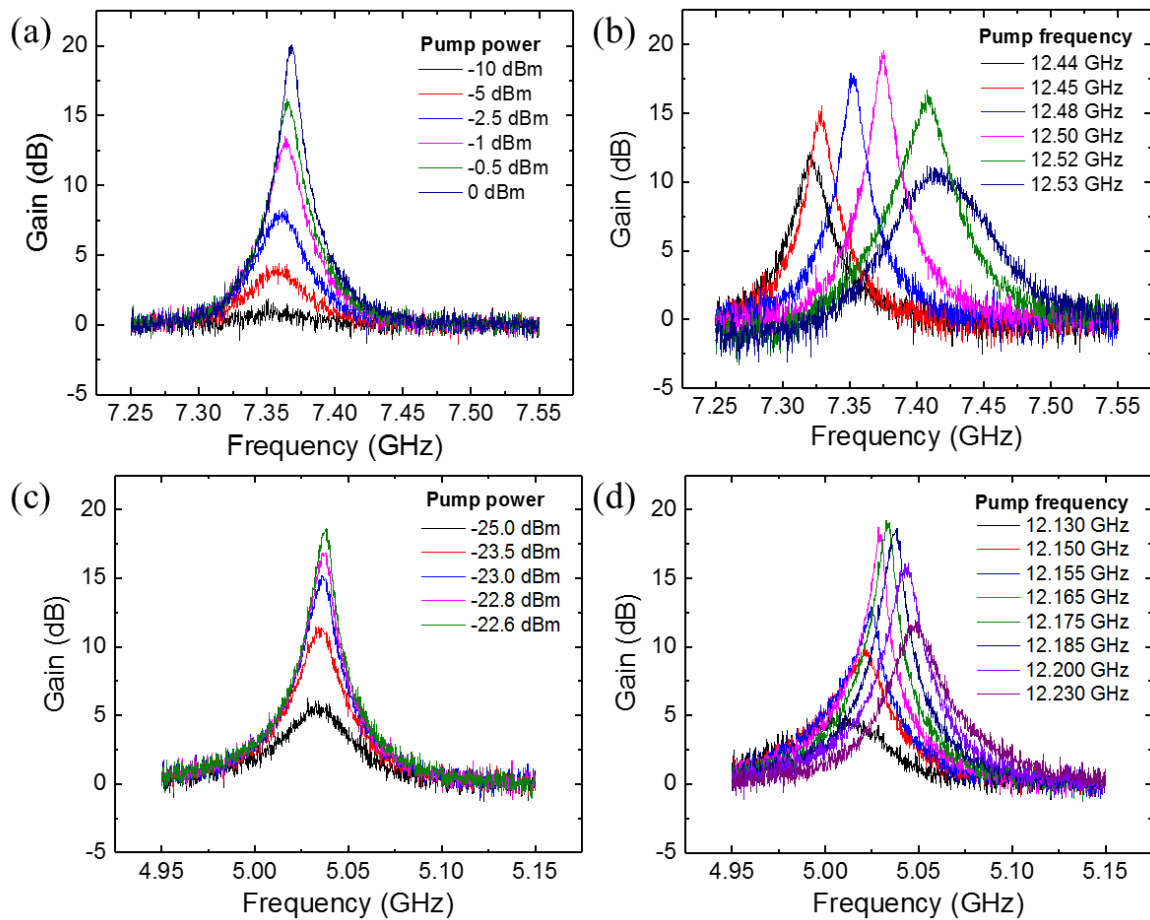


Figure 6.10 JPC gain curves for different pump power and frequency for (a), (b) signal resonator and (c), (d) idler resonator.

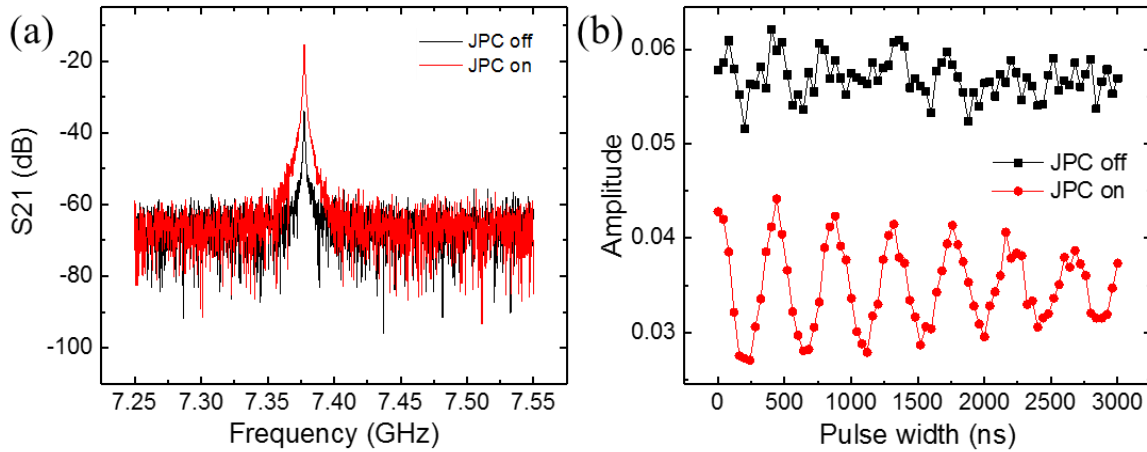


Figure 6.11 Application to qubit measurement with JPC. (a) Amplified signal at the ground state and (b) improved Rabi oscillations with JPC.

6.3 Generation of Squeezed State

As discussed in previous section, the squeezed state can be generated by JPA operated in degenerate mode. In this experiment, the squeezed state is characterized by homodyne detection probing the noise fluctuation. Using the data obtained from the homodyne detection and MLE, the density matrix and Wigner tomography are conducted on the resulted state.

6.3.1 Experimental Results

A schematic of experimental setup is shown in Fig. 6.12(a). In this study, two parametric amplifiers were used, the JPA for a squeezer and the JPC for an amplifier. Both parametric amplifiers were mounted and measured at the base temperature of ~ 7 mK in a dilution fridge. Respective cylindrical shields are used to protect them from external magnetic field. Because the parametric amplifiers operate in reflection mode, the incident and reflected signals were separated by using circulators. Two isolators were followed to transmit the reflected signal in one direction and block the back-reflection. Then, the signal was amplified by the JPC. To operate the JPA and the JPC, the strong microwave field was applied through separate pump ports. The frequency of incident signal is 7.35 GHz. The resonant frequencies of the parametric amplifiers were controlled by current injected through a bias tee for the JPA and an independent coil for the JPC to coincide with the signal frequency.

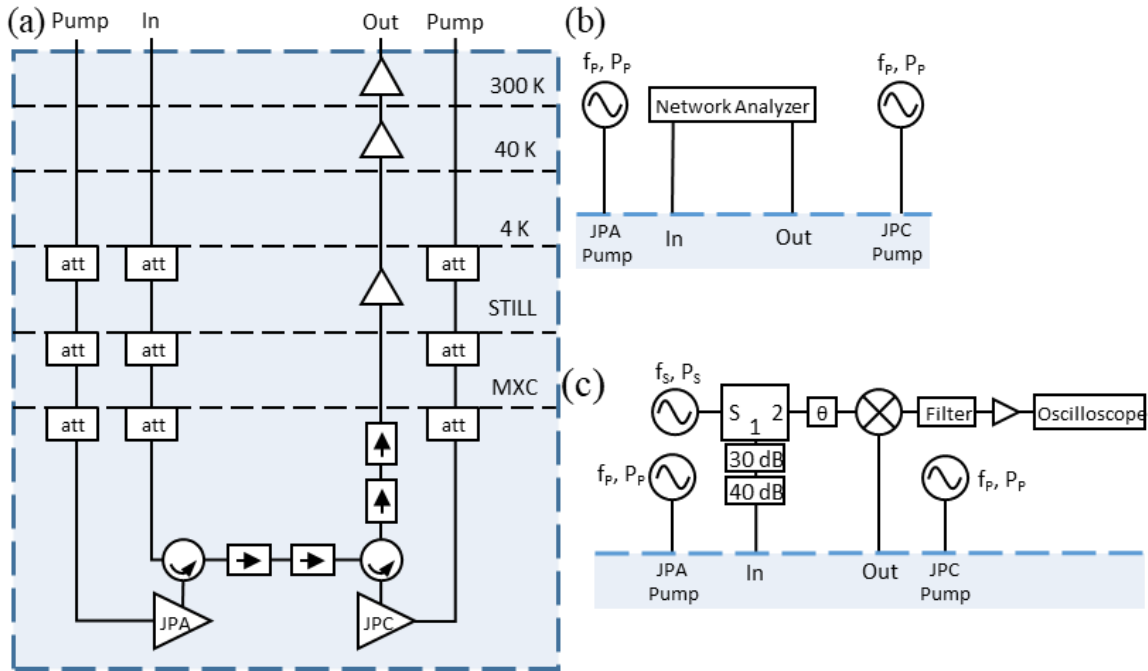


Figure 6.12 Experimental setups for measuring squeezed state. (a) Schematic of the cryogenic components inside the cryostat. Measurement setup for (b) amplification using VNA and (c) homodyne detection using oscilloscope.

The parametric amplifiers were characterized by using a vector network analyzer (VNA) as shown in Fig. 6.12(b). With the help of the circulator, the response of parametric amplifiers in the reflection mode was measured with the transmission in two-port network. In order to demonstrate the squeezed state, quadrature information was obtained by homodyne measurement as shown in Fig. 6.12(c). The microwave field is divided by an RF splitter, applying one for input signal and the other for local oscillator (LO). For the homodyne detection, the LO is mixed with the output signal using a MARKI RF microwave mixer which needs the LO power in range of 7-10 dBm. Meanwhile, the incident signal is attenuated by 70 dB for a low readout photon. The down-converted signal resulted from mixing LO and output signals is filtered in a range from DC to 1.9 MHz. The signal is then amplified with SR445A and detected by oscilloscope.

First, the flux dependences of the JPA and JPC were measured again for the experiment as shown in Fig. 6.13(a) and (b), respectively. The responses of phase for both amplifiers were measured in the range of 6-9 GHz under NA power of -55 dBm. The magnetic flux was applied by sweeping the current from -1 mA to 1 mA for the JPA and from -2 mA to 2 mA for the JPC with the spacing of 0.01 mA.

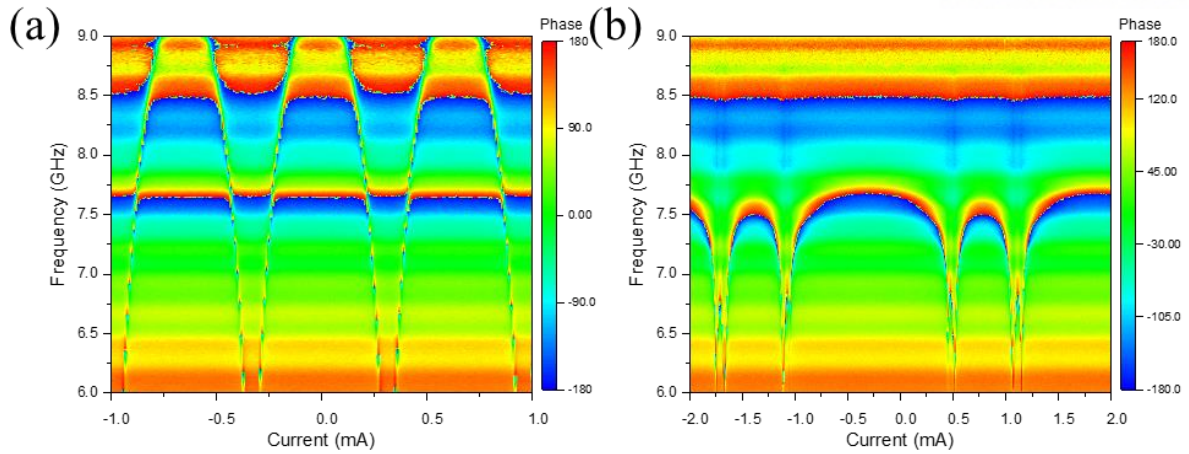


Figure 6.13 Flux dependence of the parametric amplifiers, (a) JPA (b) JPC.

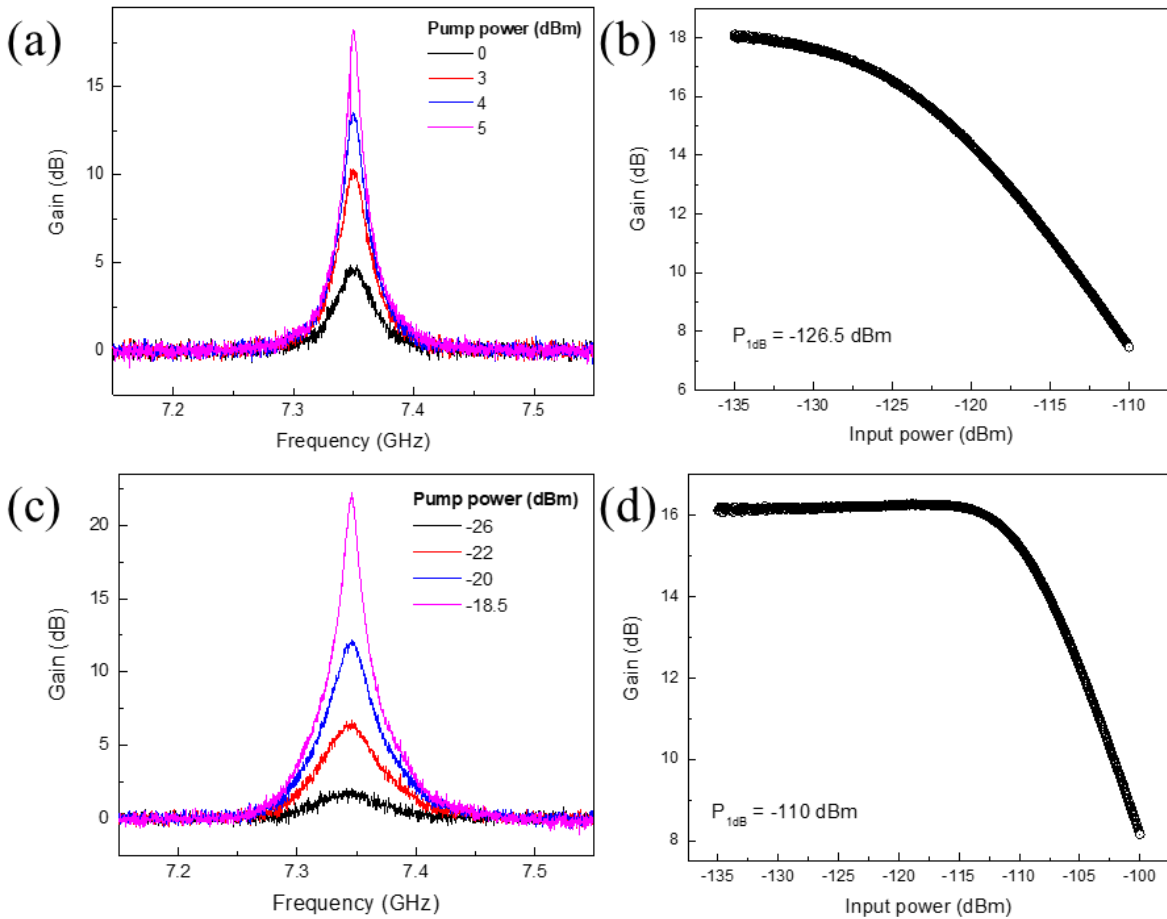


Figure 6.14 Amplification properties of the parametric amplifiers. Gain depending on the pump power and 1dB compression points for (a), (b) the JPA and (c), (d) the JPC.

Then, the pump tone is optimized with respect to the frequency and power. At the pump port, a microwave field with twice the resonant frequency ($\omega_0 = 7.35$ GHz) was applied. It is because the JPA is operated as degenerate amplifier where the signal and idler frequencies are equal. The amount of amplification, or gain, was given in Fig. 6.14(a) depending on the pump power. In this experiment, the JPA was operated at the pump power which the JPA has the maximum gain of 18 dB. Also, the 1 dB compression point was measured to be -126.5 dBm. (Fig. 6.14(b)) The JPC operation was also characterized. Because the JPC is nondegenerate amplifier, the pump frequency is determined by the sum of signal and idler frequencies, i.e. $\omega_p = \omega_s + \omega_i$. In the same way, the largest gain of JPC at the same resonant frequency is 22 dB and the 1 dB compression point with the pump power of -19 dBm was -110 dBm as shown in Fig. 6.14(c) and (d).

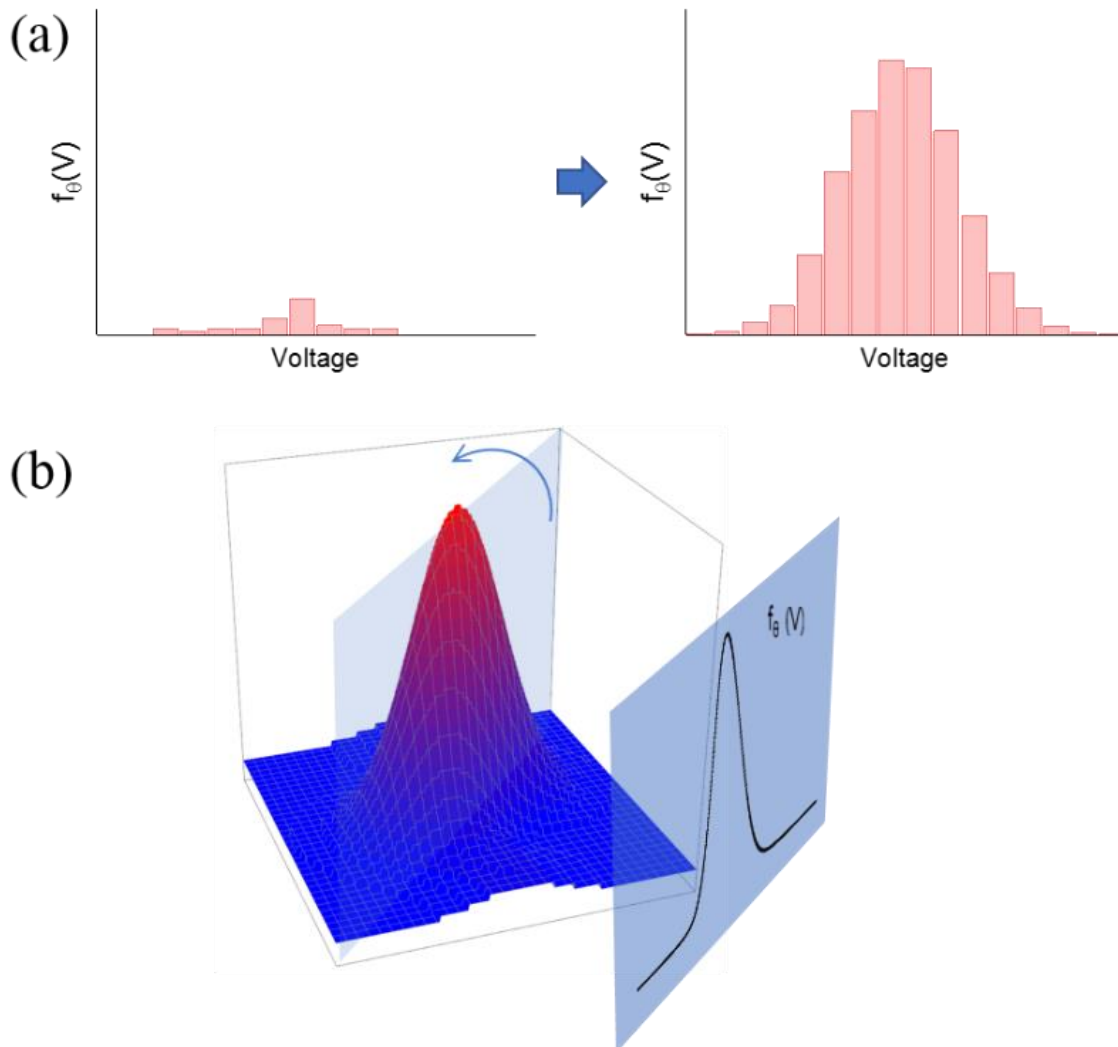


Figure 6.15 Measurement of marginal distributions. (a) At a certain phase, the distributions can be plotted by repeating the measurement of voltage magnitude. (b) When all distributions are found for different phases, the given state can be defined.

Since the JPA operates in the degenerate mode and JPC in the nondegenerate mode, each device works as a squeezer and an amplifier, respectively. When changing the phase of LO in the homodyne measurement, the phase dependence of the generated state can be measured. At a certain phase, the magnitude of voltage signal is measured repeatedly and then, the marginal distributions can be obtained as shown in Fig. 6.15(a). When the distributions in the range from 0° to 180° are found, the given state can be estimated like Fig. 6.15(b). The experimental results of JPA-off state and JPA-on state are shown in Fig. 6.16(a) and (b), respectively. When the JPA is off, all distributions are nearly same (Fig. 6.16(c)), showing no phase dependence. On the other hand, when the JPA is on, or the pump tone is applied, the squeezed state is generated, and the phase dependence is observed as shown in Fig. 6.16(d). The variation of the detected signal with respect to the phase is shown in Fig. 6.16(e). It is possible to find the phase which is below the JPA-off level.

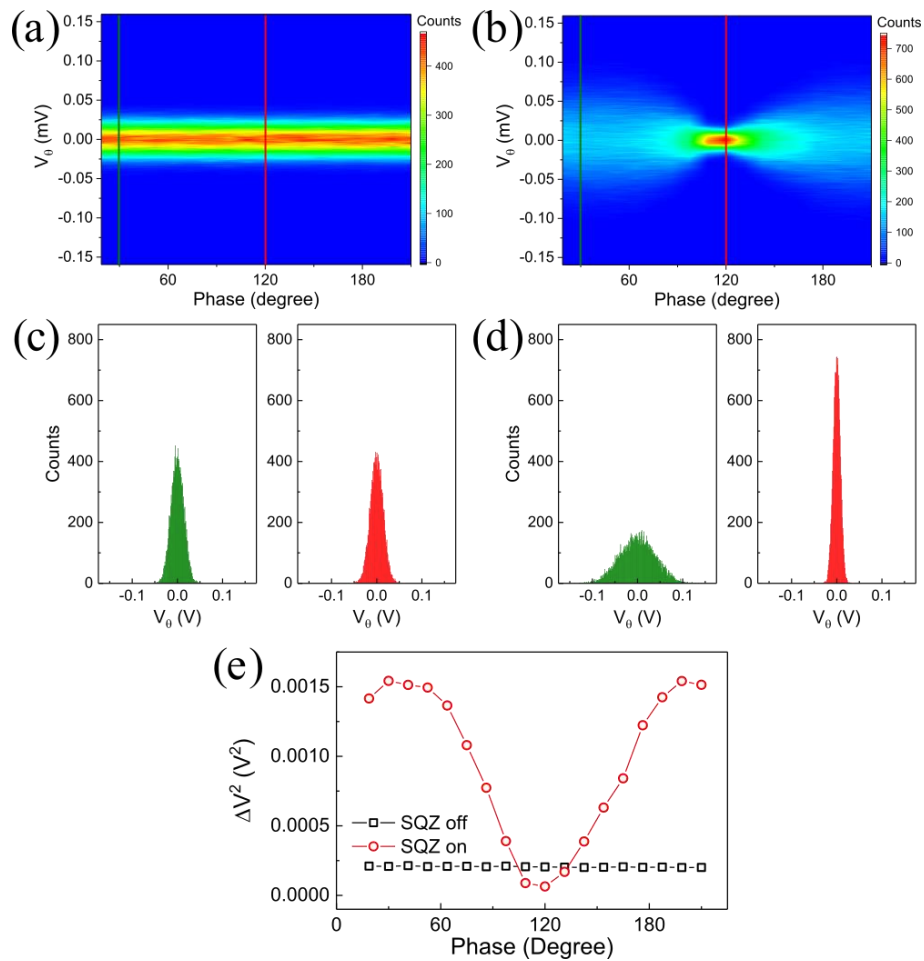


Figure 6.16 Experimental results of distributions at each phase. (a), (c) For the JPA-off state, the same distributions are measured. On the other hand, (b), (d) the different distributions are observed with respect to phase for the JPA-on state. (e) The phase dependence of squeezed state is confirmed by variation of the distributions.

6.3.2 Wigner Tomography

The quantum state can be inferred from the measurement data by using maximum likelihood estimation (MLE). Especially, iterative MLE method [152], [153] is used to define the density matrix of the state. By using conversion factor, the measured values are rescaled, $f_\theta(V) \rightarrow f_\theta(x)$. Then, the projected probability at a certain phase is calculated by

$$pr_\theta(x) = Tr[\hat{\Pi}(x, \theta)\hat{\rho}] \quad (6.1)$$

where $\hat{\Pi}(x, \theta)$ is the operator $\hat{\Pi}(x, \theta) = |x, \theta\rangle\langle x, \theta|$. Then, iteration operator can be defined as

$$\hat{R}(\hat{\rho}) = \sum_{x, \theta} \frac{f_\theta(x)}{pr_\theta(x)} \hat{\Pi}(x, \theta). \quad (6.2)$$

Using the iteration of $\hat{\rho}_{n+1} = N[\hat{R}(\hat{\rho}_n)\hat{\rho}_n\hat{R}(\hat{\rho}_n)]$ where N implies that trace is to be unity, the given density matrix can be estimated.

The distributions measured at each phase with the homodyne method were converted to the photon number basis and the iterative MLE process was conducted. The obtained density matrix for the JPA-off and JPA-on states are shown in Fig. 6.17 (a) and (b). For the squeezed state, only even number of photon numbers are presented because the signal and idler photons having same frequency form a pair.

The Wigner tomography gives the phase information visually unlike the density matrix representation. The Wigner function is written by

$$W(x, p) = \frac{1}{h} \int e^{-\frac{i2\pi py}{h}} \psi(x + y/2)\psi^*(x - y/2)dy. \quad (6.3)$$

Fig. 6.17 (c) and (d) are the results of Wigner tomography for the JPA-off and JPA-on states, respectively. For the JPA-off state, the circular shape is shown due to no phase dependence. On the other hand, the JPA-on state shows the squeezing in a direction.

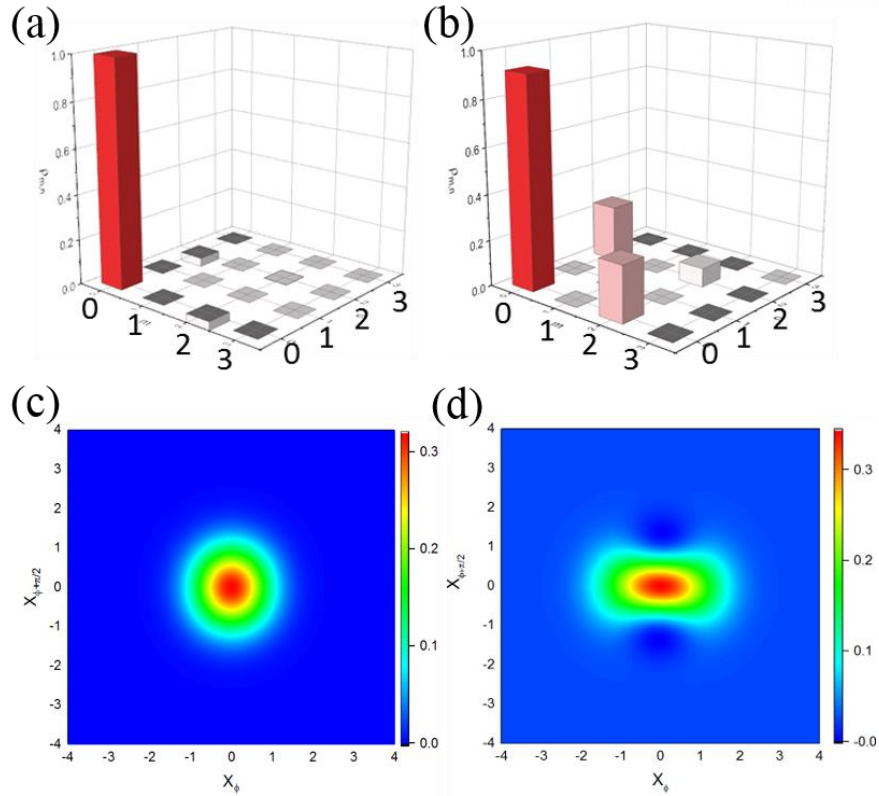


Figure 6.17 Representation of (a), (c) JPA-off and (b), (d) JPA-on states with photon numbers and Wigner tomography. When the squeezed state is generated, only even number of photons are presented. The squeezed state is reconstructed by using Wigner function, showing phase-dependence.

6.3.3 Conclusion

The squeezed microwave photon has been generated by using JPA and amplifying the signal with JPC. The squeezed state is characterized with the density matrix obtained from the MLE and reconstructed by using Wigner function. It is hoped that the squeezing enhances the measurement efficiency by reducing the noise and also the gate fidelity.

Chapter 7 . Quantum State Tomography with Circuit QED

Defining quantum state is important to develop quantum information processing. In this chapter, quantum state tomography (QST) in superconducting multi-qubit system is discussed. The quantum state is represented by various ways such as density matrix and Wigner tomography. The QST is a method to estimate the quantum state with pre-rotations. Joint readout method is introduced to measure multi-qubit contributions. Through the experiment, the quantum state in three-qubit system is represented as a form of density matrix. In the following section, two-qubit QST is demonstrated with microwave-activated phase (MAP) gate and its phase compensation with hyperbolic secant shaped pulses.

7.1 Multi Qubit Measurement

Quantum state of qubits can be represented by a density matrix using QST. The representation of single qubit is simple because it is composed of 2×2 matrix and has only 4 parameters to be determined. However, as the number of qubits increases, it is needed to calculate 4^n parameters and it takes long time with high complexity. The qubits decay with a certain rate which is different from each qubit. Their energy relaxations contribute the measurement operators differently and affect the estimation of quantum state. In the sense, joint qubit readout is one of methods to define the contributions of qubits in various measurement operators. Using these methods, the density matrix of three transmon qubit system is estimated.

7.1.1 Quantum State Tomography

QST is a technique to identify unknown quantum state using ensemble measurements. Quantum state is represented by density matrix and its elements are found through the measurements. In classical case, it is possible to define an unknown object by measuring the projections with various angles. On the other hand, the quantum state is only measured in z-direction, which is ground, excited, or their superposition state. It gives a part of information of quantum state. Therefore, the given initial state, such as superposition and entanglement, has to be rotated in various directions before the measurement as shown in Fig. 7.1. In this case, four pre-rotations including identity operator, $\pi/2$ rotation operators in x and y directions, and π rotation operator in x direction (I_d , $X_{\pi/2}$, $Y_{\pi/2}$, and X_{π}) are used. The readout of each resulted state in z direction enables us to find the density matrix of given state. Detailed process of QST used in this work follows Ref. [154].

To find the quantum state of n -qubit system, 4^n elements are needed to be determined by independent measurements. However, it cannot satisfy the basic properties of density matrix such as Hermiticity and non-negative eigenvalues with this analytic method. Maximum likelihood estimation (MLE) is used to avoid this problem and satisfy the conditions of density matrix by giving a certain form of density of matrix. The unknown state can be reproduced by the closest measured values. For example, the density matrix can be defined as

$$\rho(t) = T^\dagger(t)T(t) / \text{Tr}\{T^\dagger(t)T(t)\}. \quad (7.1)$$

where the matrix T in the two-qubit system is

$$T(t) = \begin{pmatrix} t_1 & 0 & 0 & 0 \\ t_5 + it_6 & t_2 & 0 & 0 \\ t_{11} + it_{12} & t_7 + it_8 & t_3 & 0 \\ t_{15} + it_{16} & t_{13} + it_{14} & t_9 + it_{10} & t_4 \end{pmatrix}. \quad (7.2)$$

It can be easily demonstrated that the condition of Hermiticity and non-negative eigenvalues are satisfied from the definition of the density matrix.

$$\begin{aligned} (T^\dagger T)^\dagger &= T^\dagger (T^\dagger)^\dagger = T^\dagger T \text{ and} \\ \langle \psi | T^\dagger T | \psi \rangle &= \langle \psi' | \psi' \rangle \geq 0. \end{aligned} \quad (7.3)$$

Then, the density matrix can be determined by finding the variables of t_1, t_2, \dots and t_{16} where the differences between the measured and expected values are minimized through $4^n - 1$ measurements.

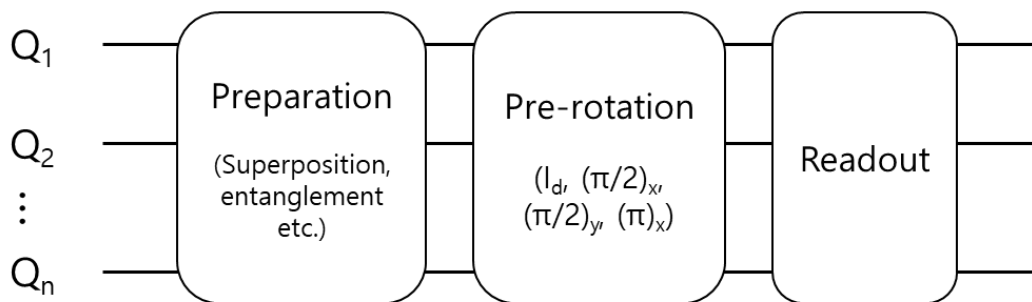


Figure 7.1 Quantum state tomography. It consists of three steps: preparation – pre-rotation – readout. Because the quantum state can be measured only in z direction, the pre-rotation process is necessary.

7.1.2 Joint Readout

Unlike the single qubit measurement, the readout of two or more qubit states is interrupted by correlations between qubits. Therefore, ‘joint qubit readout’ method [155], [156] is introduced to obtain the information of two qubit state by only single measurement. When the time for measuring the qubit state is much shorter than the relaxation time of the qubit, the information of $|00\rangle$ state can be measured, and the measurement operator is written by

$$M \propto |00\rangle\langle 00| = (II + ZI + IZ + ZZ) / 4 \quad (7.4)$$

where I is represented by identity operator and Z by Pauli matrix σ_z . However, the qubit decays with a certain rate and the populations at higher energy level (or excited state) goes to lower levels (or ground state). Then, the information of $|00\rangle$ state is for not only the real ground state but also the decayed populations. Therefore, the measurement operator can be expressed in general form

$$M = \beta_{II}II + \beta_{ZI}ZI + \beta_{IZ}IZ + \beta_{ZZ}ZZ \quad (7.5)$$

The β parameters (β_{II} , β_{ZI} , β_{IZ} , and β_{ZZ}) can be found from the measurement of simultaneous Rabi oscillations of each qubit. The time evolution of Rabi oscillation follows

$$\langle Z \rangle(t) = \frac{\gamma_1 \gamma_2}{\gamma_1 \gamma_2 + \Omega^2} + \frac{e^{-t/\tau_R} \Omega^2}{\gamma_1 \gamma_2 + \Omega^2} \left(\cos(\tilde{\Omega}t) + \frac{\sin(\tilde{\Omega}t)}{\tau_R \tilde{\Omega}} \right) \quad (7.6)$$

where γ_1 is the relaxation rate ($1/T_1$), $\gamma_2 = \gamma_1 / 2 + \gamma_\phi$ the dephasing rate, $\tau_R = 2/(\gamma_1 + \gamma_2)$ the Rabi decay time, Ω the oscillation rate, and $\tilde{\Omega} = \sqrt{\Omega^2 - (1/\tau_R)^2}$ the effective Rabi oscillation rate. By applying Eq. (7.6) to the measurement operator Eq. (7.5) and fitting the oscillations, the β parameters are obtained. In the same way, the joint qubit readout is applied for the larger size of the system.

7.1.3 Experimental Realization with Three Qubits

The quantum state of three transmon qubit in 3D cavity is determined by using the QST. The experimental scheme of transmon qubit is depicted in Fig. 7.2(a). Three transmon qubits were located in 3D aluminum cavity and separated with equal spacing. All microwaves were injected through an input port and the transmission signals were detected by using vector network analyzer (VNA). Fig. 7.2(b) shows the relaxation time of qubits used in the experiments. The relaxation time (T_1) implies how fast the qubit decays and it can be measured by varying the time interval between π pulse and readout pulse. In this case, the variation in the ground state population was measured and the ground state frequency was 7.5612 GHz. Table 7.1 summarizes the qubit parameters such as transition frequencies and T_1 .

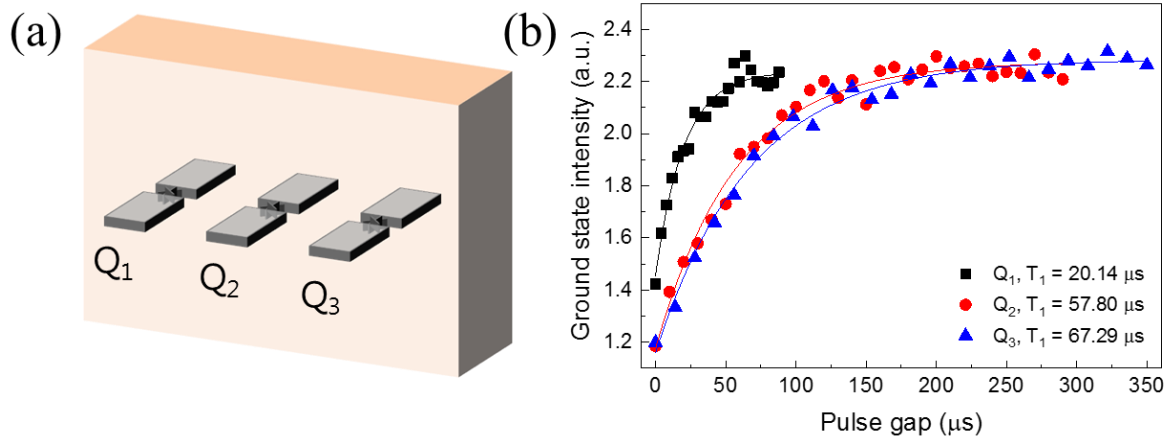


Figure 7.2 Characterization of three superconducting transmon qubits in a 3D cavity. (a) Schematic of the experimental system and (b) T_1 decay measurement of each qubit.

Table 7.1 Qubit parameters used for three qubit state tomography.

	Q ₁	Q ₂	Q ₃
$\omega_{01}/2\pi$ (GHz)	4.5809	5.3232	5.7790
T_1 (μ s)	20.14	57.80	67.29

Prior to the QST, the joint qubit readout was conducted. The ground state intensity is measured during the Rabi oscillation for each qubit first as shown in Fig. 7.3(a). In order to distinguish each qubit information, the oscillation periods are set to be different. The Rabi oscillation was conducted by increasing the pulse width to drive qubit, from 0 s to 5 μ s with an interval of 50 ns. The readout pulse width and whole pulse period were 50 μ s and 350 μ s, respectively. Then, the Rabi measurement was repeated by driving two and three qubits simultaneously. The measured values showed the combinations of Rabi oscillations of each qubit as shown in Fig. 7.3(b) and (c). Based on the qubit information obtained from the single- and two-tone Rabi oscillations, three tone Rabi oscillation could be estimated by adjusting Eq. (7.5) and (7.6) to three qubit system. Then, the β parameters are found by fitting the measured values and they are listed in Table. 7.2.

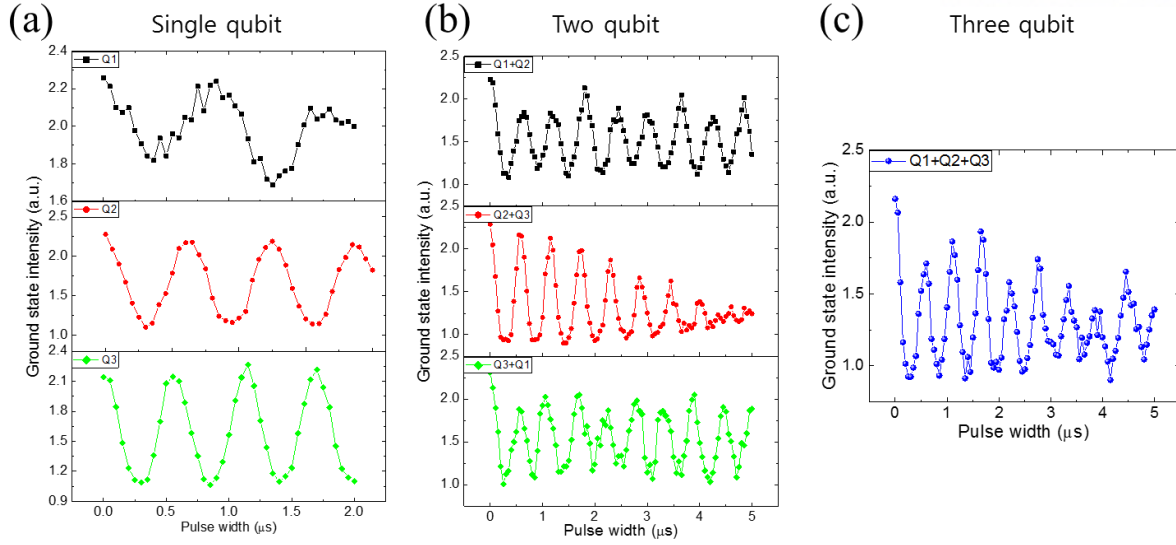


Figure 7.3 Joint readout results through simultaneous Rabi oscillations for (a) single, (b) two, and (c) three qubits.

Table 7.2 β parameters estimated from three tone Rabi oscillation.

β_{III}	β_{ZII}	β_{IZI}	β_{IIZ}	β_{ZZI}	β_{ZIZ}	β_{IZZ}	β_{ZZZ}
1.2646	0.0607	0.2597	0.2559	0.0691	0.0514	0.1802	0.0687

Single qubit operations of rotation in X- and Y-axis are implemented by using I/Q mode of vector signal generator E8267C. I port is considered to be X-axis and Q port to be Y-axis. The cosine pulse generated by arbitrary waveform generator (AWG) is mixed through pulse mode of the vector signal generator. The I/Q signal is injected with a readout pulse through a directional coupler. When the pulse shape is formed, there can be a certain amount of offset which induces low fidelity of the single qubit operation. Therefore, the offset was calibrated by adjusting the ‘offset’ function in the AWG. The offset voltage can be controlled with the order of 0.1 mV. The calibrated pulse was confirmed by measuring the π pulse width in 4 different ways, $\pm I$ and $\pm Q$. Then, to set the exact π pulse with a given gate time, ‘error amplification’ [157] is implemented. When the operation of $\pi/2$ pulse is repeated, the measured ground state intensity should be same as 0.5 in the normalized scale. However, when there is an error in the gate, the error is added and amplified as the operation is repeated. In this process, the microwave power is tuned to drive the qubit for calibrating the pulse.

Then, the QST in three transmon qubit system is conducted. In this experiment, the prepared states were the superposition state after $X_{\pi/2}$ rotation to each qubit. Pre-rotations for both positive and negative directions were conducted with 63 times, totally 126 pre-rotations. Since three qubit system is represented as 8×8 matrix, the 64 parameters are estimated. The experimental results of $X_{\pi/2}$ rotation to Q_1 , Q_2 , and Q_3 are shown in Fig. 7.4(a), (b), and (c) with the fidelities of 0.67, 0.76, and 0.60, respectively. Here, the source files to generate pulse sequence in these experiments are made by using Mathematica 6.0 [158].

7.1.4 Conclusion

The QST is implemented on three transmon qubit in 3D cavity. In the process of QST, joint qubit readout method is used and the β parameters are defined by fitting three tone Rabi oscillation. Three qubit system consists of 8×8 density matrix with 64 parameters to be determined. Due to the condition that trace of the density matrix is equal to 1, 126 different pre-rotations are conducted with two opposite signs. As the number of qubits increases, the number of elements to be solved and accordingly, the number of pre-rotations also increases. The increased pre-rotations make the longer time to take the results of joint readout and it can affect the final result of QST. Therefore, it is necessary to improve the single qubit operation with high gate fidelity.

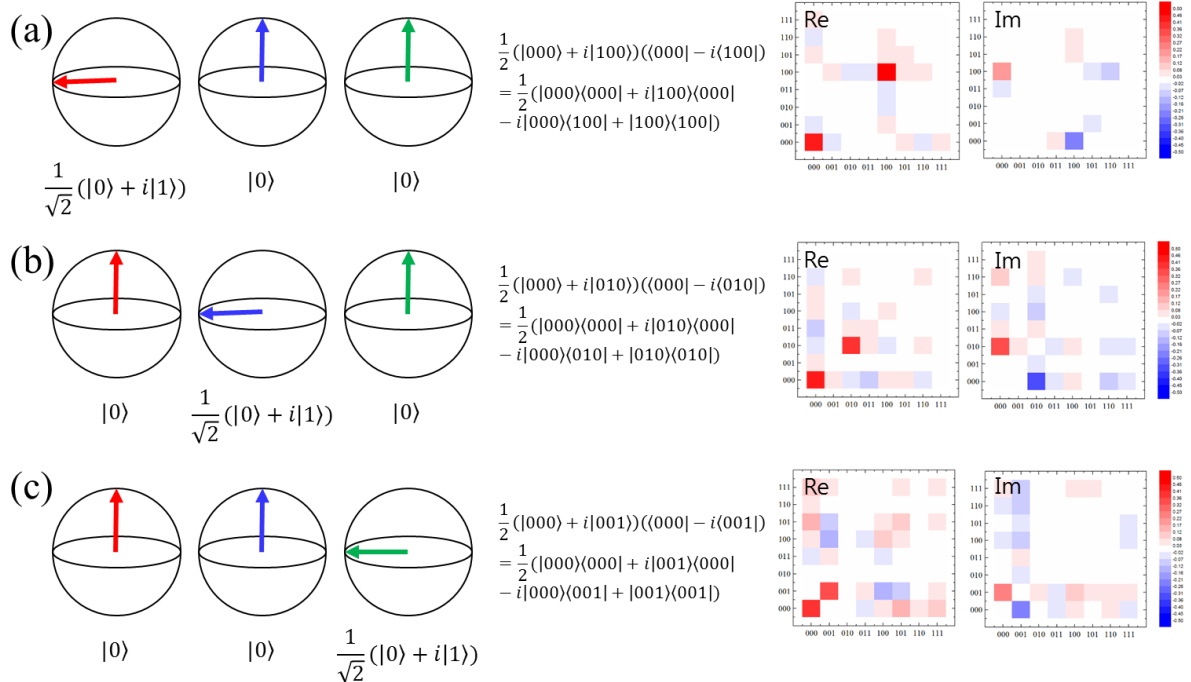


Figure 7.4 Experimental results of three-qubit QST in case of $X_{\pi/2}$ rotations for (a) Q_1 , (b) Q_2 , and (c) Q_3 .

7.2 Phase Compensation via Z-axis Phase Gate

In previous section, the method to measure the quantum state in multiple qubit system is discussed. Now, gate operations in two qubit system in respect with phase compensation are described. It is a part of the previous experimental results of two qubit entanglement by using microwave activated phase (MAP) gate and Z gate [159]. This section covers the review of the MAP gate and Z gate with hyperbolic secant pulse in order. Finally, the control of phase accumulated during the MAP gate by using Z gate in two qubit system is shown.

7.2.1 Microwave Activated Phase Gate

In 2013, the MAP gate was first demonstrated experimentally by J. M. Chow *et al.* [160]. Two transmon qubits are designed to be align their non-computational states, $|12\rangle$ and $|03\rangle$. The energy level diagram of two qubit system is depicted in Fig. 7.5(a). The notation of $|nm\rangle$ implies excitations of qubits, n for Q_1 (red) and m for Q_2 (blue). Qubit-qubit interaction makes these level split by δ , resulting the non-degeneracy in $|1\rangle \leftrightarrow |2\rangle$ transition energy in Q_2 depending on Q_1 state. The transition energy between $|01\rangle$ and $|02\rangle$ is denoted as ε and that between $|11\rangle$ and $|12\rangle$ as ε' . When an external microwave tone near $|1\rangle \leftrightarrow |2\rangle$ transition frequency is applied, the computational levels of $|01\rangle$ and $|11\rangle$ are shifted by ac Stark effect. The amount of energy shift is differed from each other, $\delta\varepsilon \neq \delta\varepsilon'$. In this scheme, the Ramsey oscillation rates are not same in $|00\rangle \leftrightarrow |01\rangle$ and $|10\rangle \leftrightarrow |11\rangle$ with driving frequency of ω_{01} (Q_2). Then, when the superposition state of Q_2 is prepared, the bell state of $\frac{1}{\sqrt{2}}(|00\rangle + |11\rangle)$ can be achieved after a certain time, or MAP gate time t_g when two Ramsey oscillations are out of phase. The pulse sequence of two qubit entanglement by using MAP gate is illustrated in Fig. 7.5(b) and the detailed descriptions are found in [159], [160].

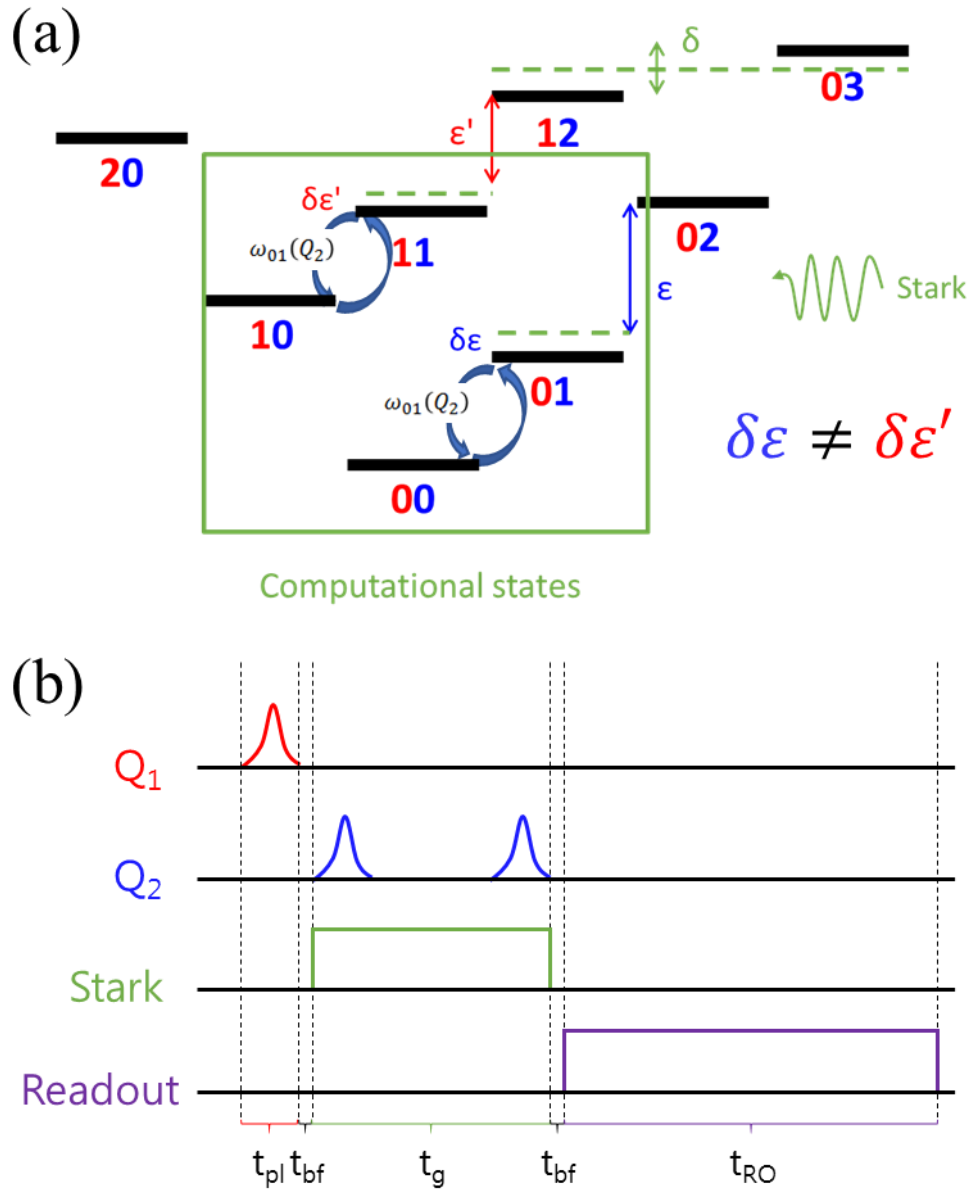


Figure 7.5 (a) Energy diagram of two qubit system during the MAP gate. $|nm\rangle$ denotes excitations of qubits, n for Q1 (red) and m for Q2 (blue). (b) Pulse sequence of the MAP gate. The pulses for Q1 and Q2 are cosine-shaped, resulting the $\pi/2$ rotations. An additional microwave tone inducing ac Stark effect is applied during the Ramsey oscillation of Q2.

7.2.2 Hyperbolic Secant Pulse for Z-axis Phase Gate

Applying the MAP gate makes unwanted phase accumulated during the operation. The phase should be cancelled by another operation to realize controlled-NOT (cNOT) gate with high fidelity. The Z-axis phase gate plays a role to make a phase as shown in Fig. 7.6. The demonstration of Z-axis phase gate is conducted by making a superposition state and applying the Z gate. In this experiment, the Z-axis phase gate with hyperbolic secant (sech) pulse is used.

The Z-axis phase gate with hyperbolic secant pulse as shown in Fig. 7.7 was reported experimentally first by H. S. Ku *et al.* in 2017 [161]. The sech pulse shows Rabi oscillations with equal periods regardless of the detuning $\Delta = \omega_D - \omega_{01}$ unlike other shaped pulses as shown in Fig. 7.8. This means that the final state is same with the initial state after a 2π cyclic evolution, but with a phase depending on the detuning Δ . Here, the phase ϕ after the Z gate has a relation with detuning Δ of $\phi = 4\arctan(\Delta/\rho)$ where ρ is a bandwidth where $\sigma = \pi/(2\rho)$.

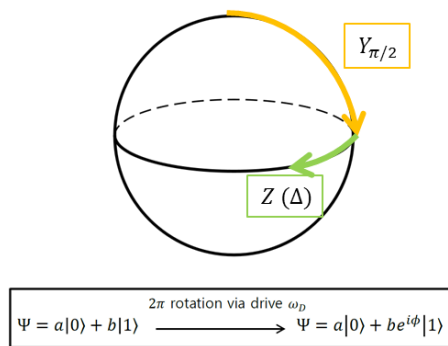


Figure 7.6 Operation of Z-axis phase gate. To characterize the gate, superposition state should be prepared by applying $Y_{\pi/2}$ pulse.

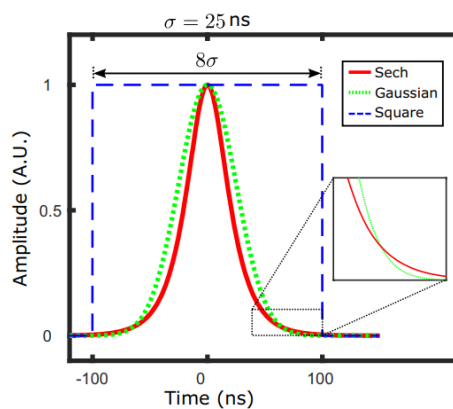


Figure 7.7 Pulse shapes for three different pulses; solid red for sech pulse, dotted green for Gaussian pulse, and dashed blue for square pulse [161].

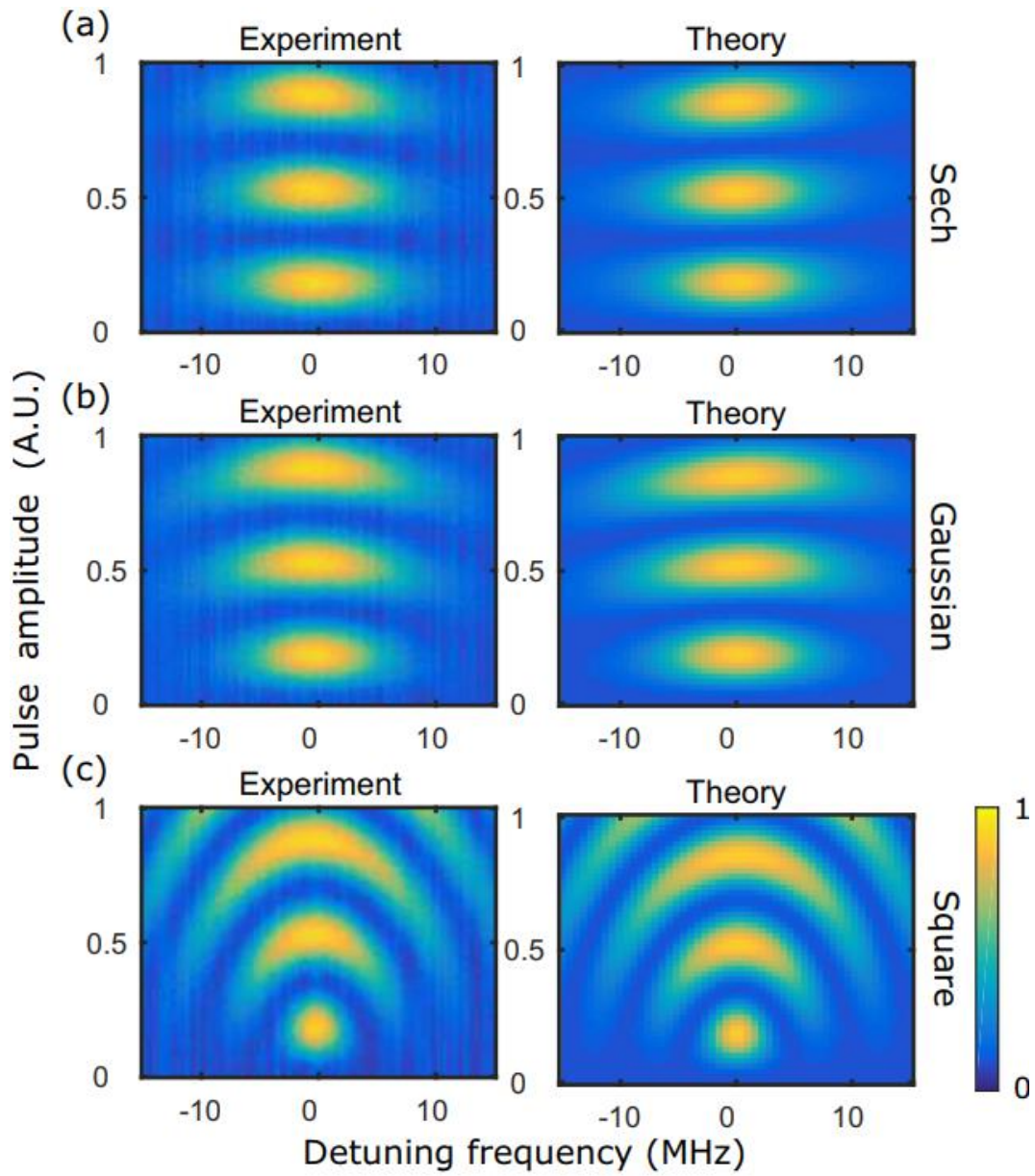


Figure 7.8 Experimental (left) and theoretical (right) Rabi oscillation map as a function of detuning frequency of $\Delta = \omega_D - \omega_{10}$ for different pulse shapes; (a) sech, (b) Gaussian, and (c) square pulses [161].

7.2.3 Experimental Result in Two Qubit System

After the MAP gate, the phase is accumulated by $\frac{1}{\sqrt{2}}(|00\rangle + e^{i\phi}|01\rangle)$ for the initial state of $\frac{1}{\sqrt{2}}(|00\rangle + |01\rangle)$. The additional phase can be compensated by applying Z-axis phase gate. In this case, hyperbolic secant pulse is used as a Z gate. The experimental scheme is shown in Fig. 7.9(a). The system consists of two qubits, one having fixed transition frequency and the other with tunable transition frequency. For the later one, the qubit is fabricated by using SQUID and the Josephson inductance is varied by an external magnetic field of coil. Also, the relaxation time T_1 of both qubits is shown in Fig. 7.9(b) and the qubit parameters are listed in Table 7.3.

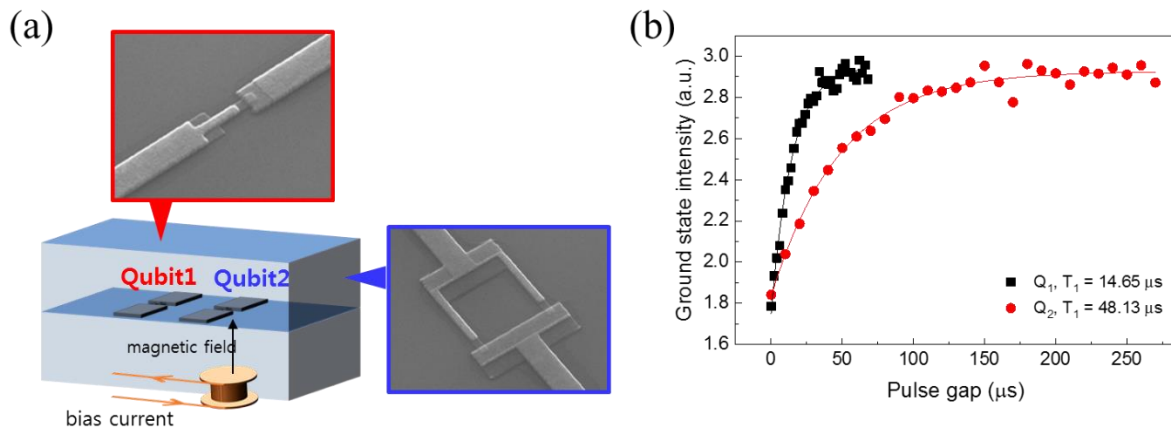


Figure 7.9 Characterization of two superconducting transmon qubits in a 3D cavity. (a) Schematic of the experimental system and (b) T_1 decay measurement of each qubit.

Table 7.3 Qubit parameters used for phase compensation in two qubit system.

	Q ₁	Q ₂
$\omega_{01}/2\pi$ (GHz)	6.1400	5.4023
T_1 (μs)	14.65	48.13

The Z-axis phase gate is calibrated and estimated by the following sequence. First, the superposition state is prepared by rotating the ground state by $\pi/2$ along the Y-axis. Then, the hyperbolic secant pulse is applied to rotate 2π with the microwave detuned from $\omega_{01}/2\pi$. The rotated angle is estimated from the measured values with single-qubit QST. The same process is repeated for Q_1 and Q_2 with different gate time. The experimental results of Z gate for qubit Q_1 and Q_2 are shown in Fig. 7.10(a) and (b), respectively. The polar angle θ gives constant value for all cases, on the other hand, the azimuthal angle ϕ shows variation with respect to the detuning Δ .

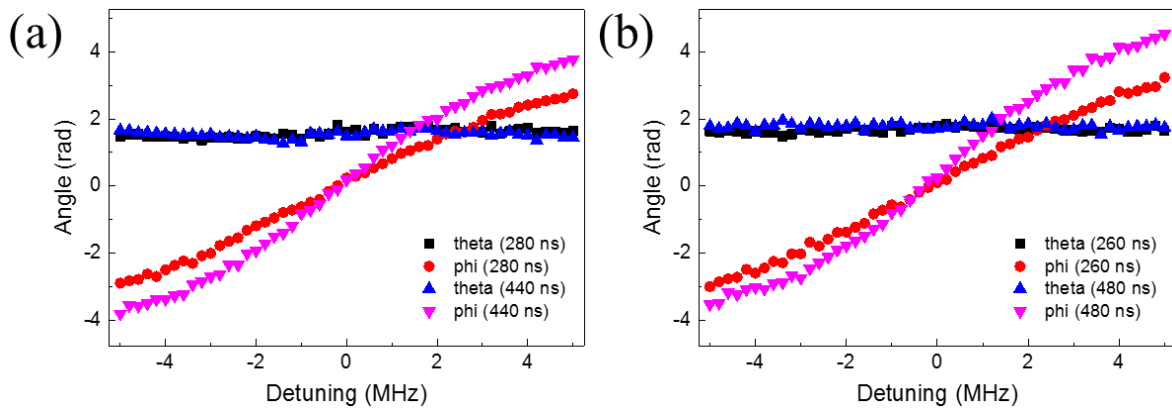


Figure 7.10 Phase estimation for z-axis phase gate by using hyperbolic secant shaped pulse. The Z-axis phase gate is realized with qubit (a) Q_1 for gate time of 280 ns and 440 ns and (b) Q_2 for gate time of 260 ns and 480 ns.

The phase compensation is examined by using hyperbolic secant pulse as Z-axis phase gate. As mentioned before, the phase is accumulated during the MAP gate. This additional phase can give undesired state and make lower gate fidelity. With the Z-axis phase gate time of 260 ns for Q_2 , the phase rotation in Q_2 is found by two qubit QST. First, we observe that the ground state intensity is changed with respect to the detuning Δ as shown in Fig. 7.11(a). At the detuning frequency to minimize the value after $Y_{\pi/2} \otimes Y_{\pi/2}$ pre-pulse, or $\Delta = +1.2$ MHz, the fidelity is improved from 0.75 to 0.81 compared to the original state as shown in Fig. 7.11(b) and (c). The quantum state with opposite sign on $|1\rangle$ at $\Delta = -3.0$ MHz is implemented with the fidelity of 0.77 as shown in Fig. 7.11(d).

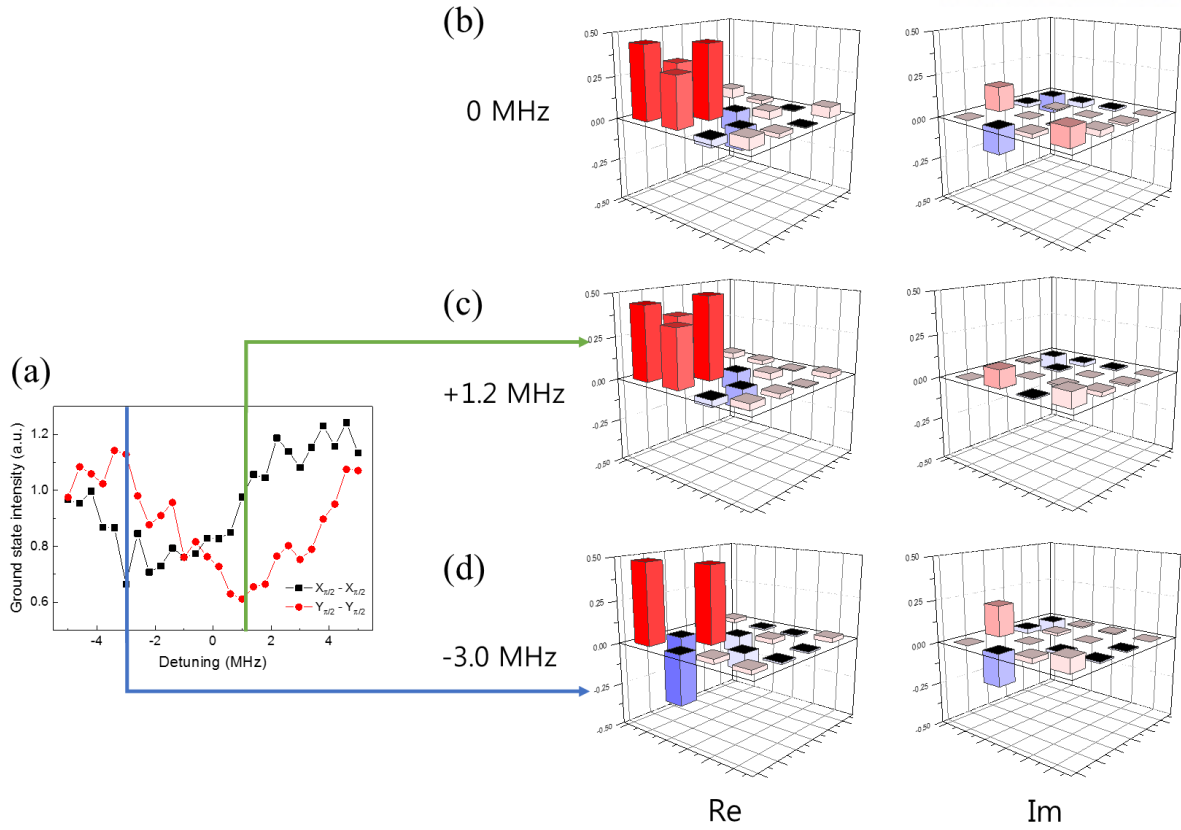


Figure 7.11 Phase compensation via Z-axis phase gate. (a) Applying protocols for Q_2 of two different pre-pulses, $X_{\pi/2} \otimes X_{\pi/2}$ and $Y_{\pi/2} \otimes Y_{\pi/2}$. Density matrix is reconstructed (b) right after MAP gate with Q_1 in the ground state, (c) when $\Delta = +1.2$ MHz, and (d) when $\Delta = -3.0$ MHz.

7.2.4 Conclusion

The phase compensation in two superconducting transmon qubits located in a three-dimensional copper cavity is realized experimentally. The phase is accumulated in the process of realizing MAP gate. With hyperbolic secant shaped pulse as a Z-axis phase gate, it is possible to make the phase cancellation. This method might have an advantage of the number of pulse and gate time. Two qubit QST is performed to show the effect of the Z-axis phase gate on two qubit system. The next step will be to make an entanglement in three qubit system by using these processes with MAP gate and Z gate.

Chapter 8 . Conclusion and Outlook

The aim of this dissertation is to show multi-level capacitive memory effect by fabricating metal/oxide/floating-Schottky junction and superconducting circuit quantum electrodynamics (QED) where the device can be applied. Prior to demonstration of the memcapacitive device, the electrical behaviors of Schottky junction is shown in case that different interfacial layers are inserted between metal and semiconductor. Aluminum oxide and graphene are chosen for an interfacial layer and their thicknesses are to be less than 5 nm to minimize the effect of physical separation. For the junction structured with Au/Ni/Al₂O₃/4H-SiC, spontaneous polarization (SP) charge on surface of 4H-SiC was observed by separating a distance with Al₂O₃ thin layer between the metal and substrate. Its effect was revealed by an increase in Schottky barrier height (SBH) due to the negative SP charges [86]. Based on the measured SBH, the SP charge was estimated to be $\sim 3.0 \times 10^{-2} \text{ C/m}^2$ which is close to previously measured values.

Unlike the insulating layer of Al₂O₃, graphene is semi-metal with non-zero band gap and has a certain amount of charge itself. When the graphene was used as an interfacial layer [71], charge transfer occurs first due to the difference in work functions of graphene and semiconductor. Dipole charge between metal and graphene was also considered, which is formed by an existence of vacuum gap between them. By using the 4H-SiC substrate having weak Fermi level pinning effect, these additional charge effects were revealed to decrease the SBH in Au/Gr/4H-SiC junction. The SBHs were measured by using three different ways of current-voltage (I-V), capacitance-voltage (C-V), and internal photoemission (IPE) methods. Although each measurement covered different electrical behaviors of the junction, the reduction of SBH by the graphene was confirmed commonly.

Based on studies of the Schottky junction [86], [162], the device structured with Au/Cr/Al₂O₃/Al/Si could function as a memcapacitor [127]. The memcapacitive device works based on a variation of depletion width by change of net charge in floating metal of the device. The suggested device showed multi-level capacitance values depending on the magnitudes of voltage pulses, indicating the capacitive memory effect. Also, the C-V hysteresis loop as an indication of memory effect was observed.

Moreover, superconducting circuit QED system where the memcapacitor can be applied was discussed. First topic is Josephson parametric amplifier (JPA) which can amplify an input signal, operating in quantum-limited regime. There are two kinds of superconducting parametric amplifiers that were used in this dissertation, such as the JPA and Josephson parametric converter (JPC). They showed signal amplification with the gain of $\sim 10 \text{ dB}$ and $\sim 20 \text{ dB}$, respectively. They were used in readout of superconducting qubit to improve measurement efficiency. Furthermore, when the JPA operates as a phase-sensitive amplifier, it can generate squeezed state. For this purpose, the JPA was

used as a squeezer and the JPC as an amplifier in order. The squeezed state was observed by using homodyne measurement and reconstructed by using Wigner tomography.

We also studied the measurement of quantum state of superconducting qubits in the circuit QED system. Quantum state tomography (QST) is a method to estimate the quantum state as a density matrix, consisting of state preparation, pre-rotations, and joint qubit readout. We discussed the basic steps of QST in multi-qubit system and showed the experimental result of $\pi/2$ rotations along x-axis with three transmon qubits located in 3D cavity. Furthermore, in two transmon qubit system, phase compensation by using hyperbolic secant pulse was presented.

Although we presented the device having multilevel capacitive memory, many issues to apply the circuit QED are remained. In order to apply the memcapacitor to the superconducting circuit QED, one should design the memcapacitor having appropriate capacitance to work as a microwave resonator. Also, the memcapacitive behaviors at low temperature should be discussed.

In the superconducting circuit system, it is still in progress to develop and operate own JPA. The next step is to repeat the generation of squeezed state by using the JPA and to make broadband JPA with high gain. In addition, as the number of qubits increases, each process of QST become complex, requiring more operations and more parameters to be calculated. Therefore, the single qubit gate fidelity should be improved further in advance to the multiple qubit operations. The use of JPA is one possible method to enhance the measurement of qubits and thus, the gate fidelities.

Appendix A. Recipes

Fabrication of superconducting resonator

This section covers the fabrication process for niobium (Nb) resonator except the deposition of metals, such as Nb and Al/AlO_x/Al junction. One of the superconducting resonator samples is shown in Fig. 4.8(a).

Wafer cleaning

- Sonicate in Acetone for 5 min
- Sonicate in IPA for 5 min
- Blow dry with N₂
- Dehydrate on a hot plate at 115 °C for 1 min
- Cool down for 1 min

Patterning and etching process for Nb resonator

- Spin photoresist S1813 at 4000 rpm for 45 sec
- Soft-bake on a hot plate at 115 °C for 1 min
- Cool down for 1 min
- Expose UV light with intensity of 14.0 mW/cm² under align gap of 50 μm
- Develop using AZ 300 MIF for 2 min
- Rinse with DI water for 40 sec
- Blow dry with N₂
- Etch Nb using SF₆
- Remove PR sonicating in Acetone for 5 min
- Sonicate in IPA for 3 min
- Blow dry with N₂
- Dehydrate on a hot plate at 115 °C for 1 min

Dicing into 8 mm × 8 mm chips

- Spin photoresist S1813 at 4000 rpm for 45 sec to protect the surface
- Soft-bake on a hot plate at 115 °C for 1 min
- Dice the wafer into square pieces (8 mm × 8 mm)

Patterning of SQUIDs

- Remove PR sonicating in Acetone for 5 min
- Sonicate in IPA for 3 min
- Blow dry with N₂
- Dehydrate on a hot plate at 115 °C for 1 min
- Spin LOR 10B at 3000 rpm for 45 sec
- Bake on a hot plate at 180 °C for 5 min
- Cool down for 1 min
- Spin PMMA C4 at 3000 rpm for 45 sec
- Bake on a hot plate at 180 °C for 1 min 30 sec
- Cool down for 1 min
- Expose with 50 pA with a dose 250 μC/mm²
- Develop top layer using MIBK:IPA (1:3) for 40 sec
- Rinse in IPA
- Blow dry with N₂
- Develop bottom layer using MF320:DI (1:5) for 30 sec
- Rinse in IPA
- Blow dry with N₂
- Evaporate Al (80 nm)/AlO_x/Al (80 nm) junction
- Lift-off in PG Remover at 50 °C for 12 hours
- Rinse in IPA
- Blow dry with N₂

Dicing into 2 mm × 4 mm chips

- Spin photoresist S1813 at 4000 rpm for 40 sec to protect the surface
- Soft-bake on a hot plate at 90 °C for 1 min
- Dice the wafer into rectangular pieces (2 mm × 4 mm)
- Sonicate in Acetone for 3 min
- Sonicate in IPA for 2 min
- Blow dry with N₂

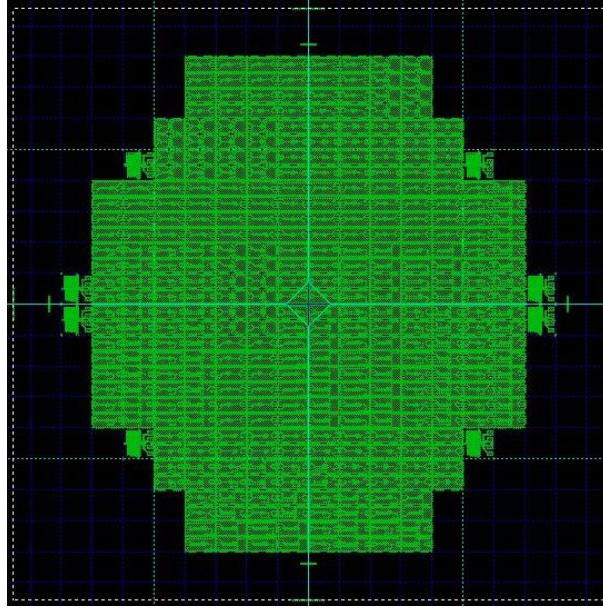


Figure A.1 Photomask design for superconducting resonator

Appendix B. JPA and JPC

The experiment of generating squeezed state is done by using JPA and JPC. The JPA samples were designed and fabricated at NIST by K. Cicak, F. Lecocq, and J. Aumentado. The JPC SN019 is purchased from Quantum Circuits, Inc. [163] and its photography of the assembly is shown in Fig. B.1. The DC coil is under the JRM. Signal and idler resonators are connected with hybrids, respectively. When one of both resonators is used, the other is terminated. The photograph of JPC mounted on the dilution fridge is shown in Fig. B.2.

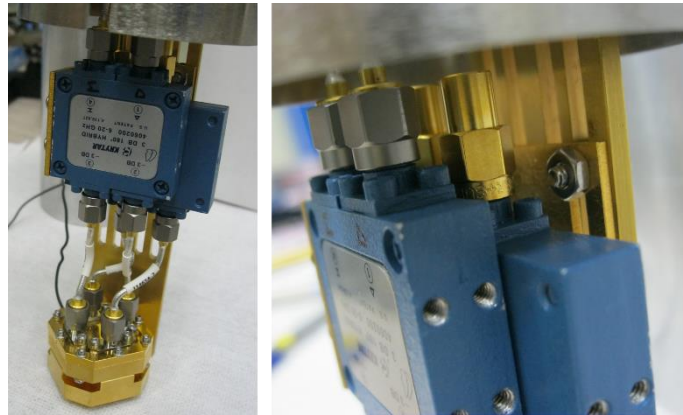


Figure B.1 Photograph of JPC SN019 to test either signal or idler mode resonator.



Figure B.2 Photograph of JPC mounted on the mixing chamber stage in dilution fridge.

Appendix C. Single Qubit Operation

Randomized Benchmarking

Randomized benchmarking (RB) [164] is a method to measure a gate fidelity by generating random sequences of gates. Test gate group consists of $\pi/2$, π , and $3\pi/2$ rotations in X- and Y-directions. By returning the final state to the ground state, the projected values are measured. Since the gate is not perfect, the ground state intensity decreases with increasing the length of random sequences. This fidelity implies an average of whole gate group. In order to determine the fidelity of specific gate, interleaved RB [165] is used. It is conducted by inserting the specific gate between every gate in previously generated random sequence. The fidelities for the reference are estimated as 0.9981 for the gate time of 55 ns and 0.9890 for the gate time of 200 ns. Also, the fidelities for $X_{\pi/2}$ gate are measured as 0.9976 and 0.9900, respectively.

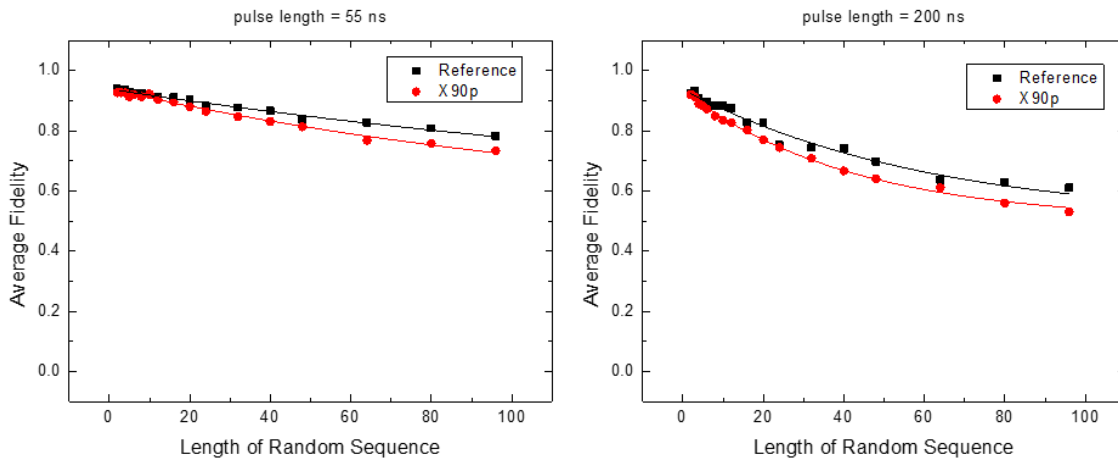


Figure C.1 Experimental results of RB for the pulse length of 55 ns and 200 ns.

Rotation in Arbitrary Axis

As discussed in section 7.1.3, the qubit operations along X- and Y-axis have been conducted by using the I/Q mode in the vector signal generator. The offset has been calibrated by setting the function in the AWG. The calibrated pulse was confirmed by plotting a part of Rabi oscillation in four different conditions as shown in Fig. C.1. The gate time was set to be 200 ns and the offset values for I and Q channels were -1.9 and -1.4 mV, respectively. Through the error amplification method, the experimental results of rotating the qubit by π in X- and Y-directions are shown in Fig. C.2.

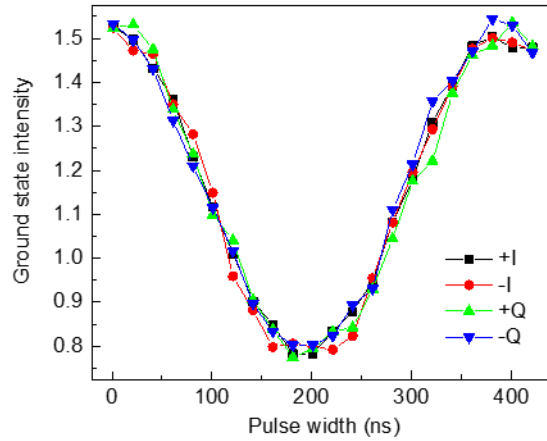


Figure C.2 Confirmation for calibrating the offset in the pulse.

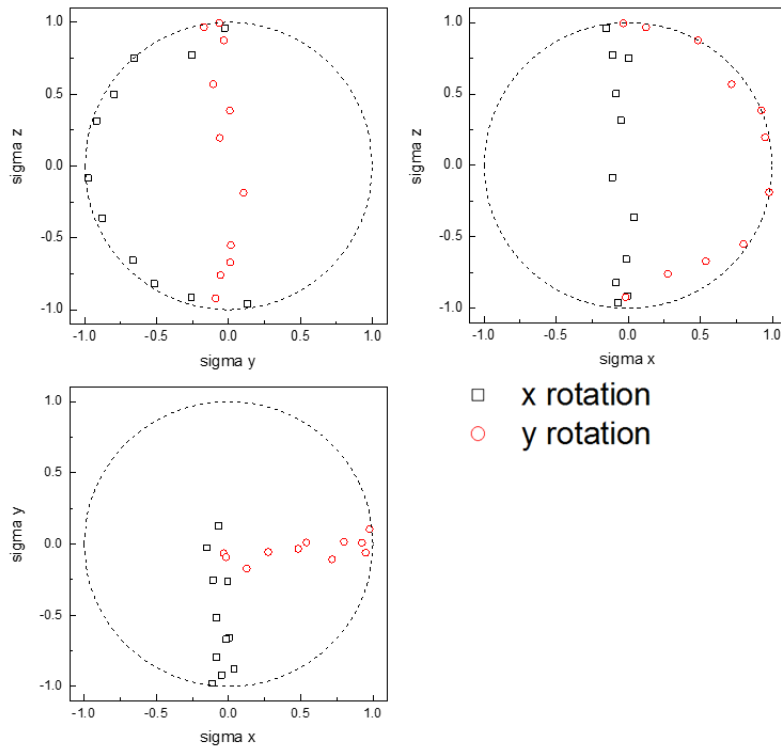


Figure C.3 Single qubit QST for tracking qubit rotation in X- and Y-directions.

Furthermore, it was demonstrated that the qubit rotated in a specific direction by controlling ratio of I and Q pulse magnitudes. Based on the magnitude of I channel, or ‘I factor’, that of Q channel is set to be $(1-I \text{ factor})^{1/2}$. The experimental results when the ratios of I to Q are 1, 0.5, 0.366, and 0 are shown in Fig. C.3. More detailed results of I factor varying from 1 to 0 with spacing of 0.1 are shown in Fig. C.4.

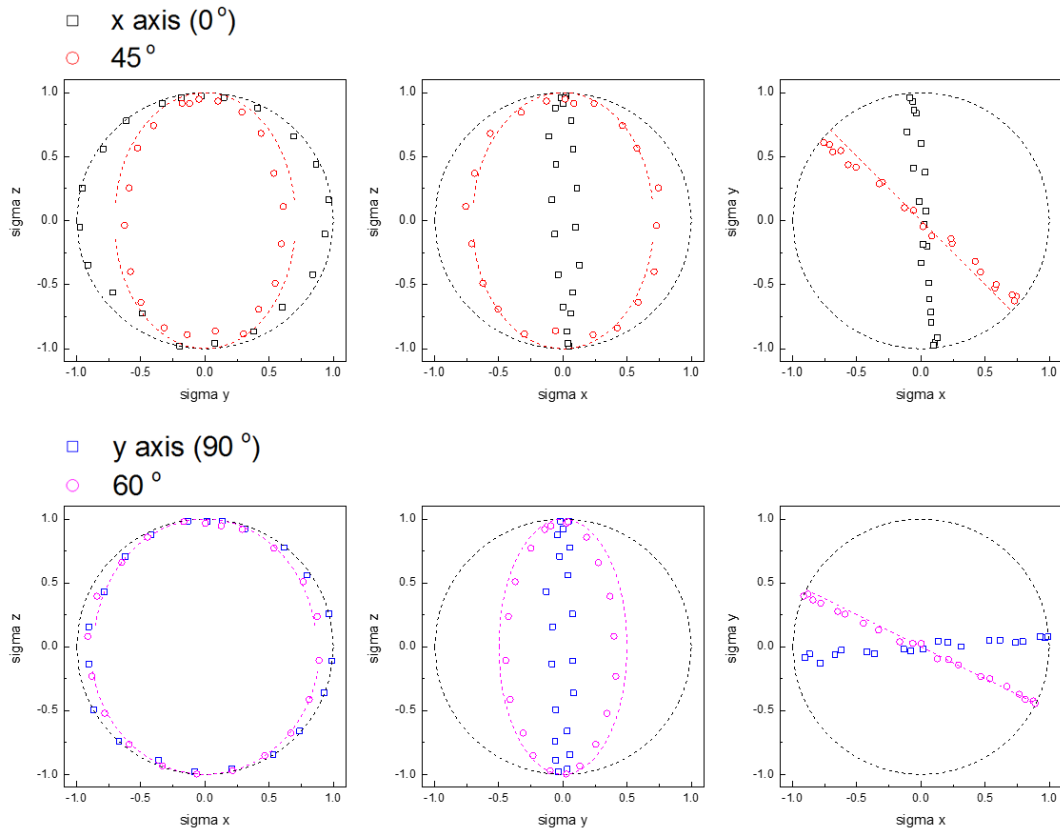


Figure C.4 Single qubit QST depending on the different rotation axis (0, 45, 60, and 90 °).

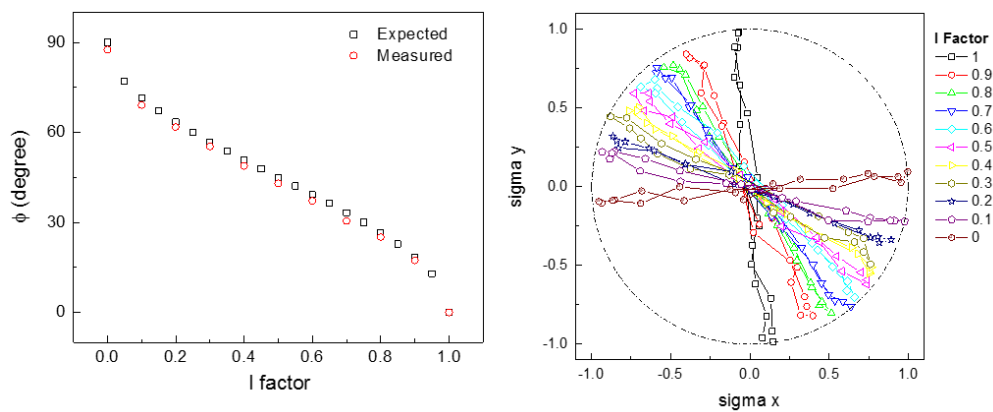


Figure C.5 Single qubit QST by varying I factor from 1 to 0 by an interval of 0.1.

References

- [1] R. P. Feynman, “Quantum mechanical computers,” *Found. Phys.*, vol. 16, no. 6, pp. 507–531, 1986.
- [2] M. Di Ventra and Y. V. Pershin, “The parallel approach,” *Nat. Phys.*, vol. 9, pp. 200–202, 2013.
- [3] D. Vion *et al.*, “Manipulating the Quantum State of an Electrical Circuit,” *Science (80-.)*, vol. 296, pp. 886–889, 2002.
- [4] J. Clarke and F. K. Wilhelm, “Superconducting quantum bits,” *Nature*, vol. 453, pp. 1031–1042, 2008.
- [5] M. H. Devoret and R. J. Schoelkopf, “Superconducting Circuits for Quantum Information: An Outlook,” *Science (80-.)*, vol. 339, pp. 1169–1175, 2013.
- [6] B. D. Josephson, “Possible New Effects in Superconductive Tunnelling,” *Phys. Lett.*, vol. 1, pp. 251–253, 1962.
- [7] M. H. Devoret, A. Wallraff, and J. M. Martinis, “Superconducting Qubits: A Short Review,” 2004.
- [8] J. M. Martinis, M. H. Devoret, and J. Clarke, “Experimental tests for the quantum behavior of a macroscopic degree of freedom: The phase difference across a Josephson junction,” *Phys. Rev. B*, vol. 35, pp. 4682–4698, 1987.
- [9] I. Buluta, S. Ashhab, and F. Nori, “Natural and artificial atoms for quantum computation,” *Reports Prog. Phys.*, vol. 74, p. 104401, 2011.
- [10] Y. Nakamura, Y. A. Pashkin, and J. S. Tsai, “Coherent control of macroscopic quantum states in a single-Cooper-pair box,” *Nature*, vol. 398, pp. 786–788, 1999.
- [11] J. M. Martinis, S. Nam, J. Aumentado, and C. Urbina, “Rabi Oscillations in a Large Josephson-Junction Qubit,” *Phys. Rev. Lett.*, vol. 89, no. 11, p. 117901, 2002.
- [12] I. Chiorescu, Y. Nakamura, C. J. P. M. Harmans, and J. E. Mooij, “Coherent Quantum Dynamics of a Superconducting Flux Qubit,” *Science (80-.)*, vol. 299, pp. 1869–1871, 2003.
- [13] F. Yoshihara, K. Harrabi, A. O. Niskanen, Y. Nakamura, and J. S. Tsai, “Decoherence of flux qubits due to $1/f$ flux noise,” *Phys. Rev. Lett.*, vol. 97, p. 167001, 2006.
- [14] J. Koch *et al.*, “Charge-insensitive qubit design derived from the Cooper pair box,” *Phys. Rev. A*, vol. 76, p. 042319, 2007.
- [15] H. Paik *et al.*, “Observation of high coherence in Josephson junction qubits measured in a three-dimensional circuit QED architecture,” *Phys. Rev. Lett.*, vol. 107, p. 240501, 2011.
- [16] A. Blais, R.-S. Huang, A. Wallraff, S. M. Girvin, and R. J. Schoelkopf, “Cavity quantum electrodynamics for superconducting electrical circuits: An architecture for quantum computation,” *Phys. Rev. A*, vol. 69, p. 062320, 2004.

- [17] S. M. Anton *et al.*, “Pure dephasing in flux qubits due to flux noise with spectral density scaling as $1/f\alpha$,” *Phys. Rev. B*, vol. 85, p. 224505, 2012.
- [18] P. Kumar *et al.*, “Origin and Reduction of $1/f$ Magnetic Flux Noise in Superconducting Devices,” *Phys. Rev. Appl.*, vol. 6, p. 041001, 2016.
- [19] M. B. Weissman, “ $1/f$ noise and other slow, nonexponential kinetics in condensed matter,” *Rev. Mod. Phys.*, vol. 60, pp. 537–571, 1988.
- [20] J. Sok, J. S. Lee, and E. H. Lee, “Tunability of Resonant Frequencies in a Superconducting Microwave Resonator by Using SrTiO₃ Ferroelectric Films,” *J. Korean Phys. Soc.*, vol. 32, no. 1, pp. 158–161, 1997.
- [21] W. E. Purches *et al.*, “A planar Al-Si Schottky barrier metal-oxide-semiconductor field effect transistor operated at cryogenic temperatures,” *Appl. Phys. Lett.*, vol. 107, p. 063503, 2015.
- [22] C. M. Caves, “Quantum limits on noise in linear amplifiers,” *Phys. Rev. D*, vol. 26, no. 8, pp. 1817–1839, 1982.
- [23] T. Yamamoto *et al.*, “Flux-driven Josephson parametric amplifier,” *Appl. Phys. Lett.*, vol. 93, p. 042510, 2008.
- [24] J. Y. Mutus *et al.*, “Design and characterization of a lumped element single-ended superconducting microwave parametric amplifier with on-chip flux bias line,” *Appl. Phys. Lett.*, vol. 103, p. 122602, 2013.
- [25] X. Zhou *et al.*, “High-gain weakly nonlinear flux-modulated Josephson parametric amplifier using a SQUID array,” *Phys. Rev. B*, vol. 89, p. 214517, 2014.
- [26] B. Abdo, F. Schackert, M. Hatridge, C. Rigetti, and M. Devoret, “Josephson amplifier for qubit readout,” *Appl. Phys. Lett.*, vol. 99, p. 162506, 2011.
- [27] P. Krantz *et al.*, “Single-shot read-out of a superconducting qubit using a Josephson parametric oscillator,” *Nat. Commun.*, vol. 7, no. 11417, pp. 1–8, 2016.
- [28] Z. R. Lin *et al.*, “Single-shot readout of a superconducting flux qubit with a flux-driven Josephson parametric amplifier,” *Appl. Phys. Lett.*, vol. 103, p. 132602, 2013.
- [29] B. Yurke *et al.*, “Observation of parametric amplification and deamplification in a Josephson parametric amplifier,” *Phys. Rev. A*, vol. 39, no. 5, pp. 2519–2533, 1989.
- [30] M. A. Castellanos-Beltran, K. D. Irwin, G. C. Hilton, L. R. Vale, and K. W. Lehnert, “Amplification and squeezing of quantum noise with a tunable Josephson metamaterial,” *Nat. Phys.*, vol. 4, pp. 928–931, 2008.
- [31] L. Zhong *et al.*, “Squeezing with a flux-driven Josephson parametric amplifier,” *New J. Phys.*, vol. 15, p. 125013, 2013.
- [32] H. J. Carmichael, A. S. Lane, and D. F. Walls, “Resonance Fluorescence from an Atom in a Squeezed Vacuum,” *Phys. Rev. Lett.*, vol. 58, no. 24, pp. 2539–2542, 1987.
- [33] O. Astafiev *et al.*, “Resonance Fluorescence of a Single Artificial Atom,” *Science (80-.)*, vol.

- 327, pp. 840–843, 2010.
- [34] D. M. Toyli *et al.*, “Resonance fluorescence from an artificial atom in squeezed vacuum,” *Phys. Rev. X*, vol. 6, no. 031004, pp. 1–13, 2016.
- [35] J. Bardeen, L. N. Cooper, and J. R. Schrieffer, “Theory of Superconductivity,” *Phys. Rev. B*, vol. 108, pp. 1175–1204, 1957.
- [36] J. Bardeen, L. N. Cooper, and J. R. Schrieffer, “Microscopic theory of superconductivity,” *Phys. Rev.*, vol. 106, no. 1, pp. 162–164, 1957.
- [37] M. Tinkham, *Introduction to Superconductivity*. Courier Corporation, 2012.
- [38] J. Clarke and A. I. Braginski, *The SQUID Handbook*. Wiley Online Library, 2006.
- [39] M. A. Nielsen and I. L. Chuang, *Quantum Computation and Quantum Information*. Cambridge University Press, 2004.
- [40] H. Mabuchi and A. C. Doherty, “Cavity quantum electrodynamics: Coherence in context,” *Science (80-.)*, vol. 298, pp. 1372–1377, 2002.
- [41] H. Walther, B. T. H. Varcoe, B. G. Englert, and T. Becker, “Cavity quantum electrodynamics,” *Reports Prog. Phys.*, vol. 69, pp. 1325–1382, 2006.
- [42] I. Chiorescu, P. Bertet, K. Semba, Y. Nakamura, C. J. P. M. Harmans, and J. E. Mooij, “Coherent dynamics of a flux qubit coupled to a harmonic oscillator,” *Nature*, vol. 431, pp. 159–162, 2004.
- [43] A. Wallraff *et al.*, “Strong coupling of a single photon to a superconducting qubit using circuit quantum electrodynamics,” *Nature*, vol. 431, pp. 162–167, 2004.
- [44] A. Wallraff *et al.*, “Approaching unit visibility for control of a superconducting qubit with dispersive readout,” *Phys. Rev. Lett.*, vol. 95, p. 060501, 2005.
- [45] J. Majer *et al.*, “Coupling superconducting qubits via a cavity bus,” *Nature*, vol. 449, pp. 443–447, 2007.
- [46] L. Dicarlo *et al.*, “Demonstration of two-qubit algorithms with a superconducting quantum processor,” *Nature*, vol. 460, pp. 240–244, 2009.
- [47] M. D. Reed *et al.*, “Realization of three-qubit quantum error correction with superconducting circuits,” *Nature*, vol. 482, pp. 382–385, 2012.
- [48] D. Neamen, *Semiconductor Physics and Devices: Basic Principles*, 3rd ed. McGraw Hill, 2003.
- [49] E. H. Rhoderick, “Metal-semiconductor contacts,” *IEE Proc.*, vol. 129, no. 1, pp. 1–14, 1982.
- [50] D. K. Schroder, *Semiconductor Material and Device Characterization*, 3rd ed. John Wiley & Sons, 2006.
- [51] S. M. Sze and K. K. Ng, *Physics of semiconductor devices*, 3rd ed. Wiley, 2006.
- [52] V. L. Dalal, “Simple model for internal photoemission,” *J. Appl. Phys.*, vol. 42, pp. 2274–2279, 1971.

- [53] R. H. Fowler, “The Analysis of Photoelectric Sensitivity Curves for Clean Metals at Various Temperatures,” *Phys. Rev.*, vol. 38, pp. 45–56, 1931.
- [54] J. S. Helman and F. Sanchez-Sinencio, “Theory of Internal Photoemission,” *Phys. Rev. B*, vol. 7, no. 8, pp. 3702–3706, 1973.
- [55] C. R. Crowell, W. G. Spitzer, L. E. Howarth, and E. E. Labate, “Attenuation length measurements of hot electrons in metal films,” *Phys. Rev.*, vol. 127, no. 6, pp. 2006–2015, 1962.
- [56] A. Hiraki, *Metal-Semiconductor Interfaces*. IOS Press, 1995.
- [57] J. R. Weber *et al.*, “Defects in SiC for quantum computing,” *J. Appl. Phys.*, vol. 109, p. 102417, 2011.
- [58] A. Csóré, H. J. Von Bardeleben, J. L. Cantin, and A. Gali, “Characterization and formation of NV centers in 3C, 4H, and 6H SiC: An ab initio study CHARACTERIZATION and FORMATION of NV CENTERS ... CSÓRÉ, von BARDELEBEN, CANTIN, and GALI,” *Phys. Rev. B*, vol. 96, p. 085204, 2017.
- [59] H. J. von Bardeleben and J. L. Cantin, “NV centers in silicon carbide: from theoretical predictions to experimental observation,” *MRS Commun.*, vol. 7, pp. 591–594, 2017.
- [60] G. D. Cheng, Y. P. Wan, and S. Y. Yan, “Optical and spin coherence properties of NV center in diamond and 3C-SiC,” *Comput. Mater. Sci.*, vol. 154, pp. 60–64, 2018.
- [61] S. A. Zargaleh *et al.*, “Nitrogen vacancy center in cubic silicon carbide: A promising qubit in the 1.5 μ m spectral range for photonic quantum networks,” *Phys. Rev. B*, vol. 98, p. 165203, 2018.
- [62] A. R. Verma and P. Krishna, *Polymorphism and polytypism in Crystals*. Wiley, 1966.
- [63] N. W. Jepps and T. F. Page, “Polytypic transformations in silicon carbide,” *Prog. Cryst. Growth Charact.*, vol. 7, no. 1–4, pp. 259–307, 1983.
- [64] U. STARKE, J. BERNHARDT, J. SCHARDT, and K. HEINZ, “SiC SURFACE RECONSTRUCTION: RELEVANCY OF ATOMIC STRUCTURE FOR GROWTH TECHNOLOGY,” *Surf. Rev. Lett.*, vol. 06, no. 06, pp. 1129–1141, 1999.
- [65] L. S. Ramsdell, “Studies on Silicon Carbide,” *Am. Mineral.*, vol. 32, pp. 64–82, 1947.
- [66] G. Pensl and W. J. Choyke, “Electrical and optical characterization of Sb: SnO₂,” *Phys. B*, vol. 185, pp. 264–283, 1993.
- [67] J. B. Casady and R. W. Johnson, “Status of Silicon Carbide (SiC) as a Wide-Bandgap Semiconductor for High-Temperature Applications: A Review,” *Solid. State. Electron.*, vol. 39, no. 10, pp. 1409–1422, 1996.
- [68] R. C. Clarke *et al.*, “Recent advances in High Temperature, High Frequency SiC Devices,” in *1998 High-Temperature Electronic Materials, Devices and Sensors Conference*, 1998.
- [69] S. Y. Davydov and A. V. Troshin, “Estimates of the spontaneous polarization in silicon

- carbide,” *Phys. Solid State*, vol. 49, no. 4, pp. 759–761, 2007.
- [70] S. Y. Han *et al.*, “Ohmic contact formation mechanism of Ni on n-type 4H-SiC,” *Appl. Phys. Lett.*, vol. 79, pp. 1816–1818, 2001.
- [71] S. Jung *et al.*, “Reduction of water-molecule-induced current-voltage hysteresis in graphene field effect transistor with semi-dry transfer using flexible supporter,” *J. Appl. Phys.*, vol. 125, p. 184302, 2019.
- [72] D. M. Pozar, *Microwave Engineering*. Wiley, 2012.
- [73] Y. Kubo *et al.*, “Hybrid quantum circuit with a superconducting qubit coupled to a spin ensemble,” *Phys. Rev. Lett.*, vol. 107, p. 220501, 2011.
- [74] M. Hofheinz *et al.*, “Synthesizing arbitrary quantum states in a superconducting resonator,” *Nature*, vol. 459, pp. 546–549, 2009.
- [75] N. Zoric, A. Iavorschi, M. Sireteanu, G. Viziteu, and R. Ciobanu, “Design and Simulations of Idc Sensor Using Comsol Multiphysics and Dielectric Spectroscopy of LTCC Materials,” *Bul. Agir*, no. 3, pp. 63–69, 2013.
- [76] B. G. Sheeparamatti, P. D. Hanasi, V. Aibbigeri, and N. Meti, “Study of Capacitance in Electrostatic Comb-Drive Actuators,” in *Proceedings of the 2015 COMSOL Conference in Pune*, 2015, pp. 1–4.
- [77] G. González, E. S. Kolosovas-Machuca, E. López-Luna, H. Hernández-Arriaga, and F. J. González, “Design and fabrication of interdigital nanocapacitors coated with HfO₂,” *Sensors*, vol. 15, pp. 1998–2005, 2015.
- [78] I. Bahl, *Lumped Elements for RF and Microwave Circuits*. Artech House Publishers, 2003.
- [79] “COMSOL Multiphysics Reference Manual, version 5.3.” COMSOL, Inc.
- [80] V. E. Chelnokov, A. L. Syrkin, and V. A. Dmitriev, “Overview of SiC power electronics,” *Diam. Relat. Mater.*, vol. 6, pp. 1480–1484, 1997.
- [81] A. Qteish, V. Heine, and R. J. Needs, “Structural and electronic properties of SiC polytypes,” *Phys. B*, vol. 185, pp. 366–378, 1993.
- [82] C. H. Park, B.-H. Cheong, K.-H. Lee, and K. J. Chang, “Structural and electronic properties of cubic, 2H, 4H, and 6H SiC,” *Phys. Rev. B*, vol. 49, no. 7, pp. 4485–4493, 1994.
- [83] F. Bechstedt *et al.*, “Polytypism and Properties of Silicon Carbide,” *Phys. Stat. Sol.*, vol. 202, p. 35, 1997.
- [84] A. Qteish, V. Heine, and R. J. Needs, “Polarization, band lineups, and stability of SiC polytypes,” *Phys. Rev. B*, vol. 45, no. 12, pp. 6534–6542, 1992.
- [85] S. Y. Davydov, A. A. Lebedev, and O. V. Posrednik, “On the possibility of the experimental determination of spontaneous polarization for silicon carbide polytypes,” *Semiconductors*, vol. 46, no. 7, pp. 913–916, 2012.
- [86] G. Choi *et al.*, “Schottky barrier modulation of metal/4H-SiC junction with thin interface

- spacer driven by surface polarization charge on 4H-SiC substrate,” *Appl. Phys. Lett.*, vol. 107, p. 252101, 2015.
- [87] E. H. Nicollian, B. Schwartz, D. J. Coleman Jr., R. M. Ryder, and J. R. Brews, “Influence of a thin oxide layer between metal and semiconductor on Schottky diode behavior,” *J. Vac. Sci. Technol.*, vol. 13, p. 1047, 1976.
- [88] K. Park, H. Seok Go, Y. Jeon, J. P. Pelz, X. Zhang, and M. Skowronski, “Dependence of spontaneous polarization on stacking sequence in SiC revealed by local Schottky barrier height variations over a partially formed 8H-SiC layer on a 4H-SiC substrate,” *Appl. Phys. Lett.*, vol. 99, p. 252102, 2011.
- [89] Z. Zolnai, N. Q. Khanh, E. Szilágyi, Z. E. Horváth, and T. Lohner, “No Title,” in *XV International Conference for Physics Students ICPS 2000*, 2000, pp. 4–11.
- [90] R. T. Tung, “Electron transport of inhomogeneous Schottky barriers,” *Appl. Phys. Lett.*, vol. 58, pp. 2821–2823, 1991.
- [91] R. T. Tung, “Recent advances in Schottky barrier concepts,” *Mater. Sci. Eng. R*, vol. 35, pp. 1–138, 2001.
- [92] Q. W. Song, Y. M. Zhang, Y. M. Zhang, F. P. Chen, and X. Y. Tang, “Investigation of current transport parameters of Ti/4H-SiC MPS diode with inhomogeneous barrier,” *Chinese Phys. B*, vol. 20, p. 057301, 2011.
- [93] R. F. Schmitsdorf, T. U. Kampen, and W. Mönch, “Explanation of the linear correlation between barrier heights and ideality factors of real metal-semiconductor contacts by laterally nonuniform Schottky barriers,” *J. Vac. Sci. Technol. B Microelectron. Nanom. Struct. Process. Meas. Phenom.*, vol. 15, p. 1221, 1997.
- [94] T. N. Oder, T. L. Sung, M. Barlow, J. R. Williams, A. C. Ahyi, and T. Isaacs-Smith, “Improved ni schottky contacts on n-Type 4H-SiC using thermal processing,” *J. Electron. Mater.*, vol. 38, no. 6, pp. 772–777, 2009.
- [95] R. T. Tung, “Electron transport at metal-semiconductor interfaces: General theory,” *Phys. Rev. B*, vol. 45, no. 23, pp. 13509–13523, 1992.
- [96] “FLEXPDE.” PDE Solutions, Inc.
- [97] K. B. Park, Y. Ding, J. P. Pelz, M. K. Mikhov, Y. Wang, and B. J. Skromme, “Effect of inclined quantum wells on macroscopic capacitance-voltage response of Schottky contacts: Cubic inclusions in hexagonal SiC,” *Appl. Phys. Lett.*, vol. 86, p. 222109, 2005.
- [98] S. Bai, R. P. Devaty, W. J. Choyke, U. Kaiser, G. Wagner, and M. F. MacMillan, “Determination of the electric field in 4H/3C/4H-SiC quantum wells due to spontaneous polarization in the 4H SiC matrix,” *Appl. Phys. Lett.*, vol. 83, pp. 3171–3173, 2003.
- [99] A. Fissel, U. Kaiser, B. Schroter, W. Richter, and F. Bechstedt, “MBE growth and properties of SiC multi-quantum well structures,” *Appl. Surf. Sci.*, vol. 184, pp. 37–42, 2001.

- [100] Y. M. Blanter and I. Martin, “Transport through normal-metal-graphene contacts,” *Phys. Rev. B*, vol. 76, p. 155433, 2007.
- [101] V. M. Karpan *et al.*, “Graphite and graphene as perfect spin filters,” *Phys. Rev. Lett.*, vol. 99, p. 176602, 2007.
- [102] H. Schomerus, “Effective contact model for transport through weakly-doped graphene,” *Phys. Rev. B*, vol. 76, p. 045433, 2007.
- [103] G. Giovannetti, P. A. Khomyakov, G. Brocks, V. M. Karpan, J. Van Den Brink, and P. J. Kelly, “Doping graphene with metal contacts,” *Phys. Rev. Lett.*, vol. 101, p. 026803, 2008.
- [104] D. Defives, O. Durand, F. Wyczisk, O. Noblanc, C. Brylinski, and F. Meyer, “Electrical behaviour and microstructural analysis of metal Schottky contacts on 4H-SiC,” *Microelectron. Eng.*, vol. 55, pp. 369–374, 2001.
- [105] K. E. Byun *et al.*, “Graphene for true ohmic contact at metal-semiconductor junctions,” *Nano Lett.*, vol. 13, pp. 4001–4005, 2013.
- [106] M. H. Lee *et al.*, “Two-Dimensional Materials Inserted at the Metal/Semiconductor Interface: Attractive Candidates for Semiconductor Device Contacts,” *Nano Lett.*, vol. 18, pp. 4878–4884, 2018.
- [107] K. S. Novoselov *et al.*, “Electric Field Effect in Atomically Thin Carbon Films,” *Science* (80-.), vol. 306, pp. 666–669, 2004.
- [108] P. R. Wallace, “The band theory of graphite,” *Phys. Rev.*, vol. 71, no. 9, pp. 622–634, 1947.
- [109] A. Itoh, T. Kimoto, and H. Matsunami, “High Performance of High-Voltage 4H-SiC Schottky Barrier Diodes,” *IEEE Electron Device Lett.*, vol. 16, no. 6, pp. 280–282, 1995.
- [110] A. Itoh and H. Matsunami, “Analysis of Schottky barrier heights of metal/SiC contacts and its possible application to high-voltage rectifying devices,” *Phys. Status Solidi*, vol. 162, pp. 389–408, 1997.
- [111] D. Tomer, S. Rajput, L. J. Hudy, C. H. Li, and L. Li, “Intrinsic inhomogeneity in barrier height at monolayer graphene/SiC Schottky junction,” *Appl. Phys. Lett.*, vol. 105, p. 021607, 2014.
- [112] H. Zhong *et al.*, “Graphene in ohmic contact for both n -GaN and p -GaN,” *Appl. Phys. Lett.*, vol. 104, p. 212101, 2014.
- [113] V. V. Afanas’ev, *Internal Photoemission Spectroscopy: Fundamentals and Recent Advances*. Elsevier, 2014.
- [114] X. Aymerich-Humet, F. Serra-Mestres, and J. Millán, “An analytical approximation for the Fermi-Dirac integral $F_3(\eta)$,” *Solid State Electron.*, vol. 24, no. 10, pp. 981–982, 1981.
- [115] W. Kim *et al.*, “Tunable Graphene-GaSe Dual Heterojunction Device,” *Adv. Mater.*, vol. 28, pp. 1845–1852, 2015.
- [116] S. Y. Han and J.-L. Lee, “Interpretation of Fermi level pinning on 4H-SiC using synchrotron photoemission spectroscopy,” *Appl. Phys. Lett.*, vol. 84, pp. 538–540, 2004.

- [117] C. Mead, “Neuromorphic Electronic Systems,” in *Proceedings of the IEEE*, 1990, pp. 1629–1636.
- [118] B. Georgeot, “Quantum computing for physics research,” *Nucl. Instruments Methods Phys. Res. A*, vol. 559, pp. 6–12, 2006.
- [119] M. Nielsen and I. L. Chuang, *Quantum Computation and Quantum Information: 10th Anniversary Edition*. Cambridge University Press, 2010.
- [120] M. Di Ventra, Y. V Pershin, and L. O. Chua, “Circuit Elements With Memory: Memristors, Memcapacitors, and Meminductors,” in *Proceedings of the IEEE*, 2009, vol. 97, no. 10, pp. 1717–1724.
- [121] M. Di Ventra, F. L. Traversa, F. Bonani, and Y. V. Pershin, “Dynamic computing random access memory: A brain-inspired computing paradigm with memelements,” in *Proceedings - IEEE International Symposium on Circuits and Systems*, 2014, pp. 1070–1073.
- [122] Y. V. Pershin and M. Di Ventra, “Memcapacitive neural networks,” *Electron. Lett.*, vol. 50, no. 3, pp. 141–143, 2014.
- [123] Y. V. Pershin, F. L. Traversa, and M. Di Ventra, “Memcomputing with membrane memcapacitive systems,” *Nanotechnology*, vol. 26, p. 225201, 2015.
- [124] B. Y. V Pershin and M. Di Ventra, “Quantum Computation With Memory Circuit Elements,” in *Proceedings of the IEEE*, 2012, vol. 100, no. 6, pp. 2071–2080.
- [125] F. L. Traversa and M. Di Ventra, “Universal Memcomputing Machines,” *IEEE Trans. Neural Networks Learn. Syst.*, vol. 26, no. 11, pp. 2702–2715, 2015.
- [126] L. O. Chua, “Memristor-The Missing Circuit Element,” *IEEE Trans. Circuit Theory*, vol. CT-18, no. 5, pp. 507–519, 1971.
- [127] G. Choi *et al.*, “Multi-Level Capacitive Memory Effect in Metal / Oxide / Floating-Schottky Junction,” *J. Korean Phys. Soc.*, vol. 74, no. 10, pp. 979–983, 2019.
- [128] J. Martinez-Rincon, M. Di Ventra, and Y. V. Pershin, “Solid-state memcapacitive system with negative and diverging capacitance,” *Phys. Rev. B*, vol. 81, p. 195430, 2010.
- [129] M. Krems, Y. V. Pershin, and M. Di Ventra, “Ionic memcapacitive effects in nanopores,” *Nano Lett.*, vol. 10, pp. 2674–2678, 2010.
- [130] S. H. Jo, T. Chang, I. Ebong, B. B. Bhadviya, P. Mazumder, and W. Lu, “Nanoscale memristor device as synapse in neuromorphic systems,” *Nano Lett.*, vol. 10, pp. 1297–1301, 2010.
- [131] J. Borghetti, G. S. Snider, P. J. Kuekes, J. J. Yang, D. R. Stewart, and R. S. Williams, “‘Memristive’ switches enable ‘stateful’ logic operations via material implication,” *Nature*, vol. 464, pp. 873–876, 2010.
- [132] G. Indiveri, B. Linares-Barranco, R. Legenstein, G. Deligeorgis, and T. Prodromakis, “Integration of nanoscale memristor synapses in neuromorphic computing architectures,” *Nanotechnology*, vol. 24, p. 384010, 2013.

- [133] C. Eichler and A. Wallraff, “Controlling the dynamic range of a Josephson parametric amplifier,” *EPJ Quantum Technol.*, vol. 1, no. 2, pp. 1–19, 2014.
- [134] M. J. Feldman, P. T. Parrish, and R. Y. Chiao, “Parametric amplification by unbiased Josephson junctions,” *J. Appl. Phys.*, vol. 46, no. 9, pp. 4031–4042, 1975.
- [135] M. A. Castellanos-Beltran and K. W. Lehnert, “Widely tunable parametric amplifier based on a superconducting quantum interference device array resonator,” *Appl. Phys. Lett.*, vol. 91, p. 083509, 2007.
- [136] N. Bergeal *et al.*, “Phase-preserving amplification near the quantum limit with a Josephson ring modulator,” *Nature*, vol. 465, pp. 64–68, 2010.
- [137] T. C. White *et al.*, “Traveling wave parametric amplifier with Josephson junctions using minimal resonator phase matching,” 2015.
- [138] A. A. Clerk, M. H. Devoret, S. M. Girvin, F. Marquardt, and R. J. Schoelkopf, “Introduction to quantum noise , measurement , and amplification,” *Rev. Mod. Phys.*, vol. 82, pp. 1155–1208, 2010.
- [139] P. K. Tien, “Parametric Amplification and Frequency Mixing in Propagating Circuits,” *J. Appl. Phys.*, vol. 29, pp. 1347–1357, 2015.
- [140] W. H. Louisell, *Coupled mode and parametric electronics*. John Wiley & Sons, 1960.
- [141] N. Bergeal *et al.*, “Analog information processing at the quantum limit with a Josephson ring modulator,” *Nat. Phys.*, vol. 6, pp. 296–302, 2010.
- [142] B. Abdo, A. Kamal, and M. Devoret, “Nondegenerate three-wave mixing with the Josephson ring modulator,” *Phys. Rev. B*, vol. 87, p. 014508, 2013.
- [143] E. Flurin, N. Roch, F. Mallet, M. H. Devoret, and B. Huard, “Generating Entangled Microwave Radiation Over Two Transmission Lines,” *Phys. Rev. Lett.*, vol. 109, p. 183901, 2012.
- [144] N. Bergeal, F. Schackert, L. Frunzio, and M. H. Devoret, “Two-Mode Correlation of Microwave Quantum Noise Generated by Parametric Down-Conversion,” *Phys. Rev. Lett.*, vol. 108, p. 123902, 2012.
- [145] R. Movshovich *et al.*, “Observation of Zero-Point Noise Squeezing via a Josephson-Parametric Amplifier,” *Phys. Rev. Lett.*, vol. 65, no. 12, pp. 1419–1422, 1990.
- [146] E. P. Menzel *et al.*, “Path Entanglement of Continuous-Variable Quantum Microwaves,” *Phys. Rev. Lett.*, vol. 109, p. 250502, 2012.
- [147] K. G. Fedorov *et al.*, “Displacement of Propagating Squeezed Microwave States,” *Phys. Rev. Lett.*, vol. 117, p. 020502, 2016.
- [148] A. Bienfait *et al.*, “Magnetic Resonance with Squeezed Microwaves,” *Phys. Rev. X*, vol. 7, p. 041011, 2017.
- [149] S. J. Weber, A. Chantasri, J. Dressel, A. N. Jordan, K. W. Murch, and I. Siddiqi, “Mapping the

- optimal route between two quantum states,” *Nature*, vol. 511, pp. 570–573, 2014.
- [150] Q. Ficheux, S. Jezouin, Z. Leghtas, and B. Huard, “Dynamics of a qubit while simultaneously monitoring its relaxation and dephasing,” *Nat. Commun.*, vol. 9, pp. 1–6, 2018.
- [151] S. Kono *et al.*, “Nonclassical Photon Number Distribution in a Superconducting Cavity under a Squeezed Drive,” *Phys. Rev. Lett.*, vol. 119, p. 023602, 2017.
- [152] A. I. Lvovsky, “Iterative maximum-likelihood reconstruction in quantum homodyne tomography,” *J. Opt. B Quantum Semiclassical Opt.*, vol. 6, pp. S556–S559, 2004.
- [153] A. I. Lvovsky and M. G. Raymer, “Continuous-variable optical quantum-state tomography,” *Rev. Mod. Phys.*, vol. 81, pp. 299–332, 2009.
- [154] J. M. Chow, “Quantum Information Processing with Superconducting Qubits,” Yale University, 2010.
- [155] S. Filipp *et al.*, “Two-Qubit State Tomography Using a Joint Dispersive Readout,” *Phys. Rev. Lett.*, vol. 102, p. 200402, 2009.
- [156] J. M. Chow *et al.*, “Detecting highly entangled states with a joint qubit readout,” *Phys. Rev. A*, vol. 81, p. 062325, 2010.
- [157] S. Sheldon, L. S. Bishop, E. Magesan, S. Filipp, J. M. Chow, and J. M. Gambetta, “Characterizing errors on qubit operations via iterative randomized benchmarking,” *Phys. Rev. A*, vol. 93, p. 012301, 2016.
- [158] I. Wolfram Research, “Mathematica.” Wolfram Research, Inc., Champaign, Illinois, 2007.
- [159] T. Noh, G. Park, S. Lee, W. Song, and Y. Chong, “Construction of controlled-NOT gate based on microwave-activated phase (MAP) gate in two transmon system,” *Sci. Rep.*, vol. 8, no. 13598, pp. 1–9, 2018.
- [160] J. M. Chow, J. M. Gambetta, A. W. Cross, S. T. Merkel, C. Rigetti, and M. Steffen, “Microwave-activated conditional-phase gate for superconducting qubits,” *New J. Phys.*, vol. 15, p. 115012, 2013.
- [161] H. S. Ku *et al.*, “Single qubit operations using microwave hyperbolic secant pulses,” *Phys. Rev. A*, vol. 96, p. 042339, 2017.
- [162] H. H. Yoon *et al.*, “Strong Fermi-Level Pinning at Metal/n-Si(001) Interface Ensured by Forming an Intact Schottky Contact with a Graphene Insertion Layer,” *Nano Lett.*, vol. 17, pp. 14–19, 2017.
- [163] “Quantum Circuits, Inc.” [Online]. Available: <https://quantumcircuits.com>.
- [164] E. Knill *et al.*, “Randomized benchmarking of quantum gates,” *Phys. Rev. A*, vol. 77, p. 012307, 2008.
- [165] E. Magesan *et al.*, “Efficient measurement of quantum gate error by interleaved randomized benchmarking,” *Phys. Rev. Lett.*, vol. 109, p. 080505, 2012.

Curriculum Vitae

Personal Details

Name: Gahyun Choi

Address: Ulsan National Institute of Science and Technology (UNIST), 50 UNIST-gil, Eonyang-eup,
Ulju-gun, Ulsan 44919, South Korea

Phone: +82-10-2962-1028

E-mail: sloopy26@unist.ac.kr, ghchoi1126@gmail.com

Education

- Aug. 2013 – Aug. 2019 Ph.D. in Department of Physics, UNIST, Ulsan, South Korea
 Advisor: Prof. Kibog Park
 Focus: Memcapacitive device, charge transport across interface, quantum information devices
- Mar. 2010 – Aug. 2013 B.S. in Material Science Engineering and Device Physics, UNIST, Ulsan, South Korea

Research Experience

- Aug. 2015 – Aug. 2019 Research student, Quantum Information Team, KRISS, Daejeon
 Project 1: Squeezed State Generated by Josephson Parametric Amplifier
 Project 2: Three Qubit Entanglement in 3D Resonator
 Advisor: Dr. Yonuk Chong
- Jan. 2012 – Feb. 2012 Undergraduate Research Intern, Center for Mechanical Metrology
 Project 1: Dual-Fiber Optical Interferometer
 Advisor: Dr. Jae-Hyuk Choi

Awards

- May 2019 Excellence Prize for Oral Presentation, The Korean Physical Society
- Nov. 2018 Excellence Prize for Oral Presentation, The Korean Physical Society
- Jan. 2015 Excellence Prize for Poster Presentation, The Korean Physical Society
 Busan-Ulsan-Gyeongnam Branch
- Dec. 2012 Excellence Prize, Undergraduate Research Program (URP)

Scholarship

- Aug. 2013 – Aug. 2019 UNIST Scholarship
- Mar. 2010 – Aug. 2013 The National Scholarship for Science and Engineering

Teaching Experience

2016	Teaching Assistant: PHY505, Quantum Physics 1, UNIST
2015	Teaching Assistant: PHY301, Quantum Physics 1, UNIST
2014/2015	Teaching Assistant: PHY302, Quantum Physics 2, UNIST
2012/2013/2014	Teaching Assistant: PHY101, General Physics 1, UNIST
2012/2013	Teaching Assistant: PHY103, General Physics 2, UNIST
2011	Tutor: MTH111, Calculus 1, UNIST
2010	Tutor: MTH112, Calculus 2, UNIST

Technical Skills

Material Growth	Atomic Layer Deposition (ALD)
Fabrication	Photolithography, E-beam Lithography, Reactive Ion Etching (RIE), Deep RIE, Wet Etching, Rapid Thermal Annealing
Measurement	Current-voltage, Capacitance-voltage, Internal Photoemission, Network Analyzer, Spectrum Analyzer, Oscilloscope
Software	Labview, Mathematica, XIC, Inkscape, Adobe Illustrator, Origin Lab, COMSOL, FlexPDE

Publications

1. G. Choi, T. Noh, J. Choi, K. Park, W. Song, and Y. Chong, "Study on the Squeezed Microwave Photon Prepared by a Josephson Parametric Amplifier", *in preparation*.
2. G. Choi, W. Song, S. Jung, H. H. Yoon, K. Mo, J. Kim, W. Bahng, and K. Park, "Electric Dipole Formation at Au/Graphene Interface Investigated with Schottky Barrier Measurements on Au/Graphene/4H-SiC Junction", *in preparation*.
3. H. H. Yoon, W. Song, S. Jung, J. Kim, K. Mo, G. Choi, H. Y. Jeong, J. H. Lee, and K. Park, "Negative Fermi-Level Pinning Effect of Metal/n-GaAs(001) Junction with Graphene Insertion Layer", *in preparation*.
4. G. Choi, S. Jung, H. H. Yoon, J. Kim, Y. Chong, and K. Park, "Multi-Level Capacitive Memory Effect in Metal/Oxide/Floating-Schottky Junction", *J. Korean Phys. Soc.*, **74**, 979 (2019).
5. S. Jung, H. H. Yoon, H. Jin, K. Mo, G. Choi, J. Lee, H. Park, and K. Park, "Reduction of Water-Molecule-Induced Current-Voltage Hysteresis in Graphene Field Effect Transistor with Semi-Dry Transfer Using Flexible Supporter", *J. Appl. Phys.*, **125**, 184302 (2019).

6. H. H. Yoon, S. Jung, G. Choi, J. Kim, Y. Jeon, Y. S. Kim, H. Y. Jeong, K. Kim, S.-Y. Kwon, and K. Park, “Strong Fermi-Level Pinning at Metal/n-Si(001) Interface Ensured by Forming an Intact Schottky Contact with a Graphene Insertion Layer”, *Nano Lett.*, **17**, 44 (2017).
7. G. Choi, H. H. Yoon, S. Jung, Y. Jeon, J. Y. Lee, W. Bahng, and K. Park, “Schottky Barrier Modulation of Metal/4H-SiC Junction with Thin Interface Spacer Driven by Surface Polarization Charge on 4H-SiC Substrate”, *Appl. Phys. Lett.*, **107**, 252101 (2015).

International Conference Presentation

1. “Quantum state tomography in three-qubit superconducting system”, presented at 20th Anniversary of Superconducting Qubits (SQ20th), Tsukuba, Japan, May 2019. [Poster]
2. “Negative Fermi-Level Pinning in Metal/4H-SiC Junction Induced by Graphene Insertion Layer”, presented at the 34th International Conference on the Physics of Semiconductor (ICPS), Montpellier, France, Aug. 2018. [Poster]
3. “Study on the Squeezed Microwave Photon Prepared by a Josephson Parametric Amplifier”, presented at Dynamics in Artificial Quantum System (DAQS), Tokyo, Japan, Jan. 2018. [Poster]
4. “Study on the Squeezed Microwave Photon Prepared by a Josephson Parametric Amplifier”, presented at 15th International Conference on Squeezed States and Uncertainty Relations (ICSSUR), Jeju, Republic of Korea, Aug. 2017. [Poster]
5. “Multi-level Capacitive Memory Effect in Metal/Oxide/Floating-Schottky Junction”, presented at APS March Meeting, San Antonio, TX, USA, Mar. 2015. [Poster]

Domestic Conference Presentation

1. “State Tomography of Superconducting Multi-Qubits in Circuit QED”, presented at KPS Spring Meeting, Daejeon, Republic of Korea, Apr. 2019. [Oral]
2. “Efficient Readout Scheme of a Single Superconducting Transmon Qubit in Dispersive Regime Circuit QED”, presented at KPS Spring Meeting, Daejeon, Republic of Korea, Apr. 2019. [Poster]
3. “Error Analysis of the cNOT Gate Constructed by MAP+Z Gates in Two-Qubit Circuit QED System”, presented at KPS Fall Meeting, Changwon, Republic of Korea, Oct. 2018. [Oral]
4. “Electrical Properties of Metal/4H-SiC Junction Modulated by Graphene Insertion Layer”, presented at KPS Fall Meeting, Changwon, Republic of Korea, Oct. 2018. [Poster]
5. “Squeezing Microwave Photon Using a Josephson Parametric Amplifier”, presented at KPS Fall Meeting, Gyeongju, Republic of Korea, Oct. 2017. [Oral]
6. “Interface Energy Barrier Modulation of Schottky Junction Made on Polar 4H-SiC with Thin Interface Spacer Layer”, presented at KPS Busan-Ulsan-Gyeongnam Branch Meeting, Ulsan, Republic of Korea, Jan. 2015. [Poster]

7. “Schottky Barrier Modulation of Metal/4H-SiC Junction with Thin Interface Spacer Driven by Surface Polarization Charge on 4H-SiC Substrate”, presented at KPS Spring Meeting, Daejeon, Republic of Korea, Apr. 2014. [Poster]
8. “Effects of Spontaneous Polarization of 4H-SiC on Electrical Properties of Metal/4H-SiC Junction with Thin Interface Spacer Layer”, presented at KPS Fall Meeting, Changwon, Republic of Korea, Oct. 2013. [Poster]

Acknowledgement

I would like to express my special thanks to my advisor Prof. Kibog Park for giving great support and supervision during the whole PhD program. He has encouraged me with advice on research and even life whenever I feel discouraged. Also, he has been full of bright and critical ideas, always inspiring me. I am deeply grateful to Dr. Yonuk Chong who is another advisor at KRISS. Foremost, I appreciate to give the opportunity to do research at KRISS and introduce me to the world of superconducting quantum computing. I thank him for giving me opportunity still to explore more and providing full support. I would also like to thank my dissertation committee members, Prof. Jinguok Kim, Prof. Min-Suk Kwon, and Prof. Kunook Chung for providing thoughtful and valuable comments on my work.

Through my graduate career at UNIST and KRISS, I have been pleased with great group members. I want to thank them all for their encouragement and warm support. I thank the former UNIST lab members, Heungseok Go and Dr. Youngeun Jeon, Dr. Hanbyul Jin, and Dr. Sungchul Jung for teaching me everything I know about fabrication skills and research methods. They also encourage me to overcome my difficulties. I also appreciate Jung-Yong Lee and Hoon Hahn Yoon for valuable discussion and their support. I especially thank Junhyung Kim, Kyu Hyung Mo and Wonho Song for helping me with experiments and simulations of my researches while I was working in KRISS. I appreciate Jinyoung Park and Jaehyeong Jo who made me laugh and gave warm welcome. Every moment was enjoyable and memorable for me.

I would like to thank Dr. Junghwan Park for his enthusiastic assistance with everything about superconducting quantum systems. With his help, I could acclimatize to new environment. I especially thank Taewan Noh for teaching and helping me with everything that I could not complete by myself. I also want to thank Jiman Choi, Jinsu Son, Gwanyeol Park, Jisoo Choi, and Joonyoung Lee all provided insightful discussion and comments. I'm grateful to spend meaningful time together.

Finally, I would like to thank my parents and brother, who have provided me with deep understanding and endless support. Your unwavering love makes me to get great strength and confidence for my work. I dedicate my dissertation to all of you.

